

12-15-2018

Performance-Based Economical Seismic Design of Multistory Reinforced Concrete Frame Buildings and Reliability Assessment

Chunyu Zhang
cyz2019@gmail.com

Follow this and additional works at: <https://digitalscholarship.unlv.edu/thesesdissertations>

 Part of the [Civil Engineering Commons](#)

Repository Citation

Zhang, Chunyu, "Performance-Based Economical Seismic Design of Multistory Reinforced Concrete Frame Buildings and Reliability Assessment" (2018). *UNLV Theses, Dissertations, Professional Papers, and Capstones*. 3464.

<https://digitalscholarship.unlv.edu/thesesdissertations/3464>

This Dissertation is protected by copyright and/or related rights. It has been brought to you by Digital Scholarship@UNLV with permission from the rights-holder(s). You are free to use this Dissertation in any way that is permitted by the copyright and related rights legislation that applies to your use. For other uses you need to obtain permission from the rights-holder(s) directly, unless additional rights are indicated by a Creative Commons license in the record and/or on the work itself.

This Dissertation has been accepted for inclusion in UNLV Theses, Dissertations, Professional Papers, and Capstones by an authorized administrator of Digital Scholarship@UNLV. For more information, please contact digitalscholarship@unlv.edu.

PERFORMANCE-BASED ECONOMICAL SEISMIC DESIGN OF MULTISTORY
REINFORCED CONCRETE FRAME BUILDINGS
AND RELIABILITY ASSESSMENT

By

Chunyu Zhang

Bachelor of Science in Civil Engineering
Shenyang Jianzhu University
2009

Master of Science in Civil Engineering
Shenyang Jianzhu University
2012

A dissertation submitted in partial fulfillment
of the requirements for the

Doctor of Philosophy in Engineering – Civil and Environmental Engineering

Department of Civil and Environmental Engineering and Construction
Howard R. Hughes College of Engineering
The Graduate College

University of Nevada, Las Vegas
December 2018

Dissertation Approval

The Graduate College
The University of Nevada, Las Vegas

November 16, 2018

This dissertation prepared by

Chunyu Zhang

entitled

Performance-Based Economical Seismic Design of Multistory Reinforced Concrete
Frame Buildings and Reliability Assessment

is approved in partial fulfillment of the requirements for the degree of

Doctor of Philosophy in Engineering – Civil and Environmental Engineering
Department of Civil and Environmental Engineering and Construction

Ying Tian, Ph.D.
Examination Committee Chair

Kathryn Hausbeck Korgan, Ph.D.
Graduate College Interim Dean

Nader Ghafoori, Ph.D.
Examination Committee Member

Mohamed Kaseko, Ph.D.
Examination Committee Member

Samman Ladkany, Ph.D.
Examination Committee Member

Mohamed Trabia, Ph.D.
Graduate College Faculty Representative

ABSTRACT

Performance-based Economical Seismic Design of Multistory Reinforced Concrete Frame Buildings and Reliability Assessment

By

Chunyu Zhang

Dr. Ying Tian, Examination Committee Chair, Associate Professor

Department of Civil and Environmental Engineering and Construction

University of Nevada, Las Vegas

As the next generation of seismic design methodology, performance-based seismic design (PBSD) method requires a structure satisfy multiple preselected performance levels under different hazard levels. Optimal PBSD methods provide different strategies to design the numerous variables, including strength, stiffness and ductility of each structural component. The overall goal of this study is to develop a new optimal PBSD method for multi-story RC moment frames. This method is capable of overcoming the deficiencies of existing optimal PBSD methods and can be implemented by the U.S. design practice. The proposed method minimizes construction cost and takes the limit of member plastic rotation and optionally inter-story drift as

optimization constraints. Other seismic design requirements reflecting successful design practice are also incorporated. Simplification is made by reducing design variables into two, one for the overall system stiffness and the other for the overall system strength. The optimization contains two stages, the determination of feasible region boundary in normalized strength and stiffness domain and optimization in the material consumption domain. Capacity spectrum method, which jointly considers nonlinear static analysis and inelastic design spectrum, is used to estimate the global and local deformation demands at the peak dynamic response.

The proposed optimization approach is applied to the design of a six-story four-bay reinforced concrete frame. The optimal design results indicate that 30% of needed flexural strength and 26% of the cross-sectional area can be reduced from the initial strength-based design of this prototype structure. Nonlinear time-history analyses are conducted on the optimized structure using ten historical ground motions scaled to represent three levels of seismic hazard. In general, the average peak dynamic response meets the target performance requirements under the three levels of seismic hazard. Structural reliability analyses are applied on the optimal structure, the original structure and other 26 structures with different overall system stiffness and strength. The effects on nonperformance probability are determined based on the nonperformance contours, which is generated based on the reliability analyses results of all the 28 structures. To ensure the probabilities of nonperformance due to either plastic hinge or inter-story drift rotation is lower than the limits of all three preselected performance levels, the prototype structure should be design based on the relative overall system stiffness larger than

0.84 and the relative overall system strength larger than 0.4. To ensure that the probabilities of nonperformance only due to plastic hinge is lower than the limits of all three preselected performance levels, the prototype structure should be design based on two cases of relative strength and relative stiffness: (1) the relative overall system stiffness is larger than 0.75 and the relative overall system strength is larger than 0.4, and (2) the relative overall system stiffness is larger than 0.65 and the relative overall system strength is larger than 0.45. To ensure that the probabilities of nonperformance only due to inter-story drift rotation is lower than the limits of all three preselected performance levels, a structure should be design based on the relative overall system stiffness larger than 0.85 and the relative overall system strength larger than 0.6.

ACKNOWLEDGEMENTS

I would like to express my sincere gratitude to Dr. Ying Tian, my dissertation supervisor. His technical guidance was crucial for my Ph.D. research. Gratitude is extended to Dr. Nader Ghafoori, Dr. Mohamed Kaseko, Dr. Samman Ladkany, and Dr. Mohamed Trabia for their advice and serving on my dissertation committee. I would like to thank the support from the Department of Civil and Environmental Engineering and Construction. I would like to thank my mother, Li Yu, for her constant support and advice. I would like to offer special thanks to my late father, Zhongliang Zhang, for his selfless devotion to our family and my growth.

Chunyu Zhang

December 2018

TABLE OF CONTENTS

ABSTRACT.....	iii
ACKNOWLEDGEMENTS.....	vi
LIST OF TABLES.....	xi
LIST OF FIGURES.....	xii
CHAPTER 1. INTRODUCTION.....	1
1.1 Performance-based Seismic Design.....	1
1.1.1 Conventional strength-based seismic design.....	1
1.1.2 Concept of performance-based seismic design.....	4
1.2 Capacity Spectrum Method.....	12
1.2.1 Overview.....	12
1.2.2 Demand spectra.....	13
1.2.2.1 Elastic demand spectrum.....	14
1.2.2.2 Highly damped demand spectra.....	15
1.2.2.3 Inelastic demand spectra.....	16
1.2.3 Capacity spectrum.....	19
1.2.3.1 Pushover analysis.....	21
1.2.3.2 Transformation between MDOF and SDOF system.....	22
1.2.4 Estimation of nonlinear deformation demand.....	23
1.3 Displacement Coefficient Method.....	26
1.4 Direct Displacement-based Seismic Design Methods.....	28
1.4.1 Structural wall.....	29
1.4.2 SDOF systems.....	31
1.4.3 MDOF systems.....	32
1.4.4 Drawback of direct displacement-based seismic design method.....	35
1.5 Optimal Performance-based Seismic Design Methods.....	35
1.5.1 Optimal objectives.....	37
1.5.2 Optimization constraints.....	39

1.5.2.1 Deterministic constraints.....	40
1.5.2.2 Probabilistic constraints.....	41
1.5.3 Optimal algorithms.....	43
1.5.3.1 Metaheuristics methods.....	43
1.5.3.2 OC methods.....	48
1.6 Research Motivation.....	54
1.7 Research Objectives.....	56
1.8 Research Methodology and Tasks.....	57
CHAPTER 2 OPTIMAL PERFORMANCE-BASED SEISMIC DESIGN METHODOLOGY.....	59
2.1 Problem Statements.....	59
2.1.1 Objective function.....	60
2.1.2 Constraints.....	60
2.1.2.1 Performance constraints.....	61
2.1.2.2 Seismic design constraints.....	62
2.2 Optimal Methodology.....	65
2.2.1 Overview.....	65
2.2.2 Simplifications.....	68
2.2.3 Determination of feasible region boundary.....	71
2.2.3.1 Overview.....	71
2.2.3.2 Load-deformation response due to modified flexural stiffness.....	73
2.2.3.3 Determination of minimum stiffness at given flexural strength.....	76
2.3 Optimal Design Procedures.....	81
2.4 Extension of Proposed Optimal PBSD Method.....	84
2.5 Uniqueness of Proposed Optimal PBSD Method.....	85
CHAPTER 3 IMPLEMENTATION OF PROPOSED OPTIMAL PBSD METHOD AND EXAMINATION OF OPTIMAL DESIGN.....	88
3.1 Implementation of Proposed Optimal PBSD Method.....	88
3.1.1 Initial design of original RC frame structure.....	88

3.1.2 Finite element model.....	90
3.1.3 Optimization.....	94
3.1.3.1 Feasible region boundary in λ - α domain.....	94
3.1.3.2 Feasible region boundary in Ω_c - W_s domain and optimal design.....	97
3.1.3.3 Construction cost reduction due to optimal design.....	99
3.2 Examination of the Optimal Design.....	100
3.2.1 Hysteretic behavior model.....	101
3.2.2 Earthquake record selection and scaling.....	102
3.2.2.1 Earthquake record selection.....	102
3.2.2.2 Earthquake record scaling.....	104
3.2.3 Examination results and discussions.....	108
3.2.3.1 Results of optimal design.....	108
3.2.3.2 Result of original design.....	112
3.3 Validity Verification of the Optimal Design.....	115
 CHAPTER 4 RELIABILITY EVALUATION OF PROTOTYPE BUILDING.....	 121
4.1 Overview of Reliability Evaluation.....	121
4.2 Statistical Properties of Variables.....	122
4.2.1 Statistical properties of external loads.....	124
4.2.1.1 Dead load and live load.....	125
4.2.1.2 Seismic load.....	126
4.2.2 Statistical properties of member resistance.....	128
4.2.2.1 Elemental flexural strength.....	128
4.2.2.2 Elemental effective stiffness.....	129
4.2.3 Statistical properties of deformation limits.....	132
4.3 Sampling Methods.....	134
4.3.1 Monte Carlo sampling method.....	134
4.3.2 Latin Hypercube sampling method.....	135
4.3.2.1 Procedure of Latin Hypercube sampling method.....	135
4.3.2.2 Elimination of correlation between variables.....	138
4.4 Probability-based Nonperformance Probability.....	141

4.5 Fragility Curve Generation.....	143
4.6 Results and Discussion.....	144
4.6.1 Normalized deformation.....	144
4.6.2 Nonperformance probability.....	150
4.6.3 Fragility curve of nonperformance probability.....	151
4.6.4 Nonperformance probability contour.....	159
CHAPTER 5 SUMMARY AND CONCLUSIONS.....	172
5.1 Summary.....	172
5.2 Conclusions.....	175
5.3 Suggestions.....	177
REFERENCE.....	178
CURRICULUM VITAE.....	190

LIST OF TABLES

Table 1.1 Allowable inter-story drift ratio of RC frames in ATC-40 (1996), ASCE/SEI 41-06 (2007) and ASCE/SEI 41-13 (2014).....	9
Table 1.2 Allowable beam and column plastic hinge rotation capacity of RC moment frames in ASCE/SEI 41-13 (2014) [θ] (unit: rad.).....	10
Table 1.3 Target annual probabilities of nonperformance recommended by Paulay and Priestley (1992).....	43
Table 3.1 Flexural capacity of the elements in the original structure (unit: kip-in.).....	90
Table 3.2 Peak ground motion acceleration and velocity for three hazard levels.....	95
Table 3.3 Unit cost of material only and combined material and labor cost.....	98
Table 3.4 Comparison of cost for the initial and optimal designs.....	100
Table 3.5 Details of selected ground motions..	103
Table 3.6 Details of scaled ground motions..	105
Table 3.7 Maximum standard deviation of inter-story drift ratios of optimal structure.....	110
Table 3.8 Maximum standard deviation of inter-story drift ratio of original structure.....	114
Table 4.1 Summary of statistical properties of input variables.....	124
Table 4.2 Composition of different types of nonperformance (unit: %)......	145
Table 4.3 Normalized width of the 95% confidence band (w/a).....	146
Table 4.4 Probabilities of nonperformance due to different types deformation of the optimal and original structures.....	150
Table 4.5 Probability of occurrence of the optimal and original structures under three hazard levels (unit: %)......	155

LIST OF FIGURES

Figure 1.1 Performance objectives determined by different target performance levels and different hazard levels in ASCE/SEI 41-06 (2007).....	6
Figure 1.2 Capacity spectrum method to predict structural non-linear deformation demand.....	13
Figure 1.3 Elastic demand spectrum based on ASCE 7-10 (2010).....	14
Figure 1.4 Highly damped demand spectra (Anil K. Chopra 2017).....	16
Figure 1.5 Elastic demand spectrum in different formats: (a) period vs. pseudo acceleration; (b) spectral displacement vs. spectral acceleration.....	17
Figure 1.6 Elastic and inelastic demand spectra based on Vidic (1994).....	19
Figure 1.7 Pushover analysis and capacity spectrum establishment: (a) the first mode shape and the corresponding load pattern; (b) gravity and lateral loads; (c) top displacement vs. base shear curve of MDOF system; and (d) capacity spectrum curve of SDOF system, and demand spectra.....	20
Figure 1.8 Different equivalent methods to transform non-linear capacity spectrum curve to equivalent bilinear capacity spectrum: (a) identical intersection and no post-yielding stiffness; (b) different intersections and no post yield stiffness; and (c) identical intersection and positive post-yielding stiffness.....	25
Figure 1.9 Fanned radially-cracked region at the bottom of a structural wall and schematic strain distribution at the base (Sasani 1998).....	29
Figure 1.10 Schematic diagram in Moehle (1992): (a) SDOF RC bridge pier; (b) idealized flexural curvature; (c) elastic response spectrum.....	31
Figure 1.11 Target yield mechanism for moment frame (Goel et al. 2010).....	33
Figure 1.12 The combined universal gravitation force and the universal gravitations caused by the other masses (Rashedi 2009).....	45
Figure 1.13 Two steel frame examples in the study of Kaveh et al. (2010): (a) three-story four-bay planar steel moment frame; (b) nine-story five-bay planar steel moment frame....	47
Figure 1.14 Research methodology and procedure.....	58
Figure 2.1 Structural failure types: (a) beam-sway mechanism; and (b) soft story mechanism....	62
Figure 2.2 Beam-sway mechanism and column flexural strength in the first floor.....	64

Figure 2.3 Framework of optimization: (a) optimization in material consumption domain; (b) stiffness optimization for system with different strengths; (c) MDOF-SDOF transformation; (d) nonlinear static analysis and determination of roof displacement demands; and (e) N2 method using inelastic spectra.....	66
Figure 2.4 Constructing based shear vs. roof displacement response based on nonlinear static analysis result of the structure without stiffness modification ($\lambda = 1$).....	76
Figure 2.5 Effects of modifying relative stiffness factor λ on capacity and demand curves.....	78
Figure 2.6 Flow of the optimal PBSO method proposed in this study.....	83
Figure 2.7 Illustration of the two times of optimal PBSO methods with (a) large interval; and (b) small interval.....	84
Figure 2.8 Comparison of the searching method of different optimal algorithms: (a) OC method proposed by Zou and Chan (2005); (b) and (c) optimal algorithm proposed in this study....	86
Figure 3.1 Prototype RC frame building: (a) floor plan; and (b) elevation plan.....	89
Figure 3.2 Illustration of (a) location of the zero-length plastic hinge elements; (b) concentrated plasticity model of one column; and (c) moment-rotation backbone curve of the plastic hinge suggested by Lignos and Krawinkler (2012).....	91
Figure 3.3 Transformation of loads: (a) two-way slab load distribution; (b) load combination; and (c) equivalent concentrated loads.....	93
Figure 3.4 Feasible region of the six-story four-span RC moment frame in λ - α domain.....	95
Figure 3.5 Feasible region boundary and optimal solutions in Ω_c - W_s domain.....	97
Figure 3.6 Application of the capacity spectrum method to determine the seismic deformation demands of occasional, rare, and very rare earthquakes.....	99
Figure 3.7 Hysteretic behavior of modified Ibarra-Medina-Krawinkler model (Lignos and Krawinkler 2012).....	101
Figure 3.8 Time-history of unscaled horizontal ground acceleration for ten earthquakes.....	104
Figure 3.9 Time-history of ten horizontal ground acceleration scaled according to very rare earthquake level.....	105
Figure 3.10 Time-history of ten horizontal ground acceleration scaled according to rare earthquake level.....	106
Figure 3.11 Time-history of ten horizontal ground acceleration scaled according to occasional earthquake level.....	106

Figure 3.12 Acceleration response spectra and scaled ground motions for different hazard levels: (a) very rare earthquake; (b) rare earthquake; and (c) occasional earthquake.....	107
Figure 3.13 Peak inter-story drift ratio for optimal design subjected to ground motions scaled for (a) occasional earthquakes; (b) rare earthquakes; and (c) very rare earthquakes.....	109
Figure 3.14 Ratio of average peak plastic hinge rotation demand to capacity ($\theta_{max}/[\theta]$) for optimal design subjected to ground motions scaled for (a) occasional earthquakes; (b) rare earthquakes; and (c) very rare earthquakes.....	111
Figure 3.15 Inter-story drift ratio for original design subjected to ground motions scaled for (a) occasional earthquakes; (b) rare earthquakes; and (c) very rare earthquakes.....	113
Figure 3.16 Ratio of average peak plastic hinge rotation demand to capacity ($\theta_{max}/[\theta]$) for original structure subjected to ground motions scaled for (a) rare earthquakes and (b) very rare earthquakes.....	115
Figure 3.17 Feasible region and the design variables of nine structures in (a) λ - α domain and (b) Ω_c - W_s domain.....	116
Figure 3.18 Peak inter-story drift ratio of the nine structures under rare earthquake derived from dynamic analyses and the feasible region boundary determined from static analyses.....	118
Figure 3.19 Contours of the peak normalized inter-story drift ratio and the design variables of the nine structures.....	119
Figure 3.20 Construction cost of the nine structures for verifying the validity of the proposed optimal PBSM method.....	120
Figure 4.1 Probability density function (PDF) curve of: (a) normal distribution; and (b) Type I distribution.....	126
Figure 4.2 Probability density function curve of lognormal distribution.....	127
Figure 4.3 Measured ratio between effective stiffness and gross bending stiffness (Elwood 2007).....	130
Figure 4.4 Distribution fitting of discrete stiffness ratio (a) frequency histogram of discrete stiffness ratio and PDF of fitting lognormal distribution; (b) cumulate frequency histogram of stiffness ratio and CDF of fitting lognormal distribution.....	131
Figure 4.5 Probability density function curve of Beta distribution.....	133
Figure 4.6 Procedure of Latin Hypercube sampling method: (a) representative values selection from CDF of one variable; (b) frequency histogram and PDF of selected representative	

values; (c) order rearranging of representative values of one variable; and (d) input data matrix of all variables and samples.....	136
Figure 4.7 Relationship between two variables: (a) correlation and (b) independent.....	138
Figure 4.8 Illustration of the relationship between two input variables: (a) correlated relationship (b) independent relationship.....	141
Figure 4.9 Statistical result of the peak normalized plastic deformations (maximum value of $\gamma/[\gamma]$ and $\theta/[\theta]$) of the optimal and original design in various performance levels: (a) collapse prevention; (b) life safety; and (c) immediate occupancy.....	147
Figure 4.10 Statistical result of the peak normalized plastic deformations (peak $\theta/[\theta]$) of the optimal and original design in various performance levels: (a) collapse prevention; (b) life safety; and (c) immediate occupancy.....	148
Figure 4.11 Statistical result of the peak normalized plastic deformations (peak $\gamma/[\gamma]$) of the optimal and original design in various performance levels: (a) collapse prevention; (b) life safety; and (c) immediate occupancy.....	149
Figure 4.12 Fragility curves for the optimal design in different nonperformance types: (a) either $\theta/[\theta] > 1$ or $\gamma/[\gamma] > 1$; (b) $\theta/[\theta] > 1$; and (c) $\gamma/[\gamma] > 1$	152
Figure 4.13 Fragility curves for the original design in different nonperformance types: (a) either $\theta/[\theta] > 1$ or $\gamma/[\gamma] > 1$; (b) $\theta/[\theta] > 1$; and (c) $\gamma/[\gamma] > 1$	153
Figure 4.14 Definition of the four types of damage states.....	154
Figure 4.15 Probability histogram of four damage states of the (a) optimal and (b) original structures.....	156
Figure 4.16 Fragility curves for both the optimal and original designs in different performance levels: (a) collapse prevention; (b) life safety; and (c) immediate occupancy.....	158
Figure 4.17 Probability contours of nonperformance due to inter-story drift for different performance levels (a) collapse prevention' (b) life safety and (c) immediate occupancy (unit: %)......	161
Figure 4.18 Deformation demand of inelastic SDOF systems with identical stiffness but different yield strength.....	162
Figure 4.19 Probability contours of nonperformance due to plastic hinge rotation for different performance levels (a) collapse prevention; (b) life safety and (c) immediate occupancy (unit: %)......	163

Figure 4.20 Probability contours of nonperformance due to either inter-story drift or plastic hinge rotation for different performance levels (a) collapse prevention; (b) life safety; and (c) immediate occupancy (unit: %)......166

Figure 4.21 Nonperformance contours due to (a) inter-story drift; (b) plastic hinge rotation; and (c) either plastic hinge rotation or inter-story drift (unit: %)......169

CHAPTER 1

INTRODUCTION

1.1 Performance-based Seismic Design

1.1.1 Conventional strength-based seismic design

Seismic design attempts to design a structure capable of resisting both gravity and seismic loads. Strength, stiffness and inelastic deformation capacity influence the seismic performance of a structure. The conventional strength-based seismic design method in the U.S. embodied in ASCE 7-10 (2010) designs strength and stiffness based on elastic seismic analysis results. According to this standard, seismic design can be performed based on results of static analyses, such as equivalent lateral force method and modal response spectrum method, or dynamic (time-history) analyses.

In ASCE 7-10 (2010), the widely used static methods start from externally applying lateral seismic forces on a building, then design element stiffness, and finally design element strength. The design seismic force for the structure, the total design base shear, is derived by dividing the seismic force of an elastic single degree of freedom (SDOF) structure with identical natural period by a strength reduction factor, R . The seismic force of the elastic SDOF structure is determined by structural seismic weight and design spectra response acceleration and the estimated structural vibration period, T . Design earthquake for design earthquake level shall be modified based on given site type. T can be estimated by empirical equations or eigen-value

analyses. Normally, the lateral strength of a structure to resist seismic loads is designed to be lower than that needed to maintain elastic response in severe earthquakes. Then the structure would behave inelastically under moderate or severe earthquake to dissipate more earthquake induced energy than an elastic structure. Therefore, the design seismic force is derived by dividing design earthquake of the elastic structure by R . The value of R is determined based on the observations of performance of certain structural type under severe earthquakes (Miranda and Bertero, 1994).

The stiffness design, in ASCE 7-10 (2010), is performed by selecting section sizes of structural elements based on structural design experience and architectural requirements. Then the inelastic deformation of the structure is checked by comparing the estimated inter-story drift ratio under design-level earthquake and the inter-story drift ratio limit given in ASCE 7-10 (2010). Because the structure performs nonlinearly under a design-level earthquake, the total deformation demand, accounting for both elastic and inelastic deformations, can be estimated by multiplying a deflection amplification factor, C_d , to the elastic inter-story drift. Element stiffness shall be modified based on the checking result to make sure that the structure inter-story drift ratio does not exceed the specified drift limit.

After section sizes are determined, the needed flexural strength of element can be obtained based on the elastic analysis results of the structure under combined gravity and design seismic force in multiple combinations. The controlling strength demand of each element under multiple load combinations is selected to be the needed flexural strength.

Some inaccurate estimations about structural deformation demand and capacity exist in the above procedure of the force-based seismic design method. First, T used to obtain the design seismic force is derived from empirical equations or elastic analysis. However, the actual vibration period keeps decreasing during seismic excitations causing nonlinear structural performance, and may be far different from T . Second, R and C_d are identical for a specific type of structure without considering its uniqueness. For example, in ASCE 7-10 (2010), R is recommended as 8, and C_d as 5.5 for RC special moment-resisting frames regardless their floor levels, spans and irregularity. This roughly determined value may lead inaccurate estimation of structural ductility demand (Zameeruddin and Sangle, 2016).

Some observations of the structural damage made after the relatively recent earthquakes in the U.S. and Japan, such as the Northridge earthquake (1994 M6.7) and the Kobe earthquake (1995 M7.2), revealed the drawbacks of the conventional strength-based seismic design method. In these earthquakes, although the structures generally performed well, they suffered unexpected severe structural damage, and high economic loss due to dysfunction and prohibiting repair cost. (Rainer and Karacabeyli, 2000; Ghobarah, 2001). The total financial loss of the Northridge and Kobe earthquakes reached about \$20 billion (Kircher et al., 1997) and \$200 billion, respectively (Bertero and Bertero, 2002).

The disadvantages of strength-based seismic design are (1) only life safety performance level (i.e. life safety) is considered (Krawinkler, 1999; Ghobarah, 2001; Sung et al., 2009); (2) non-linear behavior causing the damage of structure in different hazard levels cannot be

predicted directly; instead it is derived based on some inaccurate assumptions (Ghobarah, 2001; Priestley et al., 2007; Sung et al., 2009); and (3) this method is lack of socio-economic description or information, such as cost of repair, for decision making (Krawinkler, 1999).

1.1.2 Concept of performance-based seismic design

To avoid the deficiency in the conventional force-based method of seismic design, performance-based seismic design (PBSD) method was proposed by the American scientists and engineers in the early 1990s (Liu et al., 2004). PBSD is a progressive method, by which a structure is designed to achieve a target performance objective under each specified hazard level (Ghobarah, 2001). The performance objective is used to distinguish the acceptable or unacceptable structures, and shall be different for diverse hazard levels, such as mediate and severe earthquakes. Different from the conventional force-based method, which obtains structural safety or serviceability with uncertain reliability, PBSD provides designers with a method to select a performance objective for diverse hazard levels (Krawinkler, 1999).

As the next generation of seismic design methodology, PBSD has been a major focus of earthquake engineering community. This method was included in: SEAOC Vision 2000 (1995), ATC-40 (1996), FEMA 273 and 274 (1996), FEMA 356 (2000), ASCE/SEI 41-06 (2007) and ASCE/SEI 41-13 (2014). These documents are evolutionary in the definition of performance objectives, seismic evaluation and design methodologies; nevertheless, the basic concepts of PBSD are identical (Ghobarah, 2001). In SEAOC Vision 2000 (1995), the framework of PBSD was established to accommodate various performance objectives. Structural performance was

classified into five levels. Four different seismic design methods were included in this standard: conventional force-based method, displacement-based method, energy-based method, and prescriptive design method. In ATC-40 (1996), the performance levels of the structural and non-structural elements were defined separately. In addition, capacity spectrum method, an inelastic static method, was suggested to be incorporated in PBS. Even though some flaws existed within this method, it gave a good estimation of seismic deformation capacity and demand (Priestley, 2000). In FEMA 273 and 274 (1996), PBS related performance levels with hazard levels to define performance objective. Structural performance was classified into four performance levels: collapse prevention (CP), life safety (LS), immediate occupancy (IO), and operational performance levels. Different seismic evaluation and design methods, from linear static to nonlinear dynamic methods, were adopted for PBS in FEMA 273 and 274 (1996). Based on engineering practice and observations, the values of deformation limits, such as allowable plastic hinge rotation, used to identify whether a structure meets a certain performance level, were adjusted in FEMA 356 (2000), and followed by ASCE/SEI 41-06 (2007). Seismic evaluation methods, such as the simplification of the factors used in displacement coefficient method to predict the peak structure displacement demand, were updated in ASCE/SEI 41-06 (2007). The allowable plastic hinge rotations were slightly adjusted in ASCE/SEI 41-13 (2014). Moreover, specific limit of inter-story drift deformation was eliminated from this standard.

Based on the standards mentioned above, it can be summarized that PBS method includes four important aspects: multiple performance objectives, criteria used to define the limit

states of damage, structural seismic analysis method, and design methodology. First, the purpose of PBSO is to reduce the unexpectedly high cost due to the loss of use and repair (Ghobarah, 2001); thus multiple performance levels, related to different types of cost, shall be satisfied under different hazard levels. Figure 1.1 is one example of the definition of performance objectives. The chessboard table is composed by different performance levels indicated by the horizontal axis, and different earthquake hazard levels indicated by the vertical axis. The performance levels are defined as the limit states of damage for both structural and nonstructural components of a building (ASCE/SEI 41-13, 2014). Hazard levels can be defined by ground acceleration in either a return period format, such as 2475 years for a very rare earthquake, or a probability of exceedance in a specified time period format, such as 2% probability of exceedance in 50 years (2%/50 year) for a very rare earthquake. Each letter in this chessboard table is defined as one

		Target Performance Levels			
		Operational Performance (OP)	Immediate Occupancy (IO)	Life Safety (LS)	Collapse Prevention (CP)
Earthquake Hazard levels	frequent 75%/50 year	<i>a</i>	<i>b</i>	<i>c</i>	<i>d</i>
	occasional 50%/50 year	<i>e</i>	<i>f</i>	<i>g</i>	<i>h</i>
	rare 10%/50 year	<i>i</i>	<i>j</i>	<i>k</i>	<i>l</i>
	very rare 2%/50 year	<i>m</i>	<i>n</i>	<i>o</i>	<i>p</i>

Figure 1.1 Performance objectives determined by different target performance levels and different hazard levels in ASCE/SEI 41-06 (2007)

performance objective, reflecting the target performance level under a certain hazard level. A structure needs to satisfy all the selected performance objectives.

Based on ASCE/SEI 41-06 (2007), the performance objectives k and p in Figure 1.1, are defined as the basic safety performance objectives, which are suitable for office, residential and other general constructions. Nevertheless, some categories of buildings, such as schools, hospitals and some government or communication buildings, are more important due to either the unique social function or the needed ability to avoid large casualties. Thus, enhanced performance objectives are applied on such buildings. The enhanced performance objective can be a combination of a single basic safety performance objective and a lower performance objective, such as the combination of k and o ; alternatively, the enhanced performance objective can be a combination of two lower performance objectives, such as j and o . If a building, such as warehouse, is less important, the limiting performance objectives applied on its seismic designs can be either a single basic safety performance objective, such as k or p alone, or any other single higher performance, such as g .

The second aspect of PBSO is the acceptance criteria. To determine whether a structure can satisfy a certain performance level, criteria used to define the limited damage states shall be explicitly quantified. The criteria can be a single criterion or a combination of allowable stress, load, strain, displacement, acceleration and energy dissipation. Based on the study by Moehle (1992), strain and deformation are more suitable for measuring damage than stress. Therefore, PBSO can be deformation-based. However, in addition to deformation, structural damage is

affected by other parameters, such as the accumulation and distribution of structural damage, and the failure mode of element and overall structure (Ghobarah, 2001). Thus comprehensive criteria, considering both deformation and other influence factors, are used to describe the structural damage states in some studies. For instance the Park and Ang damage index (Park and Ang, 1985) considers both plastic deformation and dissipated energy under cyclic loading (Mechakhchekh and Ghosn, 2007). Further studies are still likely needed for a more widely accepted criterion to quantify structural damage states.

RC special moment-resisting frame is a conventional structural type. In the current seismic evaluation standards in the U.S., the only explicit damage criteria of this structural type are the deformation-based criteria, including allowable inter-story drift ratio and plastic hinge rotation. The standards that include these two deformation indexes, are: ATC-40 (1996), FEMA-273 (1996), FEMA-356 (2000), ASCE/SEI 41-06 (2007), and ASCE/SEI 41-13 (2014).

In these standards, the allowable interstory drift is given for three performance levels: Immediate Occupancy (IO), Life Safety (LS), and Structure Stability (SS) in ATC-40 (1996) or Collapse Prevention (CP) in all the other standards. Along the timeline of these standards, there are two major advancements regarding the allowable values, as shown in Table 1.1. In ATC-40 (1996), the allowable inter-story drift ratio was given for only two performance levels as 2% for LS performance level and 3.5% for SS performance level. Since FEMA-273 (1996), the allowable interstory drift ratio was given for three performance levels. Note, in ASCE/SEI 41-13 (2014), there is no specific value for the allowable inter-story drift ratio, excepted for some

general descriptions of damage status

Table 1.1 Allowable inter-story drift ratio of RC frames in ATC-40 (1996), ASCE/SEI 41-06 (2007) and ASCE/SEI 41-13 (2014)

Performance levels	Collapse Prevention (CP) or Structural stability (SS)	Life Safety (LS)	Immediate Occupancy (IO)
ATC-40	3.5%	2%	–
FEMA-273 to ASCE/SEI 41-06	4% transient or permanent	2% transient; 1% permanent	1% transient; negligible permanent
ASCE/SEI 41-13	Transient drift sufficient to cause extensive nonstructural damage. Extensive permanent drift.	Transient drift sufficient to cause nonstructural damage. Noticeable permanent drift.	Transient drift that causes minor or no nonstructural damage. Negligible permanent drift.

The values of the allowable plastic hinge rotation of the RC beams and columns were also subjected to modifications and increased gradually. Compared with ASCE/SEI 41-06 (2007), ASCE/SEI 41-13 (2014) doubled the allowable the values of plastic hinge rotations for the LS and CP performance levels. In both documents, the allowable plastic rotation was defined as a function of internal force and section detailing, as shown in Table 1.2. In this table, V = shear force; P = axial force; ρ and ρ' = tension and compression reinforcement ratios; ρ_{bal} = reinforcement ratio producing balanced strain conditions; b , d and A_g = width, depth and gross area of beam or column section; and f'_c = concrete cylinder compressive strength.

Table 1.2 Allowable beam and column plastic hinge rotation capacity of RC moment frames in ASCE/SEI 41-13 (2014) [θ] (unit: rad.)

Beam plastic hinge rotation capacity					Column plastic hinge rotation capacity				
$\frac{\rho - \rho'}{\rho_{bal}}$	$\frac{V}{bd\sqrt{f'_c}}$	Performance level			$\frac{P}{A_g f'_c}$	$\frac{V}{bd\sqrt{f'_c}}$	Performance level		
		IO	LS	CP			IO	LS	CP
≤ 0.0	≤ 3	0.010	0.025	0.05	≤ 0.1	≤ 3	0.005	0.045	0.060
	≥ 6	0.005	0.020	0.04		≥ 6	0.005	0.045	0.060
≥ 0.5	≤ 3	0.005	0.020	0.03	≥ 0.6	≤ 3	0.003	0.009	0.010
	≥ 6	0.005	0.015	0.02		≥ 6	0.003	0.007	0.008

The third aspect of PBSM method is structural analysis method. Diverse methods of structural seismic analysis are available to estimate the nonlinear deformation demand on a structure under a certain seismic hazard level. In PBSM, whether the structure satisfies the selected performance level can be determined by comparing the estimated deformation demand, in terms of plastic hinge rotation and inter-story drift ratio, with the corresponding deformation criteria mentioned previously.

The structural analysis methods include dynamic time-history and static analyses. The structural model used for these analyses can be either elastic or inelastic (nonlinear). To estimate the structural nonlinear behavior under moderate or severe earthquakes, both nonlinear dynamic and static analysis can be used. Normally, the dynamic time-history analysis provides a more realistic structural response than the static methods, especially for moderate and severe earthquakes and for tall buildings (Deierlein et al., 2010). However, this method is limited by the high computational cost due to the need of using multiple earthquake records, and the sensitivity to hysteretic model and ground motion selection (Elwood et al., 2007). The nonlinear static

method (pushover analysis) cannot effectively capture energy dissipation and lacks accuracy in defining the strength and stiffness degradation of elements under cycle loading; however, nonlinear static analysis is still widely adopted in practice due to its strong theoretical basis and convenience. Both capacity spectrum method proposed by Fajfar (1999) and the displacement coefficient method recommended in FEMA-273 (1996) to ASCE/SEI 41-13 (2014) can be used to estimate the target displacement of the structure. These two methods are described with details in Sections 1.2 and 1.3 respectively.

The fourth aspect of PBSB method is design methodology. Two types of PBSB methodology exist: the iteration method by evaluating and modifying the force-based design result, and the direct deformation-based method (Priestley, 2000; Zameeruddin and Sangle, 2016). The former method alternately applies performance-based structural analysis and force-based seismic design. The structural analysis is used to check whether a structure meets the selected performance objectives. If not, the force-based seismic design is applied to redesign the structure. This process is repeated until all performance objectives are satisfied. This iteration process significantly increases the computational cost of PBSB if multiple performance objectives are to be satisfied (Priestley, 2000). Direct deformation-based method attempted to incorporate deformation criteria in the preliminary design stage without an iteration process (Priestley, 2000; Bertero and Bertero, 2002). This method is introduced in Section 1.4.

1.2 Capacity Spectrum Method

1.2.1 Overview

To estimate the nonlinear response of a structure under moderate and severe earthquakes, several methods based on pushover analysis and demand spectra were proposed. In the pushover analysis (Section 1.2.3.1), increasing lateral loads are monotonically applied along the height of a multi-degree-of-freedom (MDOF) structure defined with inelastic properties. The MDOF system is converted into an equivalent SDOF system (Section 1.2.3.2). In the equivalent SDOF system, demand spectrum is used to estimate the deformation demand of a bilinear equivalent single-degree-of-freedom (SDOF) system (Priestley 2000).

One of the nonlinear static methods was the N2 method proposed by Fajfar (1988 and 1996) using inelastic demand spectrum and pushover analysis results. A similar method called capacity spectrum method was proposed by Freeman (1988) using highly damped demand spectra and pushover analysis results. In this method, both capacity and demand spectrum was expressed in spectral acceleration vs. spectra displacement format (Priestley, 2000). These two methods were combined as a new version of capacity spectrum method based on the work of Fajfar (1999). This method included both physical basis of inelastic demand spectra in the N2 method, and the convenient graphical procedure in the capacity spectrum method proposed by Fajfar (2000).

Figure 1.2 shows the capacity spectrum method proposed by Fajfar (1999). The capacity spectrum is obtained from pushover analysis results, and the demand spectrum is derived from

the elastic demand spectrum. Both of these spectra are expressed in spectral displacement (S_d) vs. spectral acceleration (S_a) format. The demand spectrum intersects with the capacity spectrum. The intersection between the capacity spectrum curve and the demand spectrum curve is used to predict the seismic response of a structure under a single hazard level. An idealized bilinear response is derived based on equivalent energy theory. Three aspects are included in the capacity spectrum method: the demand spectrum establishment, the capacity spectrum establishment, and the nonlinear deformation estimation based on the capacity spectrum and the demand spectrum. These aspects are described in the following sections.

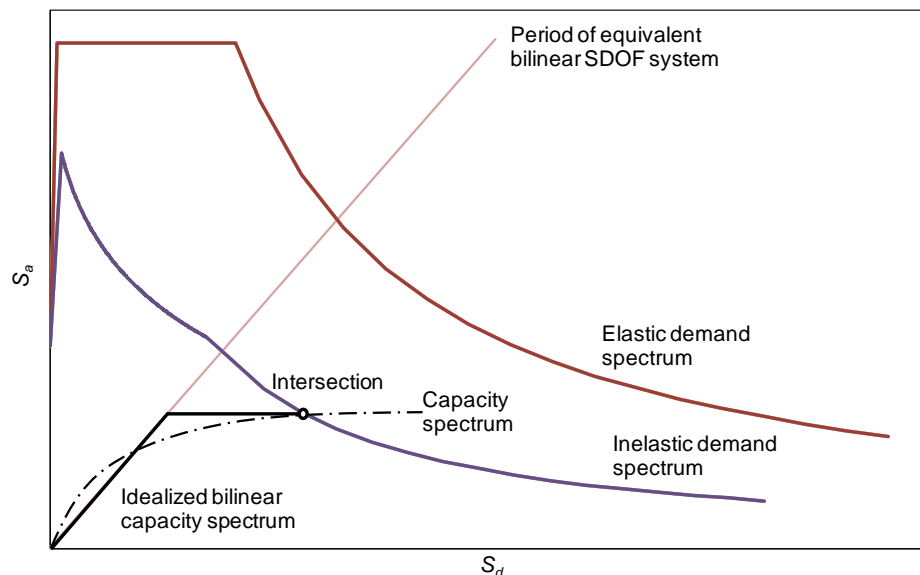


Figure 1.2 Capacity spectrum method to predict structural non-linear deformation demand

1.2.2 Demand spectra

Elastic demand spectrum can be generated based on the average value of the design

response spectra of historical earthquakes. Based on this elastic demand spectrum, two types of demand spectra were proposed to reflect the effects of strength reduction of a nonlinear SDOF system: highly damped demand spectra and inelastic demand spectra.

1.2.2.1 Elastic demand spectrum

Elastic demand spectrum can be generated by smoothing the response spectrum constituted by the average spectral acceleration of SDOF systems with different natural period of vibration. In addition, site type and system damping ratio also affect the elastic demand spectrum. Figure 1.3 demonstrates a typical elastic demand spectrum of a system with 5% damping ratio based on ASCE 7-10 (2010). S_{ae} represents the elastic spectrum acceleration of the structures with different natural periods of vibration.

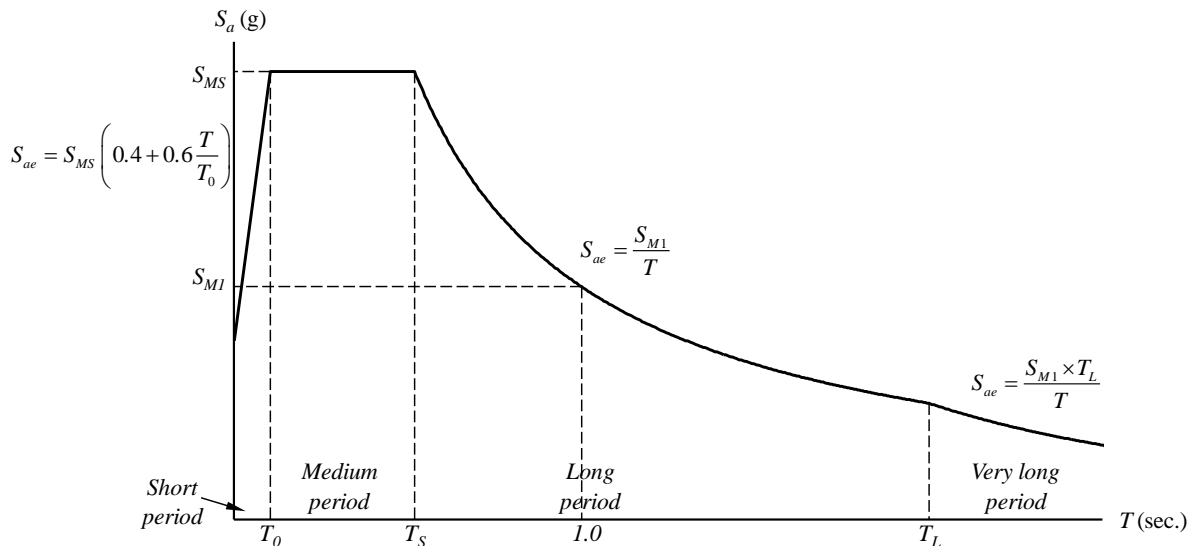


Figure 1.3 Elastic demand spectrum based on ASCE 7-10 (2010)

In Figure 1.3, S_{MS} and S_{M1} are respectively spectral response acceleration parameters at

short period (0.2 second) and at 1 second, and defined in Equations 1.1 and 1.2. T_0 , T_S and T_L are parameters used to separate short, medium, long and very long periods.

$$S_{MS} = F_a S_S \quad \text{Equation 1.1}$$

$$S_{M1} = F_v S_1 \quad \text{Equation 1.2}$$

where S_S and S_1 are maximum considered earthquake (MCE) acceleration parameters at short period and at 1 second; F_a and F_v are site modification parameters for short period and 1 second, respectively.

1.2.2.2 Highly damped demand spectra

To equivalent consider the effects of strength reduction on the deformation demand of a nonlinear system, Freeman (1998) used elastic demand spectra with a high damping ratio. In these elastic demand spectra, the spectral acceleration of the highly deamped elastic SDOF system was derived from the maximum nonlinear response of an inelastic SDOF system in a time-history analysis. The elastic and inelastic SDOF system should have identical natural period of vibration. Figure 1.4 demonstrates the typical highly damped demand spectra. However, this method has two major drawbacks (Krawinkler, 1992). First, no physical basis exists to prove a stable relationship between viscous damping and structural hysteretic energy dissipation, especially when the structure behaves highly inelastically. Second, the influence due to the changing in the natural period degradation is ignored in this method.

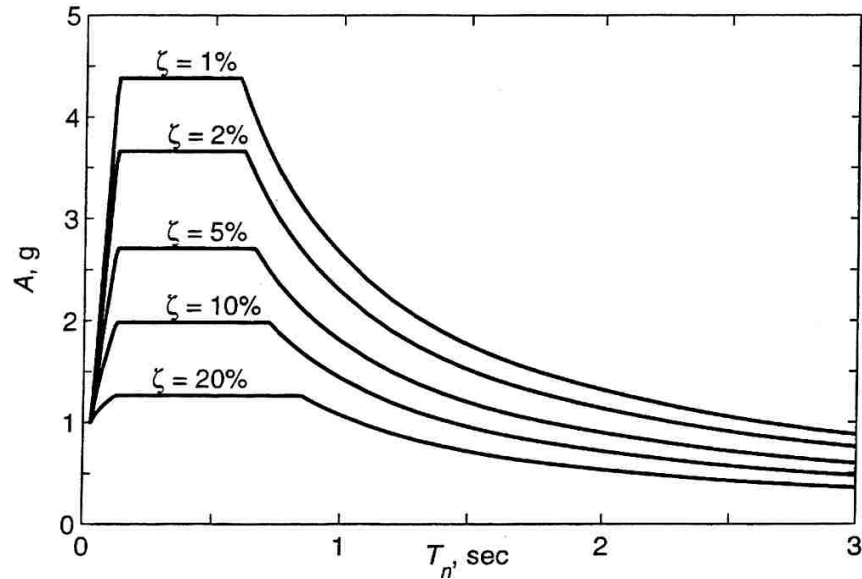


Figure 1.4 Highly damped demand spectra (Chopra, 2017)

1.2.2.3 Inelastic demand spectra

To overcome the weakness of highly damped demand spectra, inelastic response spectrum was proposed by some researchers, such as Veletsos et al. (1960, 1964), Newmark et al. (1969), and Murakami and Penzien (1975). The parameters used to derive an inelastic demand spectrum from an elastic demand spectrum are based on the statistical analysis of a SDOF system with a bilinear force-displacement relationship (Fajfar, 1999). This inelastic demand spectrum can more accurately estimate the peak nonlinear deformation than the highly damped demand spectrum, especially for structures with short periods or high ductility demand (Fajfar, 1999, 2002).

Reinhorn (1997) suggested highly damped demand spectra should be in spectra acceleration vs. spectra displacement format instead of the spectra acceleration vs. period format.

For an elastic SDOF system, the relationship among elastic spectral displacement, S_{de} , spectral acceleration, S_{ae} , and structural natural period of vibration, T , can be expressed by Equation 1.3.

Based on this equation, a smooth elastic demand spectrum in the spectral acceleration vs. period format can be transformed into spectral acceleration vs. spectral displacement format, as shown in Figure 1.5.

$$S_{de} = \frac{T^2}{4\pi^2} S_{ae} \quad \text{Equation 1.3}$$

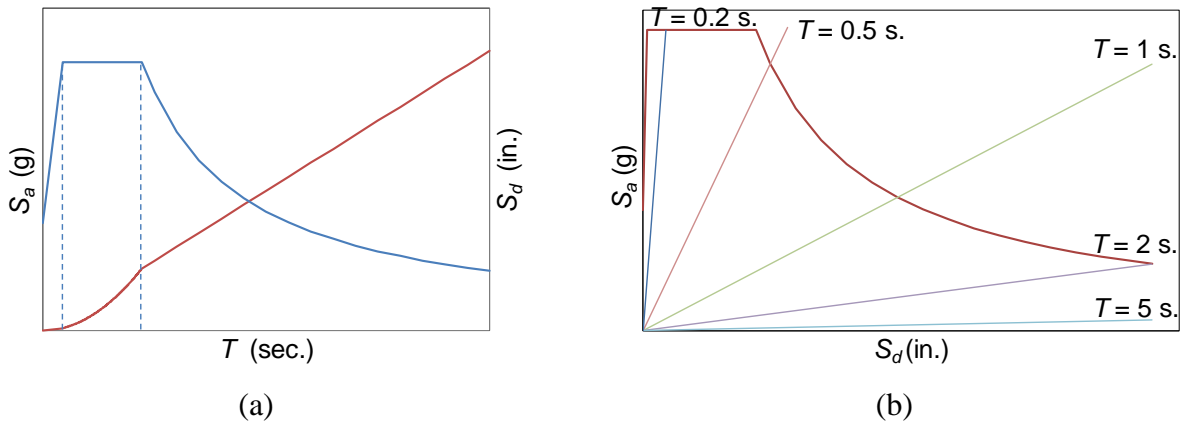


Figure 1.5 Elastic demand spectrum in different formats: (a) period vs. pseudo acceleration; (b) spectral displacement vs. spectral acceleration

The inelastic demand spectrum of a SDOF system with bilinear force-deformation relationship can be derived from the elastic demand spectrum based on Equations 1.4 and 1.5.

$$S_a = \frac{S_{ae}}{R_\mu} \quad \text{Equation 1.4}$$

$$S_d = \frac{\mu}{R_\mu} S_{de} = \frac{\mu}{R_\mu} \frac{T^2}{4\pi^2} S_{ae} = \mu \frac{T^2}{4\pi^2} S_a \quad \text{Equation 1.5}$$

where S_a and S_d are the spectral acceleration and displacement of inelastic demand spectra, respectively; T is structural natural period of vibration; R_μ is reduction factor considering strength reduction of inelastic system to allow hysteretic energy dissipation; μ is ductility factor, which is the ratio between the target displacement and the yield displacement of an equivalent bilinear capacity spectrum.

Based on Equations 1.4 and 1.5, the accuracy of an inelastic demand spectrum depends on the selection of appropriate values for R_μ and μ . Different versions of R_μ - μ - T relationship, used to calculate R_μ based on μ , were proposed in the past decades (Newmark and Hall, 1982; Nassar et al., 1992; Miranda and Bertero, 1994; and Vidic et al., 1994). Nevertheless, all these R_μ - μ - T relationship provided similar results (Chopra and Goel, 1999). Equations 1.6 to 1.9 describe the latest R_μ - μ - T relationship provided by Vidic (1994). Figure 1.6 obtained by this R_μ - μ - T relationship demonstrates the elastic demand spectrum and the inelastic demand spectra with different μ .

$$R_\mu = c_1 (\mu - 1)^{c_R} \frac{T}{T_0} + 1 \quad (T \leq T_0) \quad \text{Equation 1.6}$$

$$R_\mu = c_1 (\mu - 1)^{c_R} + 1 \quad (T \geq T_0) \quad \text{Equation 1.7}$$

$$T_0 = c_2 \mu^{c_T} T_1 \quad \text{Equation 1.8}$$

$$T_1 = 2\pi \frac{c_v v_g}{c_a a_g} \quad \text{Equation 1.9}$$

where c_1 , c_2 , c_R and c_T are hysteretic behavior parameters, which can be defined as 1.35, 0.75, 0.95 and 0.2 for bilinear hysteresis model with 5% mass damping model; a_g and v_g are the peak ground acceleration and velocity for a specified seismic hazard, respectively; c_v and c_a are amplification factors for v_g and a_g , and can be defined as 1.8 and 2.5 for structures with 5% damping ratio located in the U.S.

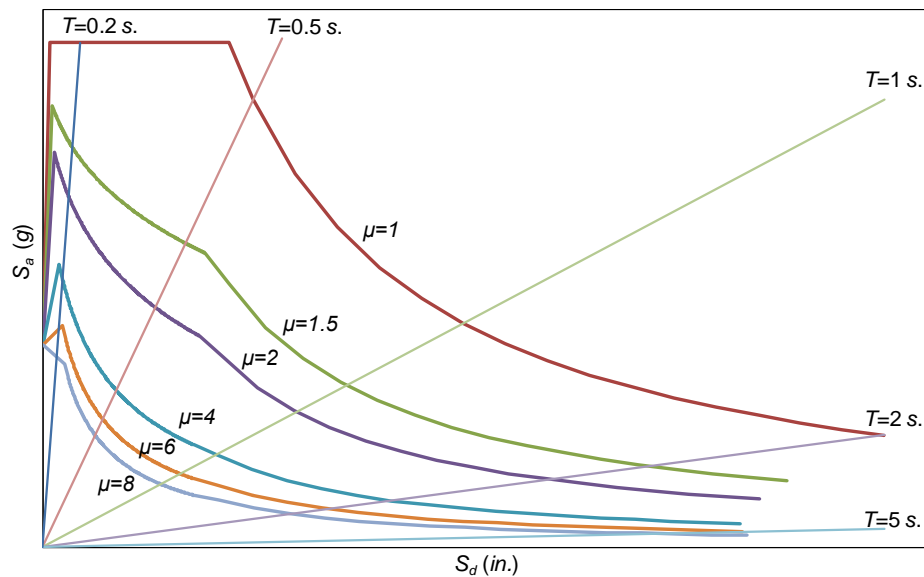


Figure 1.6 Elastic and inelastic demand spectra based on Vidic (1994)

1.2.3 Capacity spectrum

The capacity spectrum derived from a pushover analysis is used to predict structural nonlinear deformation demand in the capacity spectrum method. Figure 1.7 demonstrates the two

needed steps. First, pushover analysis is conducted on a MDOF system to obtain a top displacement vs. base shear curve (Figure 1.7(a) and 1.7(b)). Second, the top displacement vs. base shear curve for the MDOF system is transformed into a spectral displacement vs. spectral acceleration curve in an equivalent SDOF system (Figure 1.7 (c) and 1.7(d)).

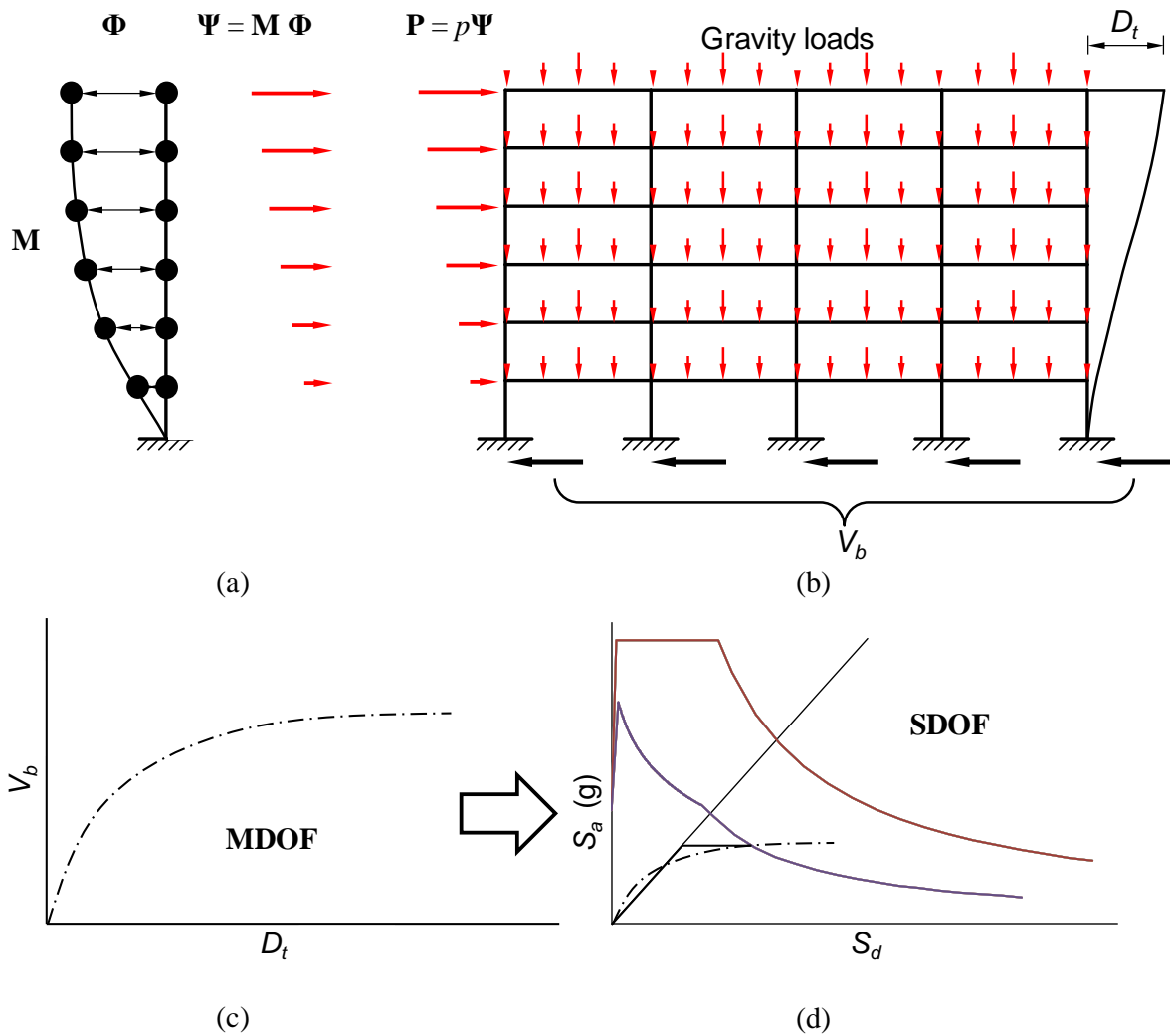


Figure 1.7 Pushover analysis and capacity spectrum establishment: (a) the first mode shape and the corresponding load pattern; (b) gravity and lateral loads; (c) top displacement vs. base shear curve of MDOF system; and (d) capacity spectrum curve of SDOF system, and demand spectra

1.2.3.1 Pushover analysis

In the pushover analysis, lateral forces are monotonically applied on the structure. The nonlinear behavior of the structure can be simulated by assigning distributed or concentrated plasticity to the structural elements. During lateral loading, inelastic elements start to yield and loss stiffness. Accordingly, the structure experiences stiffness degradation and behaviors nonlinearly. The overall structural stiffness is affected by the nonlinearity presented in each element. The most common measurement to reflect the overall nonlinear response of the structure is the top (roof) displacement vs. base shear response, as shown in Figure 1.7(c).

The horizontal loads applied on the structure in a pushover analysis follow a certain load pattern, as shown in Figure 1.7(b). Different load patterns have been suggested. The widely used one is related to the first mode shape of the structure, as shown in Figure 1.7(a). This is rational for the structures without abrupt changes of vertical strength or stiffness, since the first vibration mode dominates such structures. Some other versions of load pattern were proposed to consider higher mode effects (Park et al., 2007; Kreslin and Fajfar, 2012) or the variation of the load pattern over time due to the inelastic response of the structure subjected to ground motions (Gupta and Kunnath, 2000; Antoniou and Pinho, 2004).

Because the mass of each story is dominated by the slabs and the in-place stiffness of the slabs is extremely high, the multi-story structure shown in Figure 1.7(b) can be simplified as an lumped masses model with multiple lateral degrees of freedom (DOF) shown in Figure 1.7(a).

The lumped masses of the structure can be expressed by a diagonal matrix \mathbf{M} . The mode shape

of this lumped masses model, Φ , can be obtained by an eigenvalue analysis. Then the lateral load pattern used for the pushover analysis, \mathbf{P} , can be determined by Equation 1.10. The lateral load on the i^{th} floor, P_i , is expressed by Equation 1.11.

$$\mathbf{P} = p\mathbf{\Psi} = p\mathbf{M}\Phi \quad \text{Equation 1.10}$$

$$P_i = pm_i\Phi_i \quad \text{Equation 1.11}$$

where $\mathbf{\Psi}$ is lateral load pattern vector; p defines the magnitude of lateral load, and m_i and Φ_i are mass and mode shape on the i^{th} story.

1.2.3.2 Transformation between MDOF and SDOF system

The top displacement and base shear are used to reflect structural nonlinearity during lateral loading, as shown in Figure 1.7(c). However, this top displacement vs. base shear curve cannot be used together with the demand spectrum to predict structure deformation demand. This is because this curve is for a MDOF system, while equivalent demand spectrum is for a SDOF system. Therefore, a transformation of responses between the MDOF and SDOF systems is needed.

Based on the equation of motion and assuming that the mode shape remains constant, modal participation factor, Γ , is used to transform both the force and displacement of the MDOF system to those of the SDOF system (Fajfar 1996 and 1999). Equation 1.12 defines Γ , and the general mass of equivalent SDOF system, m^* , can be obtained by Equation 1.13.

$$\Gamma = \frac{\Phi^T \mathbf{M} \mathbf{1}}{\Phi^T \mathbf{M} \Phi} = \frac{\sum m_i \Phi_i}{\sum m_i \Phi_i^2} = \frac{m^*}{\sum m_i \Phi_i^2} \quad \text{Equation 1.12}$$

$$m^* = \Phi^T \mathbf{M} \mathbf{1} = \sum m_i \Phi_i \quad \text{Equation 1.13}$$

where Φ is mode shape; \mathbf{M} is mass matrix of the lumped mass on each floor; m_i and Φ_i are mass and mode shape on the i^{th} story; $\mathbf{1}$ is a unit vector. It is noted that Φ is normalized by proportionally modifying the mode shape vector until the roof displacement is equal to 1.

Top displacement, D_t , and based shear, V_b , of the MDOF system are transformed into general displacement, D^* , and general force F^* , of the equivalent SDOF system by Equations 1.14 and 1.15. The spectral acceleration corresponding to F^* is defined by Equation 1.16.

$$D^* = \frac{D_t}{\Gamma} \quad \text{Equation 1.14}$$

$$F^* = \frac{V_b}{\Gamma} \quad \text{Equation 1.15}$$

$$S_a = \frac{F^*}{m^*} \quad \text{Equation 1.16}$$

The capacity spectrum curve of SDOF system obtained based on the above derivation is shown in Figure 1.7(d). However, since the inelastic demand spectrum is used for a SDOF system with bilinear force-deformation relationship, the capacity spectrum shall also be transformed into a bilinear format based on energy equivalence.

1.2.4 Estimation of nonlinear deformation demand

After deriving an inelastic demand spectrum and an equivalent capacity spectrum in the SDOF system, an iterative procedure can be used to determine the intersection, which is used to

estimate the nonlinear deformation of the structure. Different methods of bilinear idealization have been proposed. All were based on energy equivalency, that is, the area enveloped by capacity spectrum should be identical to that enveloped by the bilinear equivalent capacity curve. Figure 1.8 shows three equivalent transformation methods, where K_{ini} and K_{eff} are the initial and effective structural stiffness; α is a strain hardening ratio for the post yield segment; S_{ay} and S_{dy} are yield acceleration and displacement; S_{ae} and S_{de} are elastic spectral acceleration and displacement; S_{ai} and S_{di} are strength and displacement at the intersection between the bilinear capacity spectrum and the non-linear demand spectrum.

The first method requires post yield stiffness be equal to zero, that is, no strain hardening is assumed. Additionally, the three curves (non-linear capacity curve, equivalent bilinear capacity curve and non-linear demand spectrum) intersect at the identical point, as shown in Figure 1.8(a). The second method requires the post-yielding stiffness be equal to zero, and the corresponding strength of the first intersection between the equivalent bilinear capacity curve and non-linear capacity curve be equal to 60% of the yield strength, as shown in Figure 1.8(b). The third method has a strain hardening, and the three curves intersect at the same point, as shown in Figure 1.8(c).

After the intersection between the capacity spectrum and the demand spectrum is determined, the demands of deformation and force, and some other information, such as the reduction factor, can be derived based on this intersection. The peak top displacement of the MDOF structure, D_t , can be obtained based on Equation 1.14 and the spectrum displacement, D^* .

All the external forces and element deformations are recorded in the pushover analysis for an

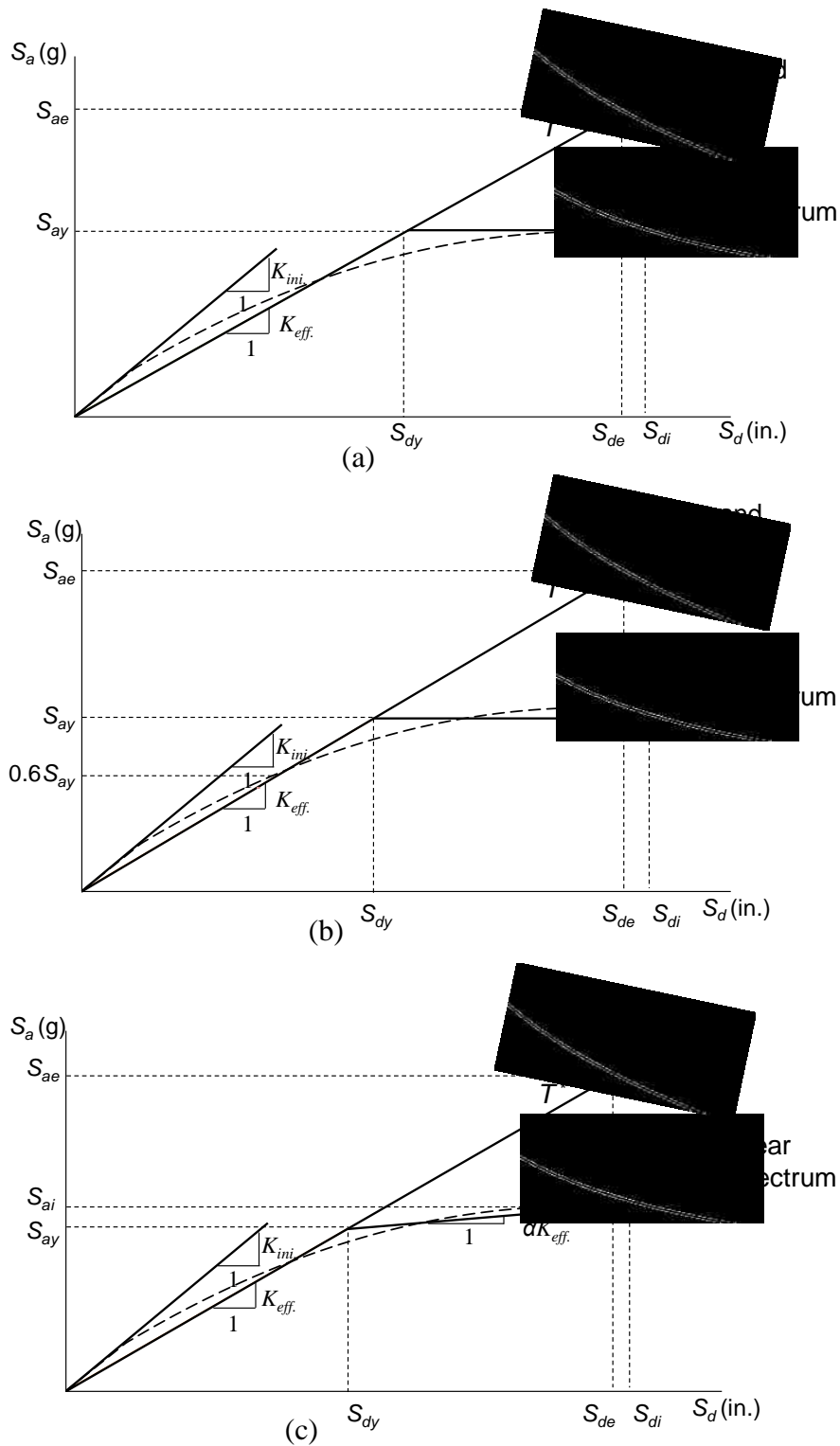


Figure 1.8 Different equivalent methods to transform non-linear capacity spectrum curve to equivalent bilinear capacity spectrum: (a) identical intersection and no post-yielding stiffness; (b) different intersections and no post yield stiffness; and (c) identical intersection and positive post-yielding stiffness

increasing D_t . Once D_t is determined, the corresponding records can be obtained. Furthermore, Equations 1.17 to 1.20 can be used to determine R_μ , μ and the elastic period of the equivalent bilinear SDOF system T^* .

$$R_\mu = \frac{S_{ae}}{S_{ay}} \quad \text{Equation 1.17}$$

$$\mu = \frac{S_{de}}{D_y^*} = \frac{S_{de}}{S_{dy}} \quad \text{Equation 1.18}$$

$$T^* = 2\pi \sqrt{\frac{m^* D_y^*}{F_y^*}} \quad \text{Equation 1.19}$$

$$F_y^* = S_{ay} m^* \quad \text{Equation 1.20}$$

where F_y^* and D_y^* are the yield strength and displacement of the equivalent bilinear SDOF system for capacity spectrum, respectively. In this study, the equivalent method shown in Figure 1.8(a) is adopted, because it can clearly define the factors of R - μ - T relationship (reduction factor, R_μ , ductility factor, μ , and equivalent structural period of bilinear SDOF system, T^*) for both demand and capacity spectra.

1.3 Displacement Coefficient Method

In addition to the capacity spectrum method, displacement coefficient method can be alternatively used to predict the maximum inelastic deformation of a structure. This method was suggested in FEMA-273 (1996) to ASCE/SEI 41-13 (2014) to estimate the target roof displacement, δ_t , based on the roof displacement vs. base shear curve derived from a pushover

analysis. ASCE/SEI 41-06 (2007) and ASCE/SEI 41-13 (2014) improved the displacement coefficient method used in FEMA-273 (1996). The equation used to calculate δ_t in ASCE/SEI 41-13 (2014) is shown in Equations 1.21 and 1.22.

$$\delta_t = C_0 C_1 C_2 S_a \frac{T_e^2}{4\pi^2} g \quad \text{Equation 1.21}$$

$$T_e = T_i \sqrt{\frac{K_i}{K_e}} \quad \text{Equation 1.22}$$

where C_0 is the modification factor to correlate the spectral displacement of an equivalent SDOF system with the roof displacement of the MDOF system; C_1 is a modification factor to relate the expected maximum inelastic displacements with the maximum displacements for the linear elastic system; C_2 is a modification factor to represent the effect of pinched hysteresis shape, cyclic stiffness degradation, and strength deterioration on the maximum displacement response; S_a is the response spectral acceleration at the effective fundamental period, T_e ; g is gravity acceleration; T_i is the elastic fundamental period of the structure; K_i is the elastic lateral stiffness of the building; K_e is the effective lateral stiffness of the building obtained by idealizing the pushover curve as a bilinear relationship. The details for calculating these factors can be found in ASCE/SEI 41-13 (2014). Similar to the capacity spectrum method, once δ_t is determined, the local deformation demands become available.

1.4 Direct Displacement-based Seismic Design Methods

Direct displacement-based design (DDBD) method starts from the target (allowable) displacement estimation of a structure under a selected hazard level or a selected performance level. The structure is designed to be capable of resisting the target displacement (Priestley et al., 2007; Welch et al., 2014). The seismic response of a structure is controlled by four quantities: strength, stiffness and ductility. Normally, in the direct displacement-based design method, one or two of these quantities is predetermined first to predict the target displacement demand. Then the other quantities are determined by assuming displacement capacity is equal or slightly larger than displacement demand (Fajfar 1999). The nonlinear displacement demand can be obtained based on displacement response spectrum and structural effective stiffness or period (Moehle, 1992; Sasani, 1998). Alternatively, the nonlinear displacement demand can be estimated based on the assumed displacement shape related to the inelastic first-mode at the design level of seismic excitation and the selected ductility (Priestley et al., 1996; Priestley et al., 2007). In a direct displacement-based design, the displacement capacity of a structure can be expressed and limited by either allowable material strain or inter-story drift ratio. One drawback of direct displacement-based design method is that this method designs structure based on only one performance objective; thus, an iteration method may have to be used to modify structural capacity so that the other performance objectives can be satisfied. The following sections briefly describe the existing direct displacement-based design methods used for structural walls, SDOF bridge piers and MDOF RC moment frames.

1.4.1 Structural wall

Sasani (1998) proposed a direct displacement-based design method for RC structural walls resisting strong ground motions, as shown in Figure 1.9. First, this method designs a RC wall under frequent earthquakes based on the traditional force-based method. At this hazard level, the structure is expected to remain elastic, and its design is controlled by the deformation requirements of the non-structural elements. Second, a direct displacement-based design is used to estimate the structural deformation demand at the life safety performance level. Setting the structural deformation capacity to be identical to the deformation demand, the concrete compressive strain related to deformation capacity is checked. If this strain is larger than the allowable value, then the design should be modified until the concrete strain is no more than its limit. Finally, the base shear was checked to avoid an unexpected failure mode. The details of this method are described below.

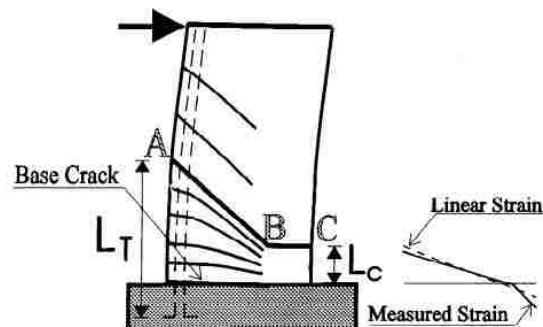


Figure 1.9 Fanned radially-cracked region at the bottom of a structural wall and schematic strain distribution at the base (Sasani 1998)

The nonlinear deformation demand of a RC structural wall was assumed as 1.5 times of the elastic deformation demand, which could be determined by the displacement response spectra and an estimated structural fundamental period, T . T of the structure with N pieces RC wall was obtained by Equation 1.23.

$$T = 1.8H^2 \sqrt{\frac{\bar{m}}{\sum_{i=1}^N EI_{eq}}} \quad \text{Equation 1.23}$$

where H = wall total height; \bar{m} = the average linear mass along wall height; and EI_{eq} = estimated equivalent flexural stiffness.

The equal displacement rule assumes that the peak inelastic deformation of a structure under a strong ground motion is equal to the peak elastic deformation if the structure remains elastic. However, based on the study by Wallace and Moehle (1992), the equal displacement rule is not suitable for RC structural walls, and the ratio between the inelastic deformation and the elastic deformation shall be 1.5. This ratio was adopted in the direct displacement-based design method for walls. The deformation capacity at the top of the RC wall, Δ_c^t , was expressed as:

$$\Delta_c^t = \frac{\Phi_y H^2}{3.6} + (\Phi_u - \Phi_y) L_p (H - L_p / 2) \quad \text{Equation 1.24}$$

where Φ_u and Φ_y are the yield and ultimate curvatures of the section; and H and L_p are wall total height and plastic hinge length. Φ_y can be calculated as $\Phi_y = M_u / EI_{eq}$, where M_u is section

ultimate moment capacity. Φ_u can be obtained by section analysis under cyclic loading when the maximum usable concrete strain is reached. Note, compared with Equation 1.24, the code design provisions may overestimate the displacement capacity of the RC structural wall by 100%.

1.4.2 SDOF systems

Moehle (1992) proposed a direct displacement-based design method for SDOF RC structures as shown in Figure 1.10(a). The equal displacement rule was used to predict the inelastic deformation demand. Elastic response spectrum, shown in Figure 1.10(c), was used to predict elastic deformation demand based on the estimated structural period related to effective structural stiffness. Deformation capacity was expressed by allowable material strain.

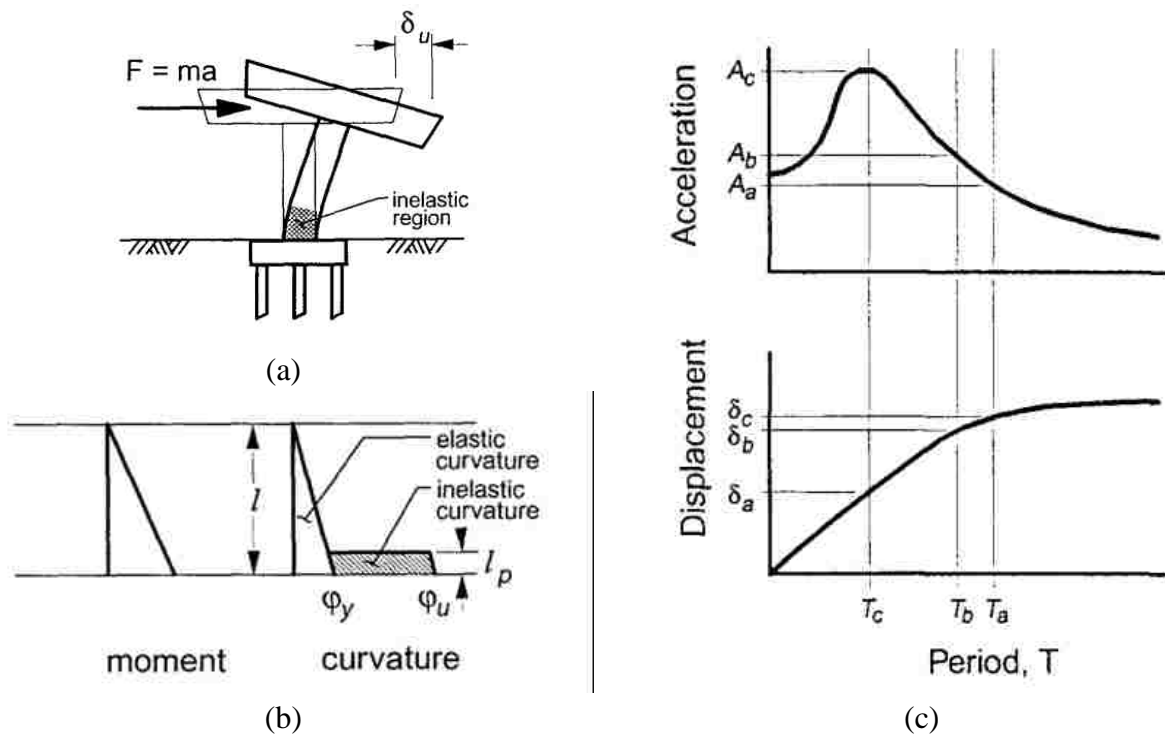


Figure 1.10 Schematic diagram in Moehle (1992): (a) SDOF RC bridge pier; (b) idealized flexural curvature; (c) elastic response spectrum

The flexural deformation capacity of a SDOF bridge pier shown in Figure 1.10 could be determined using Equation 1.25 proposed by Priestley and Park (1987).

$$\delta_u = \frac{\varphi_y l^2}{3} + (\varphi_u - \varphi_y) l_p \left(l - \frac{l_p}{2} \right) \quad \text{Equation 1.25}$$

where δ_u is ultimate displacement capacity; l and l_p are column height and plastic hinge length; φ_u and φ_y are ultimate and yield curvatures of plastic hinge, respectively. φ_y can be neglected if an idealized bilinear force-displacement model is used. φ_u can be determined by allowable material strain, controlled by either the maximum usable concrete compression strain or the longitudinal reinforcement tensile strain.

1.4.3 MDOF systems

Goel et al. (2008 and 2010) suggested a direct displacement-based design method for MDOF frame structures based on the beam hinging mechanism shown in Figure 1.11 and a pre-selected target drift. An equivalent energy method was used to determine the required base shear force for different hazard levels. Therefore, multiple performance targets could be considered simultaneously by selecting the largest base shear for design. Then the design base shear was distributed vertically on each floor. A plastic design method was adopted to design beam components based on the virtual work principle. The design base shear of one performance objective, V_y , is calculated based on Equations 1.26 to 1.28.

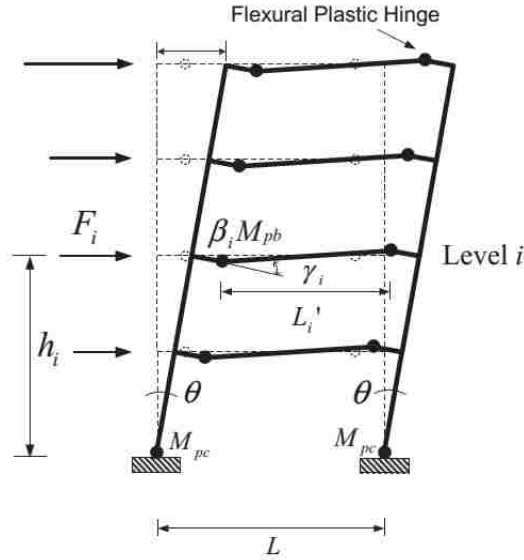


Figure 1.11 Target yield mechanism for moment frame (Goel et al. 2010)

$$V_y = \frac{-\alpha + \sqrt{\alpha^2 + 4\gamma S_a^2}}{2} W \quad \text{Equation 1.26}$$

$$\alpha = \sum_{i=1}^N \lambda_i h_i \times \frac{\theta_p 8\pi^2}{T^2 g} \quad \text{Equation 1.27}$$

$$\gamma = \frac{2\mu - 1}{R_\mu^2} \quad \text{Equation 1.28}$$

where α reflects the target deformation demand; γ is an energy modification factor; S_a is the design acceleration of one hazard level; θ_p represents the inter-story drift limit of one performance level; W is total weight; T is structural vibration period; λ_i and h_i are story height of the i^{th} story and the corresponding distributed lateral load; R_μ is a strength reduction factor; and μ is ductility ratio. The base shear of a performance target can be calculated according to the selected hazard level and the desired performance level reflected by S_a and θ_p , respectively.

Then the design base shear, controlled by one of the multiple performance objectives, was distributed vertically to each story considering the influence of higher mode and structural nonlinearity, as shown in Equations 1.29 and 1.30.

$$F_i = (\beta_i - \beta_{i+1}) \left(\frac{w_n h_n}{\sum_{j=1}^n w_j h_j} \right)^{0.75T-0.2} V_y \quad \text{Equation 1.29}$$

$$\beta_i = \left(\frac{\sum_{j=i}^n w_j h_j}{w_n h_n} \right)^{0.75T-0.2} \quad \text{Equation 1.30}$$

where F_i is the distributed lateral force at the i^{th} story; β_i is a base shear distribution factor for the i^{th} story; and w_j and h_j are the weight and height of the j^{th} story.

Finally, the plastic design method is used to design the yield strength of the beams according to the distributed lateral loads. Virtual work principle is used by assuming the external work caused by the distributed lateral load is equal to the internal virtual work caused by the plastic hinge rotation at beam ends, as shown in Equation 1.31.

$$\sum_{i=1}^n F_i h_i \theta = 2M_{pc} \theta + \sum_{i=1}^n 2(\beta_i M_{pb}) \frac{L}{L'_i} \quad \text{Equation 1.31}$$

where θ represents the target plastic hinge rotation angle of the structure shown in Figure 1.11; M_{pb} and M_{pc} are the design yield moments of the beams and the columns; L and L'_i are the total

and clear lengths of a beam. M_{pc} can be determined based on beam-hinge mechanism to avoid a weak story. The design procedure based on Figure 1.11 implied that plastic hinges appeared at each beam end and rotate with same angle under a strong earthquake, which may not be true.

1.4.4 Drawback of direct displacement-based seismic design method

Even though direct displacement-based design is considered a PBSB method, some disadvantages exist. First, economy is a basic demand of PBSB method (Krawinkler, 1999), but not directly involved in the existing direct displacement-based design methods. Moreover, more accurate structural analysis methods shall be used to predict the nonlinear deformation of a structural system and its elements, which are affected by not only strength but also stiffness. However, the current direct displacement-based design methods design the member strength based on a preselected or estimated stiffness. Therefore, an optimal PBSB method, which provides a strategy to design both element strength and stiffness based on target nonlinear structural performance, is desired.

1.5 Optimal Performance-based Seismic Design Methods

The conventional PBSB alternately performs structural analysis and design until all the performance objectives are satisfied. Optimal seismic design provides a mean to determine which and how the design variables shall be modified (Plevris, 2012) so that the structure would satisfy not only the design requirements but also a predefined optimal objective. An optimal PBSB normally requires an algorithm to achieve the optimal design objective for a structure

satisfying various constraints. The optimal design objective can be the minimum construction cost, floor acceleration or structural damage. The architectural constraints can be the upper or lower bound of design variables, such as section size. The performance-based structural constraints can be the allowable forces or deformations for different performance levels, such as the allowable inter-story drift ratios shown in Table 1.1. An optimal PBSO problem can be expressed using Equations 1.32 to 1.34.

$$\text{Minimize or Maximize } Z = f(\mathbf{X} = (x_1, x_2, \dots, x_i, \dots, x_n)) \quad \text{Equation 1.32}$$

$$\text{Subject to } R(\mathbf{X})^h \leq R_{Lim}^p \quad (h = 1, \dots, H; p = 1, \dots, P) \quad \text{Equation 1.33}$$

$$x_i^L \leq x_i \leq x_i^U \quad (i = 1, \dots, n) \quad \text{Equation 1.34}$$

where Z and f are objective function and its expression; \mathbf{X} is a vector of design variables with x_i being the i^{th} design variable; $R(\mathbf{X})^h$ is the structural response (force or deformation) under the h^{th} hazard level; R_{Lim}^p is the allowable value of structural response in the p^{th} performance level; x_i^L and x_i^U are the upper and lower bounds of the i^{th} design variable; and n , H and P are the total number of design variables, hazard levels and performance levels.

An optimal PBSO consists of three basic components: an objective function, constraints, and an optimization algorithm. Two types of objective function have been considered: single objective function and multi-objective function. The constraints can be divided into two categories: deterministic constraints and probabilistic constraints. The detailing requirements of seismic design to achieve desired failure mechanism, such the minimum reinforcement ratio, can

be used as supplemental constraints. Various optimal algorithms have been proposed for optimal PBSB; nevertheless, they mainly fall into two categories: metaheuristics method and optimality criteria (OC) method.

1.5.1 Optimal objectives

Single objective function minimizing the total construction cost was widely used in optimal PBSBs (Mohharrami and Grierson, 1993; Soegiarso and Adeli, 1997; Ganzerli et al., 2000; Liang et al., 2002; Lee et al., 2002; Talatahari et al., 2014; Kaveh and Nasrollahi, 2014 and Gholizadeh, 2015). The material cost occupies a large portion of construction cost. Therefore, minimizing was often adopted as the single optimal objective and can be expressed by Equation 1.35.

$$\text{Minimize } Z = \sum_{j=1}^M c_j \rho_j \sum_{i=1}^N (A_{ij} \times l_{ij}) \quad \text{Equation 1.35}$$

where Z is the total material cost; c_j and ρ_j are unit cost and density of material j ; A_{ij} and l_{ij} are section area and length of component i made by material j ; M and N are total types of material and total number of component, respectively.

Different types of multi-objective function were also considered. Xu et al. (2006) proposed a multi-objective function for steel buildings, which simultaneously minimizes total structural weight and damage. Because structural weight and damage cannot be added, they were transformed into two unitless objectives, as shown in Equation 1.36.

$$\text{Minimize } Z = f_1 + f_2 = \omega_1 \frac{\sum_{j=1}^n \rho L_j A_j}{W_{\max}} + \omega_2 \left\{ \left(\frac{1}{ns} \right) \sum_{s=1}^{ns-1} \left[\left(\frac{v_s(x)}{\Delta(x)} \right) \left(\frac{H}{H_s} \right) - 1 \right]^2 \right\}^{0.5} \quad \text{Equation 1.36}$$

where Z is the optimal objective minimizing element weight and structural damage together; f_1 and f_2 are unitless weight and damage objectives, respectively; ω_1 and ω_2 are combination factors defined by Gong (2003); ρ represents material density; L_j and A_j are the length and cross section area of member j ; W_{\max} is the assumed maximum possible weight; ns is the total number of stories; $v_s(x)$ and H_s are lateral drift and height in the s^{th} story; and $\Delta(x)$ and H are roof lateral drift and total structural height, respectively.

In Equation 1.36, the weight objective is normalized by the maximum possible weight, while the damage objective is normalized based on equal inter-story drift expectation. This expectation believes that structure would suffer least damage if the inter-story drift ratio is identical among different stories (Chopra 1999). Therefore, in Equation 1.36, roof drift ratio is used as the standard measurement to evaluate the degree of inter-story drift uniformity. Both weight objective and damage objective are unitless, and can be optimized simultaneously to consider the conflict between construction budget and possible loss during earthquakes.

Zou et al. (2007) proposed a multi-objective function for RC frames to minimize the life-cycle cost of a structure, including both initial material cost and expected future damage loss.

Equation 1.37 shows the objective function as:

$$\begin{aligned}
\text{Minimize } Z &= f_1 + f_2 = (f_{1c} + f_{1s}) + \left(\sum_{r=1}^{N_r} P_r L_r \right) \\
&= \left[\sum_{i=1}^{N_i} w_{ci} (L_{ci} b_{ci} d_{ci}) + \sum_{i=1}^{N_i} w_{si} (L_{si} \rho_i + L'_{si} \rho'_i) \right] + \left\{ \sum_{r=1}^{N_r} P_r \left[\sum_{q=1}^5 L_q (A_q) \right]_r f_1 \right\}
\end{aligned} \tag{Equation 1.37}$$

where f_1 and f_2 are the initial material cost and the expected future damage loss; f_{1c} and f_{1s} are initial material cost of concrete and reinforcement; L_r and P_r represent the system failure loss and the corresponding occurrence probability; w_{ci} and w_{si} are unit material cost of concrete and reinforcement; L_{ci} , L_{si} and L'_{si} are the lengths of the i^{th} component, the tension reinforcement and the compression reinforcement; b_{ci} and d_{ci} are the width and depth of the i^{th} component; ρ_i and ρ'_i are the tension and compression reinforcement ratios of the i^{th} component; L_q is total structural cost including direct and indirect losses; A_q is damage status classified into five types; and r is the number of total selected performance levels.

In Equation 1.37, the initial material cost is related to the total weight of all types of material; the expected future damage is related to the initial material cost, and evaluated in five aspects. The expected future damage loss includes direct loss, such as repairing or replacement cost, and indirect loss, such as structural malfunction.

1.5.2 Optimization constraints

The preselected constraints that the solution of an optimal PBSO problem must satisfy defines the boundary separating the allowable and undesired systems. The multi-dimensional space of the design variables enveloped by the constraints is called as feasible region. Two types of PBSO constraints have been adopted in the optimal PBSO problems: deterministic constraints

and probabilistic constraints. The former defines a feasible region, in which the structures with deterministic design variables satisfy the performance-based constraints. The latter defines a feasible region, in which a structure with probabilistic distributed design variables satisfies the allowable failure probability of different performance levels. The structure in this multi-dimensional feasible region is not defined by the value of design variables, but their mean values. The values of design variables are changeable during optimal process following a distribution type with the deterministic mean and variance. Therefore, the structural responses under the possible values of a design variable are different. The failure probability of the structure with uncertain variables can be obtained by a statistical analysis.

1.5.2.1 Deterministic constraints

The limit state function of the deterministic constraints used to avoid structural failure can be expressed by Equation 1.38.

$$G(\mathbf{X}) = [R^p] - R(\mathbf{X})^h \quad \text{Equation 1.38}$$

where \mathbf{X} is the vector of design variables; $R(\mathbf{X})^h$ is the non-linear response of structure with \mathbf{X} under the h^{th} selected hazard level; $[R^p]$ represents the deformation limit of the p^{th} performance levels; $G(\mathbf{X})$ defines the limit state function of \mathbf{X} for the p^{th} performance level under the h^{th} hazard level. The performance level and corresponding hazard level are predefined according to Figure 1.1. Each combination of a performance level and a hazard level is called a performance objective. All selected performance objectives shall be achieved.

Normally, nonlinear deformation instead of the force or acceleration of structure is selected as the constraints for an optimal PBSO problem. Two types of non-linear deformation are considered in optimal PBSO: inter-story drift ratio and plastic hinge rotation, as expressed as:

$$\Delta \leq [\Delta] \quad \text{Equation 1.39}$$

$$\theta \leq [\theta] \quad \text{Equation 1.40}$$

where Δ and $[\Delta]$ are inter-story drift ratio of the structure and corresponding limits; θ and $[\theta]$ are plastic hinge rotation of columns or beams and its limits.

1.5.2.2 Probabilistic constraints

Uncertainty exists in external loads, material properties, construction, and numerical analysis. The failure probability of a structural caused by these uncertainties can be quantified by structural reliability analysis, which identifies the failure probability of the structure using models with discrete input variables following certain probability distributions.

The limit state function of the deterministic constraints defined in Equations 1.39 and 1.40 includes inter-story drift, and plastic hinge rotation of beams and columns. A structure fails when any one of these limit state functions is unsatisfied, that is the structure model shall be taken as a series system. Therefore, structure failure probability derived from probability analysis can be defined as Equation 1.41.

$$P[G(\mathbf{X}) \leq 0] = P\left[\left(\Delta^h \geq [\Delta]^p\right) \cup \left(\theta^h \geq [\theta]^p\right)\right] = \Phi(-\beta) \quad \text{Equation 1.41}$$

where \mathbf{X} is the vector of the design variables; $G(\mathbf{X})$ is limit state function of the deterministic deformation constraint with \mathbf{X} ; $P[]$ is conditional probability; symbol \cup expresses the union of two condition subsets; $\Phi()$ is the standard normal distribution function, which has zero mean and unit variance; β is the reliability index of non-linear deformation of structure.

The probabilistic format of the deformation constraints can be defined as that the failure probability in limit state function is lower than its limit, as shown in Equation 1.42 or 1.43.

$$P[G(\mathbf{X}) \leq 0] \leq [P^p] \quad \text{Equation 1.42}$$

$$\beta \geq [\beta^p] \quad \text{Equation 1.43}$$

where $[P^p]$ is the allowable failure probability of the nonlinear deformation of structure in the p^{th} performance level; $[\beta^p]$ is the allowable reliability index of non-linear deformation of structure under in the p^{th} performance level.

To date, only SEAOC (1995) proposed the acceptable failure probability of structural in deferent performance levels, which was based on the study of Paulay and Priestley (1992) and shown in Table 1.3. In this table, $[P_{f,a}]$ and $[\beta_{j,a}]$ are the allowable annual failure probability and the reliability index; $[P_{f,E}]$ and $[\beta_{j,T}]$ are the allowable failure probability and the reliability index of period (normally 50 years).

Table 1.3 Target annual probabilities of nonperformance recommended by Paulay and Priestley (1992)

Performance level	$[P_{f,a}]$	$[\beta_{j,a}]$	$[P_{fE}]$	$[\beta_{jE}]$
Operational	0.0200	2.054	0.100	1.276
Life safety	0.0020	2.878	0.010	2.326
Collapse prevention	0.0002	3.540	0.001	3.090

1.5.3 Optimal algorithms

The two major optimization algorithms for PBSO are metaheuristics and optimality criteria (OC) methods. The metaheuristics method treats the optimal variables of a structure as the variables of an object in natural world or a social phenomenon, and imitates a searching mechanism for an optimal design following the natural phenomena or societal laws. The advantage of this method is that it requires neither explicit expression of the constraints, nor the explicit formulations of the searching path for the optimal solution. Nevertheless, great computational effort is required to simulate the searching mechanism.

In contrast, OC method requires much less computational effort, but needs explicit constraints defined by the optimal variables. The optimal PBSO is then transformed to a nonlinear programming problem, which can be solved by diverse mathematical methods. The efficiency of these mathematical methods depends on the path of searching optimal solution.

1.5.3.1 Metaheuristics methods

The metaheuristics methods adopted in the optimal PBSO problems include genetic algorithm (Liu et al., 2005; Kaveh et al., 2012), ant colony algorithm (Kaveh et al., 2010), neural networks algorithm (Möller et al., 2009), particle swarm algorithm (Talatahari, 2013; Gholizadeh

and Moghadas, 2014), charged system search algorithm (Talatahari et al., 2014), and discrete gravitational search algorithm (Yazdani et al., 2016). The gravitational search algorithm employed by Yazdani et al. (2016) is described here to demonstrate how the structure variables are encoded by the natural objects and how the natural phenomenon is used to search the optimal solution. Gravitational search algorithm was first proposed by Rashedi et al. (2009) to search optimal solution based on Newton's law of gravity and the law of motion defined in Equations 1.44 and 1.45.

$$F = G \frac{M_1 M_2}{R^2} \quad \text{Equation 1.44}$$

$$a_1 = \frac{F}{M_1} \quad \text{Equation 1.45}$$

where F is the universal gravitation between two objects; G is the gravitational constant; M_1 and M_2 are the masses of two objects; R is the interval between the two objects; a_1 and M_1 are the acceleration and the mass of the first object.

The gravity law states that the universal gravitation between two objects in the space is proportional to their masses, and inversely proportional to the square of their interval. The law of motion indicates that the acceleration of one objective is proportional to the external force applied on it and inversely proportional to its mass. To apply these natural laws, the gravitational search algorithm assumed that a space with N dimensions includes finite objects. The location vector of the i^{th} object, X_i , is expressed in Equation 1.46.

$$X_i = (x_i^1, \dots, x_i^d, \dots, x_i^n) \quad \text{Equation 1.46}$$

where x_i^d is the position of the i^{th} object in the d^{th} dimension. The number of space dimension shall be equal to the number of the optimal variables. Therefore, each position in this space is a possible solution of optimal PBSO. In the other word, the location of a position in the i^{th} dimension represents the value of the i^{th} design variable.

These objects move in the N -dimension space based on the Newton's law of gravity and the law of motion. Each object experiences universal gravitations from all other objects in the space, as shown in Figure 1.12. The resultant force, F_1 , determines the object's motion direction. The acceleration of this object is determined by the external force and its own mass. The initial masses of all objects are identical but modified during the searching process based on a fitness function. For the objects close to the optimal solution, their masses increase at the current time

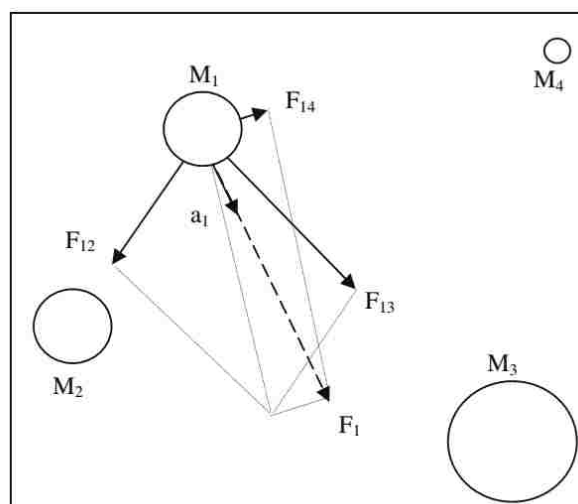


Figure 1.12 The combined universal gravitation force and the universal gravitations caused by the other masses (Rashedi et al., 2009)

step, while the masses of other objects decrease simultaneously. With the additional mass, the object has larger attraction to other objects, and its speed is reduced. Nevertheless, this trend is opposite for other objects, which are far from the optimal solution. Finally, all the objects will stop around the heaviest one, which has the ultimate value of fitness function and represents the optimal design solution. The modified masses of the i^{th} object at searching time, t , is shown in Equations 1.47 and 1.48.

$$M_i(t) = \frac{m_i(t)}{\sum_{j=1}^N m_j(t)} \quad \text{Equation 1.47}$$

$$m_i(t) = \frac{fit_i(t) - worst(t)}{best(t) - worst(t)} \quad \text{Equation 1.48}$$

where $m_i(t)$ and $M_i(t)$ are the inertial and gravitational masses of the i^{th} object at time t ; $fit_i(t)$ is the fitness value of the i^{th} object at time t ; $worst(t)$ and $best(t)$ are the highest and lowest (or inverse depending on the objective function) fitness value among all objects.

The computational effort of any metaheuristics method is considerably high. For instance, Kaveh et al. (2010) applied both ant colony optimization algorithm (ACO) and genetic algorithms (GA) to the optimal PBSB of two plane steel moment frames shown in Figure 1.13. The time required at each iteration step was almost identical for two algorithms, thus the computational cost depended only on the required number of iteration. To decrease the design variables, 27 members in the 3-story frame (Figure 1.13(a)) were unified into five groups, and

108 members in the 9-story frame (Figure 1.13(b)) were unified into 13 groups. Thus, this method does not deliver a global optimal design.

For the 3-story steel moment frame, the required analysis rounds of ACO and GA were 3900 and 6800, respectively. The optimal weight obtained from ACO was 6.79% lighter than from GA. The standard deviation of the results obtained from the ACO and GA algorithms were 1.701 kips and 3.222 kips, respectively. The 9-story frame was optimized for two cases. For the

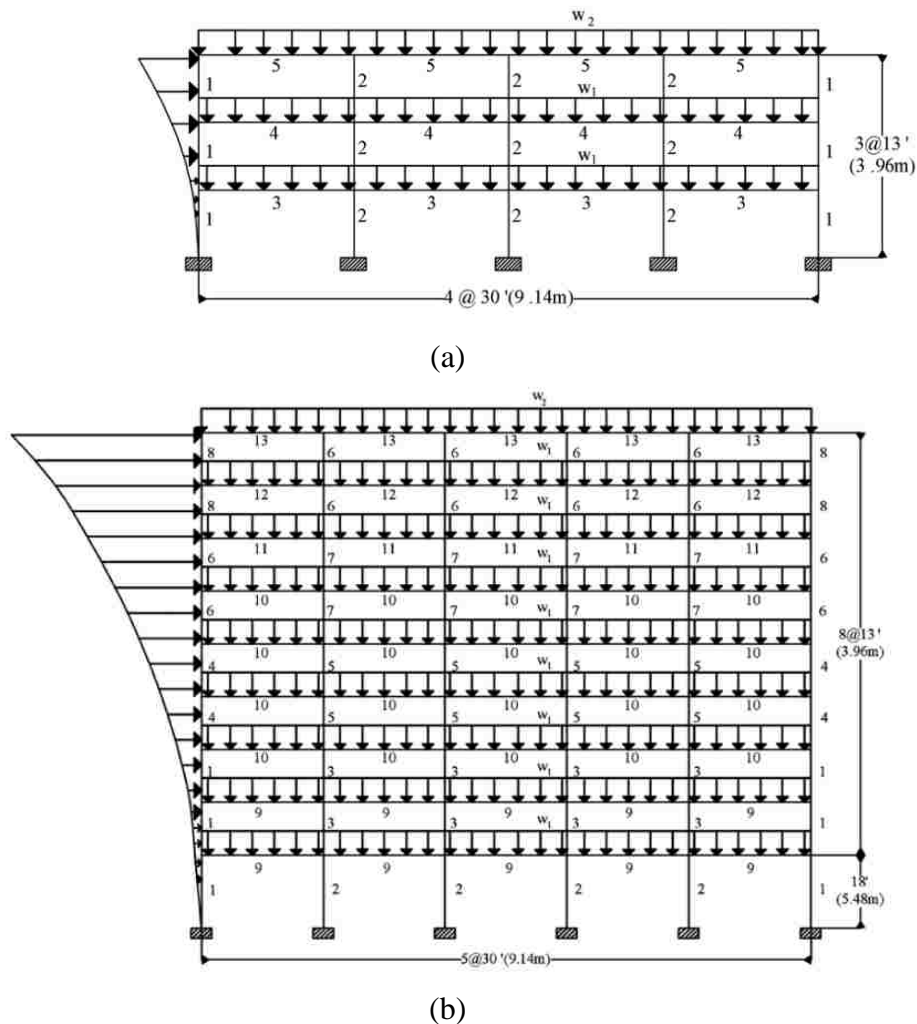


Figure 1.13 Two steel frame examples in the study of Kaveh et al. (2010): (a) Three-story four-bay planar steel moment frame; (b) Nine-story five-bay planar steel moment frame

first case, both beams and columns were taken as optimal variables. For the second case, only beams are optimized with predetermined columns. The required analysis rounds for the first case were respectively 7000 for ACO and 11500 for GA algorithms. For the second case, the needed analysis rounds were 5600 and 9700 for ACO and GA algorithms, respectively. Therefore, without a fully automated design process, these metaheuristics methods are difficult to be used in the engineering practice due to the high computational cost.

1.5.3.2 OC methods

OC method is a type of gradient-based method that determines searching direction and speed based on the gradient of constraints, which can be explicitly expressed by design variables based on some simplifications. The key challenge existing in OC method is how to transform a structural optimization problem with implicit constraints, which cannot be explicitly formulated by the optimal variables, into a nonlinear programming problem with explicit constraints. The challenge was tackled by some researchers. Grierson et al. (2006) and Xu et al. (2006) proposed a performance-based OC method for steel moment frames with a multi-objective function shown in Equation 1.36. For steel structures, the stiffness and strength of an element are determined by section characteristics, such as the moment of inertia, I , elastic modulus, S , and plastic modulus, Z . This OC method expressed all these section characteristics only by section sizes A , as shown in Equations 1.49 to 1.51.

$$I = C_1 A^2 + C_2 A + C_3$$

Equation 1.49

$$S = C_4 A + C_5 \quad \text{Equation 1.50}$$

$$Z = \zeta S \quad \text{Equation 1.51}$$

where C_1 to C_5 are constants determined by a regression analysis (Gong, 2003); and ζ is a shape factor depending on the cross-section type.

The allowable values of inter-story drift ratio and roof displacement as well as the upper and lower bounds of section size were considered as constraints, as shown in Equations 1.52 to 1.54. Equation 1.36 was used to define an objective function. However, the second part of the multi-objective function in Equation 1.36 and the nonlinear deformation constraints shown in Equations 1.52 and 1.53 were implicit with respect to A . Therefore, the first-order Taylor series were used to reformulate the objective function and constraints into Equations 1.55 to 1.58. The implicit objective function and constraints were formulated by reciprocal sizing variables, $x = 1/A$, and sensitivity coefficients of inter-story drift ratio, roof displacement and ductility-demand, $d\delta/dx_j$, $d\Delta/dx_j$ and df_2/dx_j . The definition of x can be found in the study by Schmit and Farshi (1974). The method to calculate the sensitivity coefficients was proposed by Gong et al. (2005). Therefore, the optimal PBSO problem was transformed to a nonlinear programming problem with the objective function and constraints explicitly expressed by A .

$$\text{Subject to: } \delta_s^i(x) \leq [\delta^i] \quad (i = 1, \dots, n_h; s = 1, \dots, n_s) \quad \text{Equation 1.52}$$

$$\Delta^i(x) \leq [\Delta^i] \quad (i = 1, \dots, n_h) \quad \text{Equation 1.53}$$

$$[A_j^L] \leq A_j \leq [A_j^U] \quad (j = 1, \dots, n) \quad \text{Equation 1.54}$$

where δ_s^i and $[\delta^i]$ are the inter-story drift ratio on the s^{th} story and its allowable value at the i^{th} hazard level; Δ^i and $[\Delta^i]$ are roof displacement and its allowable value at the i^{th} hazard level; A_j , $[A_j^L]$ and $[A_j^U]$ are the cross sectional area and its lower- and upper bound values of the j^{th} component; n_h , n_s and n are the number of the hazard level, stories and components.

Minimize: $f(x) = f_1 + f_2$

$$= \frac{\omega_1}{W_{\max}} \sum_{j=1}^n \rho L_j \frac{1}{x_j} + \omega_2 \left\{ [f_2(x)]^0 + \sum_{j=1}^n \left[\frac{df_2(x)}{dx_j} \right]^0 (x_j - x_j^0) \right\}^{CP} \quad \text{Equation 1.55}$$

$$\text{Subject to: } [\delta_s^i(x)]^0 + \sum_{j=1}^n \left[\frac{d\delta_s^i(x)}{dx_j} \right]^0 (x_j - x_j^0) \leq [\delta^i] \quad (i = 1, \dots, n_h; s = 1, \dots, n_s) \quad \text{Equation 1.56}$$

$$[\Delta^i(x)]^0 + \sum_{j=1}^n \left[\frac{d\Delta^i(x)}{dx_j} \right]^0 (x_j - x_j^0) \leq [\Delta^i] \quad (i = 1, \dots, n_h) \quad \text{Equation 1.57}$$

$$[x_j^L] \leq x_j \leq [x_j^U] \quad (j = 1, \dots, n) \quad \text{Equation 1.58}$$

where the superscript 0 represents the current design in iteration loop; $[x_j^L]$ and $[x_j^U]$ are the lower and upper bounds of x_j ; and CP represents the collapse prevention performance level.

In addition to using Taylor series and sensitivity analysis, Chan and Zou (2004) and Zou et al. (2005 a and 2005 b) proposed a notable OC method for RC moment frame structures. This method adopted the virtual work principle to explicitly express the inter-story drift as a function of the width and depth of all elements, and express the plastic hinge rotation as a function of tension and compression reinforcement ratios. The optimal PBSO problem, which minimizes the total material cost, is separated into two optimization phases. The objective of the first phase is to

minimize the total concrete cost of the RC frame that needs to satisfy the inter-story drift limit when the structures behaves elastically under minor earthquakes. In this phase, the section sizes of all elements are optimized based on the elastic analysis of the structure under the frequent earthquakes. Equation 1.59 shows the objective function.

$$\text{Minimize : } Z(B_i, D_i) = \sum_{i=1}^{N_i} w_i B_i D_i \quad \text{Equation 1.59}$$

where w_i is the unit cost of concrete; B_i and D_i are the width and the depth of the i^{th} member; N_i is the total number of elements.

To explicitly express the elastic inter-story drift by the optimal variables, virtual work principle is used, as shown in Equation 1.60.

$$u_j^{(n)} = \sum_{i=1}^{N_i} \int_0^{L_i} \left(\frac{F_X^{(n)} f_{Xj}}{EA_X} + \frac{F_Y^{(n)} f_{Yj}}{GA_Y} + \frac{F_Z^{(n)} f_{Zj}}{GA_Z} + \frac{M_X^{(n)} m_{Xj}}{GI_X} + \frac{M_Y^{(n)} m_{Yj}}{EI_Y} + \frac{M_Z^{(n)} m_{Zj}}{EI_Z} \right) dx \quad \text{Equation 1.60}$$

where $u_j^{(n)}$ is the virtual work on the j^{th} story on the n^{th} mode; L_i is the length of the i^{th} member; E and G are the Young's modulus and shear modulus of concrete; A_X , A_Y and A_Z are the cross sectional areas perpendicular to local axes X, Y and Z of the element; I_X , I_Y and I_Z are torsional and flexural moments of inertia along axes X, Y and Z of the element; $F_X^{(n)}$, $F_Y^{(n)}$, $F_Z^{(n)}$, $M_X^{(n)}$, $M_Y^{(n)}$ and $M_Z^{(n)}$ are the member internal forces and moments; f_{Xj} , f_{Yj} , f_{Zj} , m_{Xj} , m_{Yj} and m_{Zj} are the virtual member force and moment due to a unit virtual load applied to the building at the location corresponding to the displacement, u_j . The member internal forces and moments could be

obtained through structural analysis. Equation 1.60 can be formulated by B_i and D_i based on the three-dimensional elastic theory proposed by Cowper (1996). Therefore, the elastic displacement can eventually be explicitly expressed by the optimal variables, B_i and D_i .

The objective of the second optimization phase is to minimize the total reinforcement cost in the condition that the RC frame must satisfy the limits of inter-story drift and plastic hinge rotation under severe earthquakes. In this phase, the reinforcement ratio of each element is determined based on the nonlinear analysis of the structure subjected to severe earthquakes. Equation 1.61 shows the objective function.

$$\text{Minimize: } Z(\rho_i, \rho'_i) = \sum_{i=1}^{N_i} w_{si} (L_{si}\rho_i + L'_{si}\rho'_i) \quad \text{Equation 1.61}$$

where w_{si} is the unit cost of reinforcement; L_{si} and L'_{si} are the length of the tension and the compression reinforcement of the i^{th} member; and ρ_i and ρ'_i are the tension and compression reinforcement ratios.

Virtual work principle is adopted to explicitly express inter-story drift and plastic hinge rotation. The virtual work u_j on the j^{th} story derived from a pushover analysis is equal to the sum of virtual work produced by both the structural members, $u_{j,memb}$, and by the plastic hinges, $u_{j,hinge}$, as shown in Equation 1.62. Because the section sizes have been determined in the first phase, $u_{j,memb}$ shall be identical to $u_j^{(n)}$ in Equation 1.60. Additionally, based on Zou (2005), $u_{j,hinge}$ can be expressed by plastic hinge rotations, and the rotation of each element can be explicitly

formulated by the optimal variables (ρ and ρ'), as shown in Equations 1.63 and 1.64. Therefore, the nonlinear deformations can be explicitly expressed by ρ and ρ' .

$$u_j = u_{j,memb} + u_{j,hinge} \quad \text{Equation 1.62}$$

$$u_{j,hinge} = \sum_{i=1}^{N_j} \left[\sum_{h=1}^2 m_{pjh}^0 \theta_{ph} \right]_i \quad \text{Equation 1.63}$$

$$(\theta_p)_i = \left(\frac{M - M_y}{M_u - M_y} \theta_p^U \right)_i = \frac{\theta_p^U}{0.1} \left(\frac{M_i}{M_{yi}(\rho_i, \rho'_i)} - 1 \right) \quad \text{Equation 1.64}$$

where m_{pjh}^0 is the virtual moment at the h^{th} hinge of the i^{th} member on the j^{th} story; the subscript i represents the i^{th} element; θ_{ph} is the plastic rotation at the h^{th} plastic hinge of a member; θ_p^U is allowable plastic rotation; M is the applied moment at plastic hinge; M_y and M_u are the yield and ultimate moments corresponding to θ_p^U . M_y can be explicit expressed by ρ and ρ' .

In addition to the OC methods described above, Li et al. (2010) proposed a hybrid optimization method that combines the OC method proposed by Chan and Zou (2004) with genetic algorithm to optimally design RC tall buildings. Hajirasouliha et al. (2012) adopted Chan's method (2004) to determine section dimensions; however, the objective function is to minimize the reinforcement weight on each story and the structural damage caused by plastic hinging.

Note that, the optimal result by OC method may be only a local optimal solution (Huang et al., 2015). Moreover, the nonlinear deformation of a structure is affected by both strength and stiffness of the elements. For a RC moment frame, the element flexural stiffness is related to

section size, while the element flexural strength is related to both section size and reinforcement ratio. In addition, the permitted values of structural nonlinear response, such as allowable plastic hinge rotation determined in Table 1.2, are also a function of the optimal variables, such as section sizes and reinforcement ratio. Therefore, it is difficult for OC method to obtain the sensitivity coefficients of multiple variables. Moreover, Zou and Chan (2005) states that for a statistically indeterminate frame, the explicit constraints of structural responses derived from OC method are approximate due to the internal force redistribution when an optimal variable is changed. Therefore, in each iterative round, a complex nonlinear structural analysis is required to estimate the nonlinear structural response based on the updated variables.

1.6 Research Motivations

This research is motivated by the economic loss due to the conventional force-based seismic design and the lack of practical optimal PBSD method. Unexpected high economic loss due to the damage to structural and nonstructural components of buildings occurred during the recent earthquakes. This was partially caused by the conventional force-based method, which considers only the life safety performance level (Krawinkler, 1999; Ghobarah, 2001; Sung et al., 2009). PBSD has been a major focus of earthquake engineering community, because it can better limit the structural and nonstructural damage under multiple hazard levels (Powell 2008).

PBSD has been widely employed to evaluate the seismic performance of existing buildings, for which design details such as section size and reinforcement arrangement are

already known. However, the force-based design approach is still prevailing for designing new buildings because of the lack of general procedures of PBSB (Ghobarah, 2001). The current PBSB method is essentially a trial-and-error method with very high computational cost. Accordingly, it has been applied mainly to the critical facilities, such as hospital buildings.

The needs to simultaneously design numerous variables, including strength, stiffness and ductility of all components, and to consider multiple hazard levels call for developing optimal PBSB. As a result, some optimal PBSB methods described previously were proposed for RC frames; however, the existing methods have various drawbacks hindering their applications to the U.S. design practice.

- (1) Majority of the available optimal PBSB methods employed inter-story drift to measure structural performance, while only a few studies (Ganzerli et al., 2000; Zou and Chan, 2005 and Zou et al., 2007) considered the plastic hinge rotation of beams and columns. However, the plastic hinge rotation of a frame component better describes the local behavior of a RC frame and has been taken as the only performance measurement in the latest performance-based evaluation standard, ASCE 41-13 (2014).
- (2) As reflected in ASCE 41-13 (2014), the allowable plastic hinge rotation of a beam or a column is not a constant value; instead, it is a function of the shear stress or axial stress, which varies during lateral loading. This property was not considered in the existing studies (Ganzerli et al., 2000; Zou and Chan, 2005 and Zou et al., 2007), which assumed constant plastic hinge rotation capacity, and would significantly increase the complexity of the

optimization problem.

- (3) Majority existing optimal PBSDs requires complex algorithms and high computational cost due to the numerous variables. Therefore, a fully automated design process is needed to apply these methods. However, the needed computer programs are often not accessible for practicing engineers.

1.7 Research Objectives

The overall goal of this study is to develop a new optimal PBSD method for multi-story RC moment frames. The new method is expected to overcome the deficiencies of existing optimal PBSD methods and can be practically implemented by the U.S. design practice. Specific objectives include:

- Develop a simplified optimal PBSD procedure that incorporates the latest criteria of structural performance of RC frame buildings and can be practically implemented by design engineers;
- Investigate how much construction cost can be reduced by the proposed method, and how much the overall strength and stiffness of the optimal design are reduced from those of the conventional force-based seismic design;
- Examine whether the optimal design derived from the proposed method can satisfy the requirements of the selected performance levels under multiple hazard levels; and
- Investigate the influence of the overall strength and stiffness on the structure failure

probability and the statistically features of different types of nonlinear deformations.

1.8 Research Methodology and Tasks

Nonlinear pushover analysis is included in the proposed optimal PBSM to estimate the structural nonlinear deformation under multiple hazard levels. This structural analysis method permits incorporating various assumptions and simplifications and has low computational cost. Nonlinear programming is used to determine the optimal solution based on the linear objective function and the explicit feasible region boundary derived from the proposed method. Nonlinear dynamic analysis is used to estimate the deformation of the optimal structure, because this method can provide a more realistic structural response if the hysteretic behavior of structural components is properly defined (Deierlein et al., 2010). Latin Hypercube sampling method is adopted to perform the failure probability analysis, because this method can generate reliable statistical results with comparatively less sampling times.

This study follows the stages shown in Figure 1.14. In the first stage, a new optimal PBSM method is developed for multi-story RC moment frames. In the second stage, the proposed optimal PBSM method is applied to a prototype multi-story RC frame building to illustrate the detailed procedures and to investigate the effects of the proposed method on cost saving. The third stage examines the seismic performance the optimally designed structure by performing nonlinear dynamic analyses. The fourth stage investigates the influence of overall strength and stiffness on the structure failure probability by using Latin Hypercube sampling method.

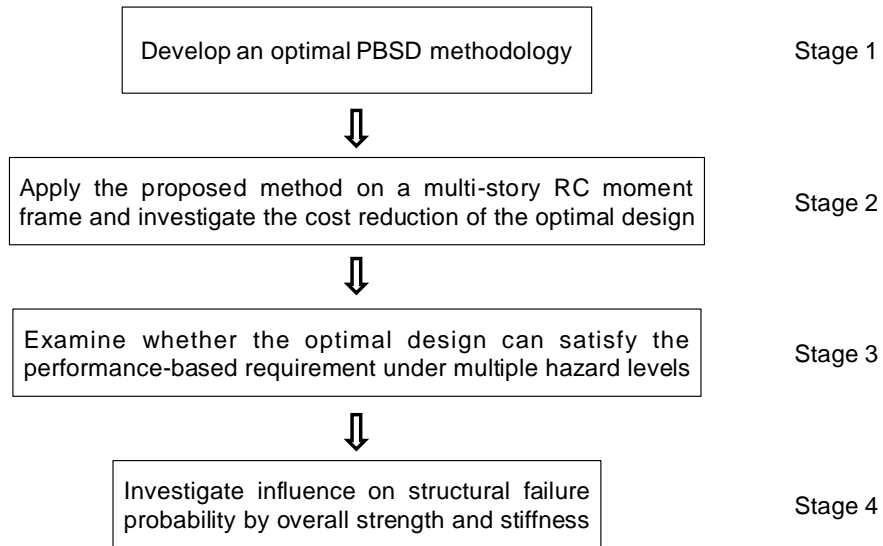


Figure 1.14 Research methodology and procedure of this study

CHAPTER 2

OPTIMAL PERFORMANCE-BASED SEISMIC DESIGN METHODOLOGY

2.1 Problem Statements

This study proposed a practical optimal PBSM method to achieve the minimum overall cost of a multistory RC moment frame, which satisfies the deformation requirements of multiple performance objectives. In addition, some other seismic design requirements to ensure a desired failure mode are incorporated to simplify the structural model and reduce the complexity of the optimization process.

Based on the capacity design philosophy, the expected failure mechanism of the RC moment frame is a flexural failure, which is a ductile failure mode with observable deflection and cracking before a dramatic loss of strength. However, the shear failure of RC structural components is brittle and has little or no warning before a sudden loss of strength. Therefore, the flexural strength of the elements in a RC moment frame is used as the design basis for force-controlled actions to make sure that they would not occur. Thus, the optimal methodology proposed in this study is used to optimize the flexural design. The design methods of the force-controlled behaviors, such as shear, still follow the procedures of the current seismic design. In addition, the optimized structure based on the proposed seismic design method shall also satisfy the gravity design requirements.

2.1.1 Objective function

The most widely selected single objective function minimizing total cost of RC moment frames is adopted in this study. The two types of construction material (concrete and reinforcement) are taken as the optimal variables. The unit costs of concrete and reinforcement are associated with volume and weight, respectively. Therefore, the objective function in this study of the RC moment frame is expressed by Equation 2.1.

$$\text{Minimize } C_T = c_c \Omega_c + c_s W_s \quad \text{Equation 2.1}$$

where C_T = the total cost; Ω_c = total concrete volume; W_s = total weight of reinforcements; c_c and c_s = unit costs for concrete and steel reinforcement. Normally, the unit cost of different material includes only the raw material cost without considering the labor cost, such as transportation, framework, erection, fabrication, and some other aspects. However, the labor cost occupies about 41% of the overall cost for RC structure (Rwamamara et al., 2010) Therefore, the unit cost in this study is composed by both raw material cost and labor cost.

2.1.2 Constraints

Because the purpose of optimal PBSO problem is to design a structure satisfying multiple performance objectives, the constraints shall include the structural behavior limits of multiple performance objectives. As described previously, the most widely adopted performance-based limits in PBSO are the nonlinear deformation requirements. Therefore, in this study, the design code specified nonlinear deformation requirements (inter-story drift ratio and plastic hinge

rotation) are adopted to define the performance constraints. Some other seismic design requirements, such as minimum positive moment at the ends of beams and strength column weak beam principle, are used to simplify the optimization or as the seismic design constraints.

2.1.2.1 Performance constraints

In this study, both inter-story drift ratio, γ , and plastic hinge rotation angle, θ , are employed to quantify the structural nonlinear behavior under multiple performance objectives. In different hazard levels, γ and θ are limited by different allowable values for preselected performance levels, as shown in Equation 2.2. The hazard levels include at least two of frequent, occasional, rare and very rare earthquakes, as shown in Figure 1.1.

$$\text{Subject to} \quad \forall \gamma_p \leq [\gamma]_p, \forall \theta_p \leq [\theta]_p \quad (p = 1, 2, \dots, P) \quad \text{Equation 2.2}$$

where $[\gamma]_p$ and $[\theta]_p$ are the allowable values for transient γ_p and θ_p in the p^{th} performance level. $[\gamma]$ is taken as the global deformation constraint to restrain the damage to nonstructural components, such as glass curtain walls, and avoid excessive P-delta effects. However, ASCE/SEI 41-13 (2014) has no specification on $[\gamma]$; thus, the allowable values of $[\gamma]$ for RC moment frames in the different performance levels are determined according to ASCE/SEI 41-06 (2007) shown in Table 1.1. On the other hand, $[\theta]$ is taken as the local deformation constraint to restrain the damage to structural elements (beams and columns). The allowable values of $[\theta]$ for RC moment beams and columns are determined according to ASCE/SEI 41-13 (2014) shown in Table 1.2.

2.1.2.2 Seismic design constraints

In addition to restraining the performance-based local and global deformations, other design requirements to ensure the desired seismic performance of RC frames are incorporated. These requirements, beneficial for reducing optimization complexity, are enforced from the original design. First, the beam-sway mechanism shown in Figure 2.1(a) is expected when the structure suffers from the rare and very rare earthquakes, and has large lateral nonlinear displacements. In this failure mechanism, plastic hinges appear at the ends of beams and the bottom ends of the first story columns. Earthquake energy is dissipated by the nonlinear deformation of these plastic hinges. Even though severe damage may occur to the beams, the structure will maintain its integrity. However, if the structure is designed inappropriately, the soft-story mechanism shown in Figure 2.1(b) may occur. In this failure mechanism, plastic hinges appear at both ends of the columns on the identical story; thus, the structure becomes an unstable geometrically changeable system, and may finally collapse.

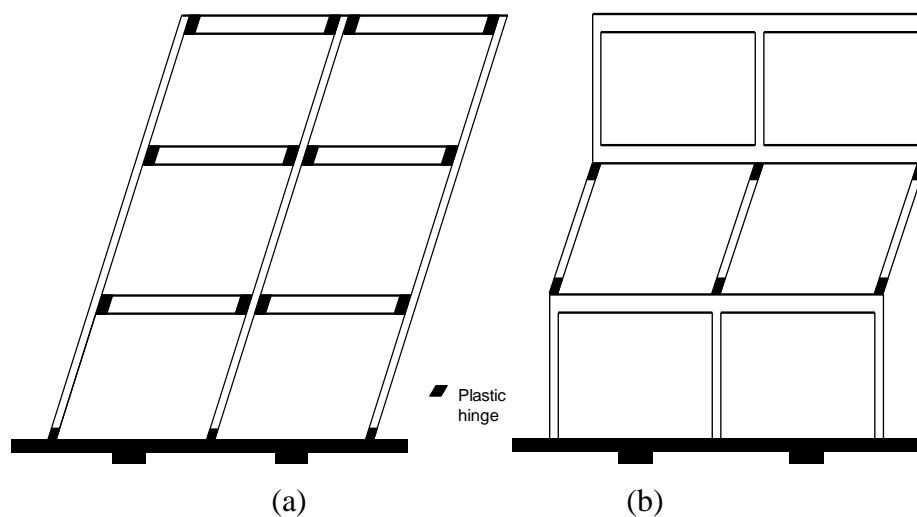


Figure 2.1 Structural failure types: (a) beam-sway mechanism; and (b) soft story mechanism

To avoid the soft-story mechanism, the needed flexural strength of a column is determined by the maximum bending moment demand this column may experience when the RC frame is loaded in the nonlinear pushover analysis due to rare or very rare earthquakes. Additionally, at a beam-column joint, to make sure that the plastic hinges appear at the ends of beams rather than in the columns, the flexural capacity of the columns shall be larger than that of the beams. This can be defined as strong column-weak beam behavior. For this purpose, the method suggested in ACI 318-14 (2014) to determine the flexural strength of columns at a beam-column joint is adopted in this study, as shown in Equation 2.3.

$$\sum M_{nc} \geq 1.2 \sum M_{nb} \quad \text{Equation 2.3}$$

where M_{nc} and M_{nb} are the flexural strength of columns and beams framing into a joint, respectively.

Second, yielding in the first-floor columns is permitted at their bottom ends. However, prior to the exhaustion of column plastic deformation capacity, the sufficient number of beams shall have been engaged in developing yielding. The more beam plastic hinges appear, the more earthquake energy is dissipated and thus less damage will be induced to the columns. In addition, when a structure suffers the lateral loads caused by earthquakes, the axial force of columns will increase dramatically. As indicated in Table 1.2, if a column carries a large axial force, its plastic hinge rotation capacity $[\theta]$ is less than that of a beam. Moreover, reduced column size due to optimization leads to decreased $[\theta]$. Therefore, in this study, the flexural strength at the bottom

ends of the first story columns is increased. Following the yielding in the first-floor beams, the inflection point of a first-floor column moves up and is assumed to be located approximately at 3/4 of column height, as shown in Figure 2.2. The needed flexural strength of a column at the support, $M_{nc,2}$, is then taken as $1.5\sum M_{nb}$.

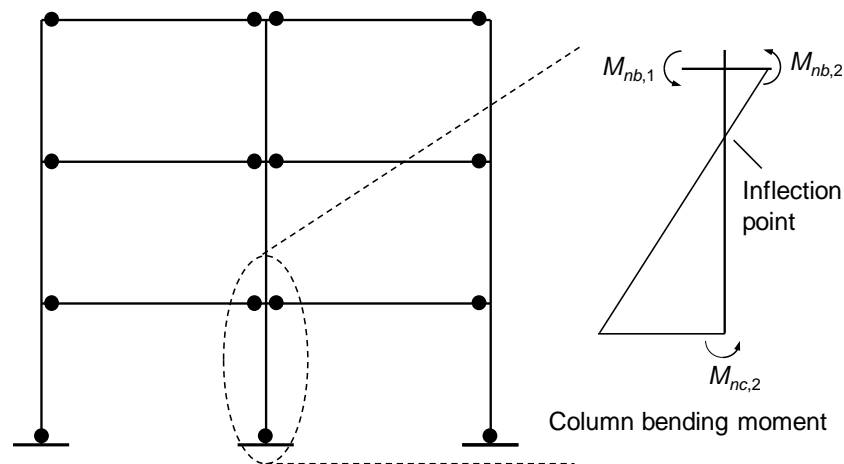


Figure 2.2 Beam-sway mechanism and column flexural strength in the first floor

Third, the code-specified maximum and minimum reinforcement ratios of a section need to be satisfied. If the reinforcement ratio is higher than the maximum allowable value, the concrete in compression will fail before the yielding of the tension reinforcement, and an abrupt failure will occur due to the continuous failure of concrete in compression. The maximum reinforcement ratio limit ensure sufficient rotation capacity of plastic hinges (Subramanian, 2010). When the reinforcement ratio is lower than the minimum allowable value, an abrupt failure will occur without warning due to the suddenly increased deformation (McCormac and Brown, 2015). Therefore, the requirements on ACI 318-14 (2014) about the maximum and

minimum reinforcement ratios of a section is adopted in this study.

Fourth, based on ACI 318-14 (2014), the positive moment strength of a beam at plastic hinge regions shall be at least half of the negative moment resistance. Therefore, to reduce the number of the optimal variables, the positive moment strength of a beam can be assumed as half of the negative moment resistance. Furthermore, other code-specified requirements for the reinforcement shall be satisfied. For example, ACI 318-14 (2014) requires that both negative and positive moment strength at any section along the beams shall be at least one-fourth the maximum moment strength provided at the face of either joint. Moreover, Beam short- and long-term deflections, shear strength at the beam-column joints, and the shear strength of the beams and columns should also be satisfied.

2.2 Optimization Methodology

2.2.1 Overview

Figure. 2.3 outlines the optimization procedure developed in this study. In Figure 2.3(a), the optimal solution is obtained by a nonlinear programming method in this study. The nonlinear programming problem has a linear objective function and a convex feasible region. The objective function and constraints in Equations 2.1 and 2.2 incorporates the three major characteristics of an inelastic system resisting seismic loads (i.e., strength, stiffness and ductility) because Ω_c affects elastic stiffness, W_s is associated with member flexural strength, and γ and θ are related to ductility. The constraints related to acceptable structural performance define a feasible region for

the two decision variables Ω_c and W_s . Because the objective function is linear with respect to Ω_c and W_s , the optimal solution (Point A in Figure. 2.3(a)) must be located on the feasible region boundary and is reached when the objective function becomes tangent to the feasible region.

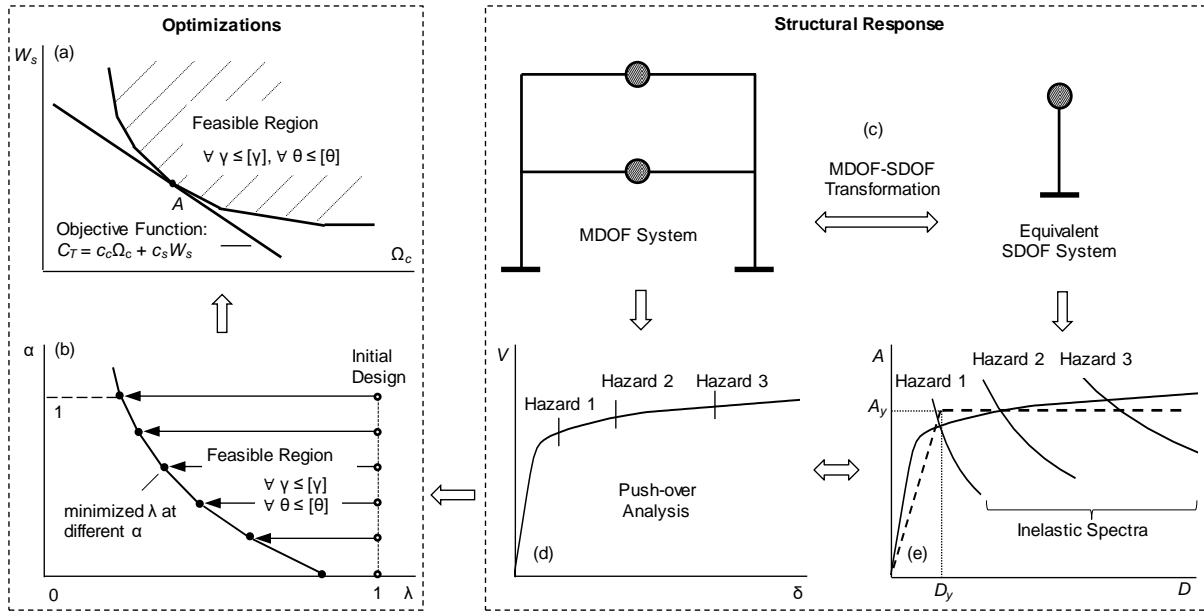


Figure 2.3 Framework of optimization: (a) optimization in material consumption domain; (b) stiffness optimization for system with different strengths; (c) MDOF-SDOF transformation; (d) nonlinear static analysis and determination of roof displacement demands; and (e) N2 method using inelastic spectra

Despite the simple format of the objective function, several challenges in obtaining the optimal solution exist. The first challenge is the determination of peak deformation demand caused by the different levels of seismic hazard. This study intends formulate the peak deformation demand of a nonlinear RC frame system as a function of its lateral stiffness and strength. This, however, cannot be achieved by nonlinear time-history analyses. Accordingly,

capacity spectrum method, which employs nonlinear static analysis, is adopted to predict the peak seismic response. The details of applying this method are given later in Section 1.2, and schematically is shown in Figure 2.3(c).

The second challenge is that the peak nonlinear deformation demand of a RC frame is affected by not only stiffness but also flexural strength of the beams and columns because the commonly assumed equal displacement rule may not be applicable. As indicated by Krawinkler and Seneviratna (1998), the peak lateral displacement of an elastic-perfectly plastic SDOF system due to ground excitation differs from that of a purely elastic system. The difference is a function of the fundamental period T , the strength reduction factor R , and the ductility ratio μ . These properties are correlated through a R - μ - T relationship (Miranda and Bertero, 1994 and Vidic et al., 1994). It follows that the optimal member size, which controls system elastic stiffness, cannot be solely determined from a target lateral displacement without considering the flexural design of members. Accordingly, different from most of the past studies (Zou and Chan, 2005; Xu et al., 2006; Grierson et al., 2006; Li et al. 2010 and Zou et al., 2007) that utilized nonlinear static analysis, Ω_c and W_s are not separately optimized in this study.

The third challenge in obtaining an optimal solution is defining the feasible region boundary. As indicated in Equations 2.1 and 2.2, the objective function is expressed by material consumptions Ω_c and W_s , whereas the constraints are defined using plastic hinge rotation θ and optionally by inter-story drift ratio γ . These two sets of variables are correlated by structural performance predicted by structural analysis. To solve Equations 2.1 and 2.2, either the feasible

region boundary is defined by Ω_c and W_s or the objective function is transformed as a function of θ and γ . The former approach is considered. However, the deformation demands in terms of γ and θ for a multistory RC frame are difficult to be explicitly formulated as a function of Ω_c and W_s . Moreover, as indicated in Tables 1.1, the plastic rotation capacity $[\theta]$ of a member is a function of shear or axial force, which varies during lateral loading, implying that $[\theta]$ cannot be predefined. The coupling effect between plastic hinge rotation capacity and seismic demand complicates the development of an optimization algorithm and was not considered in the past studies, which assumed a fixed value of $[\theta]$. A two-stage optimization approach is considered herein to address these issues. In the first stage, strength-based design procedure is followed to obtain an original design for the RC frame. Optimization, as shown in Figure. 2.3(b), is then performed to determine a feasible region boundary defined by discretized pairs of a stiffness parameter λ and a flexural strength parameter α normalized based on the original design. In the second stage, the feasible region boundary determined previously in the λ - α domain is converted into that in the Ω_c - W_s domain, from which the optimization problem defined by Equations 2.1 and 2.2 is solved by a nonlinear programming method.

2.2.2 Simplifications

The optimal design of a structural system is ultimately represented by the stiffness and strength properties of each component. For convenience of formulation, two dimensionless design variables, a relative flexural stiffness factor denoted as λ and a relative flexural strength factor denoted as α , are defined for each member. The relative stiffness factor λ is defined as the

ratio of section moment of inertia varying during optimization to that determined from the original design. The relative strength factor α is defined as

$$\alpha = \frac{M_n - M_G}{M_{n,0} - M_G} \quad \text{Equation 2.4}$$

where M_n is member flexural strength varying during optimization, $M_{n,0}$ is the flexural strength determined from the original design, and M_G is the bending moment caused only by the gravity loads considered in the seismic design.

λ is optimized for each α using the algorithm described in Section 2.2.3.4. The feasible region boundary in the λ - α domain shown in Figure 2.3(b) is determined by connecting the points with discrete α values and the corresponding minimum λ value. $\lambda = 1$ and $\alpha = 1$ correspond to the sectional stiffness and strength from the original design, respectively. The parameter λ correlates concrete volume Ω_c ; the parameter α can be translated into the consumption of flexural reinforcement W_s when the value of Ω_c is determined and indicates the degree of reducing member flexural strength from that determined from the original design. A RC frame shall also be designed based on the load combinations purely for gravity loading. A relative strength factor α_G corresponding to gravity design is defined accordingly and taken as the lower bound of α . α_G is evaluated using Equation 2.4 by replacing M_n with $M_{G,0}$, the bending moment demand caused by gravity design.

Because many beams and columns exist in a RC frame, the total number of design

variables for the entire system far exceeds the two optimal variables Ω_c and W_s in Equation 2.1. To limit the computational cost associated with optimization and enable expressing the feasible region eventually using the two optimal variables, this study intends to reduce the number of variables to two as well. For this purpose, it is required that both the ratio of cross-sectional dimension and the ratio of flexural strength among different members determined from the original design be maintained during the process searching the minimum λ . In other words, the relative stiffness factor λ and the relative strength factor α are identical for all the elements at any step of optimization; thus these two factors can be used as the overall indices measuring stiffness and strength of the entire structure.

With such a simplification, the additional design requirements described previously, regarding strong-column/weak-beam and positive flexural strength of a beam section, are not necessary to be considered as optimization constraints, because they are automatically satisfied once they have been enforced in the original design. Due to the above simplifications, the design result based on the proposed approach would not be a global optimal solution mathematically. However, in a seismic design of RC frame, the member sizes are typically the same in every two to three stories. Moreover, the beam flexural reinforcement is normally identical on each side of a beam-column joint. All these features can be incorporated in the original design. Thus, even if the factors α and λ are used to uniformly modify the original design for simplification purpose, the optimal design result would be close to a global optimal solution that can reflect design practice.

2.2.3 Determination of feasible region boundary

2.2.3.1 Overview

The key to solving Equations 2.1 and 2.2 is the determination of the feasible region boundary, which is obtained first in the λ - α domain. A point situated on the feasible region boundary shown in Figure 2.3(b) can be interpreted as either the minimum λ satisfying performance criteria at a given α or the minimum α at a given λ . The former definition is considered to formulate an iterative procedure used to determine the feasible region boundary. A set of discrete α values ranging from α_G to 1 are selected. For each α , the flexural strength of a member, M_n , is modified from the original design based on Equation 2.4. For the RC frame with a specific value of α , λ is minimized for each level of earthquake hazard using a procedure described in Section 2.2.3.4; the controlling value of λ gives the optimal λ for this α . This procedure is repeated for all selected α values so that a piecewise linear feasible region boundary is defined in the λ - α domain.

The height and effective depth of a beam are denoted in the following discussions as h and d , respectively. Their values from the original design are designated as h_0 and d_0 . When minimizing λ at a given value of the relative strength factor α , the cross-sectional area of frame members is reduced. Accordingly, in addition to limiting plastic hinge rotation and inter-story drift ratio, the maximum reinforcement ratio permitted by design codes, ρ_{max} , needs to be considered as a constraint. The flexural capacity of a beam can be expressed as

$$M_n = \omega b d^2 f'_c (1 - 0.59\omega) \quad \text{Equation 2.5}$$

where f'_c is concrete compressive strength; b is beam width; and ω is a tensile reinforcement index calculated as $\omega = \rho f_y / f'_c$ with f_y being the yield strength of reinforcement. Approximating d/d_0 as h/h_0 , the minimum λ corresponding to ρ_{max} can be derived as

$$\lambda_{min,1} = \left(\left(\alpha + \frac{M_G}{M_{n,0} - M_G} \right) \left(\frac{M_{n,0} - M_G}{M_{n,0}} \right) \left(\frac{\omega_0}{\omega_{max}} \right) \left(\frac{1 - 0.59\omega_0}{1 - 0.59\omega_{max}} \right) \right)^{\frac{4}{3}} \quad \text{Equation 2.6}$$

where ω_0 and ω_{max} are beam tensile reinforcement index according the original design and ρ_{max} , respectively. The flexural stiffness of a beam also needs to satisfy the deflection serviceability requirement under gravity loading. Denoting the minimum relative stiffness needed for this purpose as $\lambda_{min,2}$, the lower bound of λ is then defined as $[\lambda] = \max\{\lambda_{min,1}, \lambda_{min,2}\}$.

The first-stage optimization that minimizes the relative stiffness factor λ at a given relative strength factor α can then be stated as Equation 2.7. Section 2.2.3.4 presents the detailed algorithm for solving this optimization problem. Because the flexural strength of a column interacts with its axial force, which varies during lateral loading, $[\lambda]$ corresponding to ρ_{max} for columns cannot be predefined and needs to be checked during optimization. However, the optimal design for λ should not be affected by ρ_{max} for the columns due to its high permitted value up to 8% in a design code ACI 318-14 (2014). Once the optimal result of λ becomes available, the section size of each frame member and thus the total volume of concrete Ω_c can be determined based on those of the original design and the definition of λ . The optimization

problem Equation 2.7 is implemented to all selected values of α ($\alpha_G \leq \alpha \leq 1$) for each level of seismic hazard. The data sets of α and its minimum λ constitute the feasible region boundary in the λ - α domain.

$$\begin{aligned}
 & \text{Minimize } \lambda \\
 & \text{Subject to } \forall \theta \leq [\theta] \\
 & \quad \quad \quad \forall \theta \leq [\theta] \text{ (Optimal)} \\
 & \quad \quad \quad \lambda \geq [\lambda]
 \end{aligned}
 \tag{Equation 2.7}$$

Each pair of α and its minimum λ provides information regarding the needed flexural strength and section size, from which flexural designs are conducted for all the beams and columns. The flexural design may be governed by the minimum reinforcement ratio specified in design codes; however, this occurs normally at very few locations. Based on the flexural design of each component, the total weight of reinforcing steel W_s is evaluated. Note each pair of α and its minimum λ corresponds to a unique pair of W_s and Ω_c ; hence, the feasible region boundary in the λ - α domain is transformed into that in the W_s - Ω_c domain, where the second stage of optimization defined by Equations 2.1 and 2.2 can be carried out.

2.2.3.2 Load-deformation response due to modified flexural stiffness

To solve Equation 2.7 at each selected α ($\alpha_G \leq \alpha \leq 1$), the peak seismic response of RC frame in terms of plastic hinge rotation θ and inter-story drift γ need to be determined for each level of seismic hazard. This is achieved by using capacity spectrum method described in Section 1.2 and summarized in Figures 2.3(c) to 2.3(e). For the RC frame with a specific value of α but

without stiffness modification from the original design (i.e., $\lambda = 1$), nonlinear static analysis is conducted. The analysis provides information regarding base shear, roof displacement, inter-story drift ratio, and plastic hinge rotation. For the structural analysis in this study, concentrated plasticity model is adopted. This mode simulates the beams and column by line elements having concentrated plasticity at ends (plastic hinges). The sections outside the plastic hinge regions are linear elastic with a flexural stiffness taking into account the effects of concrete cracking. Following gravity loading, lateral loads corresponding to the first vibration mode are applied. However, if the variation of inertia force distribution due to inelastic response is considered, an adaptive lateral load pattern (Krawinkler and Seneviratna, 1998; Kalkan and Kunnath, 2007) accounting for the effects of higher modes and member yielding can be used to more accurately capture the structural response by means of nonlinear static analyses. The lateral loading response of the structure with $\lambda = 1$ evaluated by a nonlinear static analysis consists of the generation of a series of plastic hinges. Due to the use of the concentrated plasticity model, even if the occurrence of each plastic hinging modifies the system stiffness matrix, it remains identical between two subsequent hinging. Lateral loading causing the j^{th} plastic hinge is taken as loading step j and designated by a subscript within parenthesis in the following discussions. Denoting the system stiffness matrix during loading step j as $\mathbf{K}_{(j)}$, the increase in the displacement of the system $\Delta \mathbf{u}_{(j)}$ and story drift and the increase in lateral load $\Delta \mathbf{F}_{(j)}$ satisfies $\Delta \mathbf{F}_{(j)} = \mathbf{K}_{(j)} \Delta \mathbf{u}_{(j)}$. Thus, the total displacement $\mathbf{u}_{(j)}$ at the completion of the j^{th} loading step under load

$\mathbf{F}_{(j)}$ is

$$\mathbf{u}_{(j)} = \sum_{k=1}^j \mathbf{K}_{(k)}^{-1} \Delta \mathbf{F}_{(k)} \quad \text{Equation 2.8}$$

When the relative strength factor α is fixed and the relative stiffness factor λ is applied uniformly to all frame members to modify their flexural stiffness, the sequence of plastic hinging remains unchanged. Accordingly, the stiffness matrix of the modified system during the j^{th} loading step can be expressed as $\mathbf{K}_{(j)}^{\lambda} = \lambda \mathbf{K}_{(j)}$. In addition, when the value of α is fixed, modifying λ has not impact on the load increase $\Delta \mathbf{F}_{(j)}^{\lambda}$ needed to generate a new plastic hinge in the modified system, that is, $\Delta \mathbf{F}_{(j)}^{\lambda} = \Delta \mathbf{F}_{(j)}$. Thus, the lateral displacement of the system with modified stiffness can be derived as

$$\mathbf{u}_{(j)}^{\lambda} = \sum_{k=1}^j [\mathbf{K}_{(k)}^{\lambda}]^{-1} \Delta \mathbf{F}_{(k)}^{\lambda} = \frac{1}{\lambda} \mathbf{u}_{(j)} \quad \text{Equation 2.9}$$

Accordingly, under the same lateral load $\mathbf{F}_{(j)}$ before causing a collapse mechanism, the roof displacement δ , inter-story drift ratio γ , and plastic hinge rotation angle θ of the system modified by λ must satisfy

$$\frac{\delta}{\delta_0} = \frac{\gamma}{\gamma_0} = \frac{\theta}{\theta_0} = \frac{1}{\lambda} \quad \text{Equation 2.10}$$

where δ_0 , γ_0 , and θ_0 are the roof displacement, the inter-story drift ratio, and the plastic rotation angle of the structure without stiffness modification (i.e., $\lambda = 1$). Equation 2.10 is of

significant convenience for solving the first-stage optimization problem defined in Equation 2.7. As shown in Figure 2.4, once the base shear vs. roof displacement ($V-\delta$) response of a frame system at a given value of α but without stiffness reduction ($\lambda = 1$) becomes available, it can be used to directly construct a nonlinear $V-\delta$ response for the system with modified flexural stiffness. Accordingly, there is no need to perform extra structural analyses during the process of searching for the minimum λ for the structure at the selected α . Thus, the total number of pushover analyses needed to complete the proposed optimal seismic design is identical to the number of discretized α values ($\alpha_G \leq \alpha \leq 1$) chosen to define a feasible region boundary.

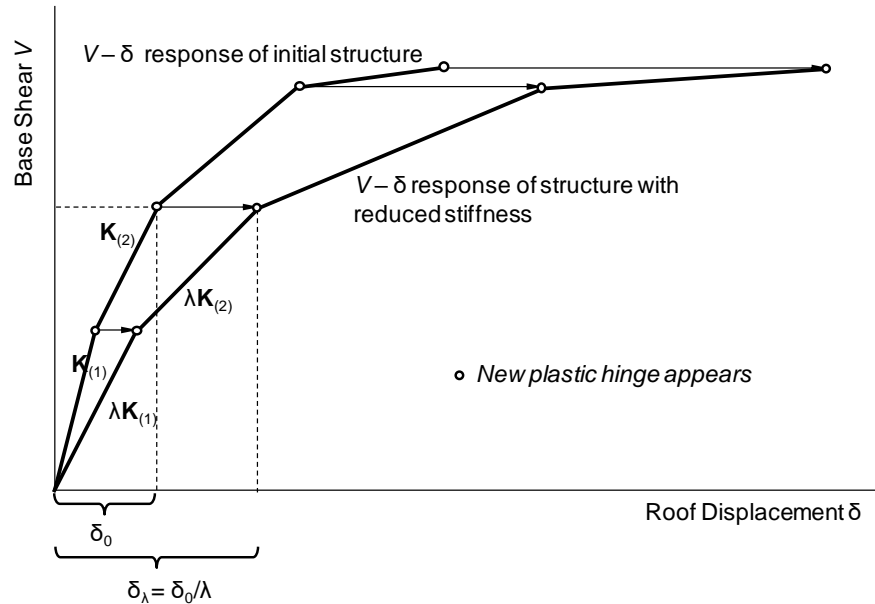


Figure 2.4 Constructing based shear vs. roof displacement response based on nonlinear static analysis result of the structure without stiffness modification ($\lambda = 1$)

2.2.3.3 Determination of minimum stiffness at given flexural strength

For each relative strength factor α ($\alpha_G \leq \alpha \leq 1$), the application of capacity spectrum

method described in Section 1.2 estimates the peak deformation demands. If the limiting values ($[\theta]$ and $[\gamma]$) are not exceeded under any seismic hazard, the relative stiffness factor λ is optimized by reducing member section size until one of the constraints in Equation 2.7 controls. When the section size decreases, reinforcement ratio increases, because the flexural strength of any element is unchanged. The beam shear stress tends to increase due to reduced section size. Therefore, the increase of both reinforcement ratio and shear stress result in decreased beam plastic hinge rotation capacity $[\theta]$, as indicated in Table 1.2. Because of the interaction between λ and $[\theta]$, an iterative approach is employed to search for the minimum λ .

A superscript is used for the variables to denote iteration step. The iterations, schematically illustrated in Figure 2.5, start from $\lambda^{(0)} = 1$. The capacity spectrum method is applied to evaluate effective period $T^{(0)}$ and peak displacement $D_{max}^{(0)}$ of the equivalent SDOF system as well as story drift ratio $\gamma^{(0)}$ and plastic rotation angle $\theta^{(0)}$ at the peak roof displacement $\delta_{max}^{(0)}$ of the MDOF system. As stated previously and shown in Figure 2.4, at the same value of α , the based shear vs. roof displacement ($V-\delta$) response for different values of λ can be determined directly from that of the structure without stiffness modification ($\lambda = 1$). It follows that the idealized bilinear capacity curve for $\lambda^{(0)} = 1$ can be used to construct new bilinear capacity curves for $\lambda^{(i)} < 1$ ($i \geq 1$) in the subsequent iterations. Because member flexural strengths are not changed, the yield acceleration A_y for the capacity curves associated with different λ values can be approximated to be identical, as shown in Figure 2.5.

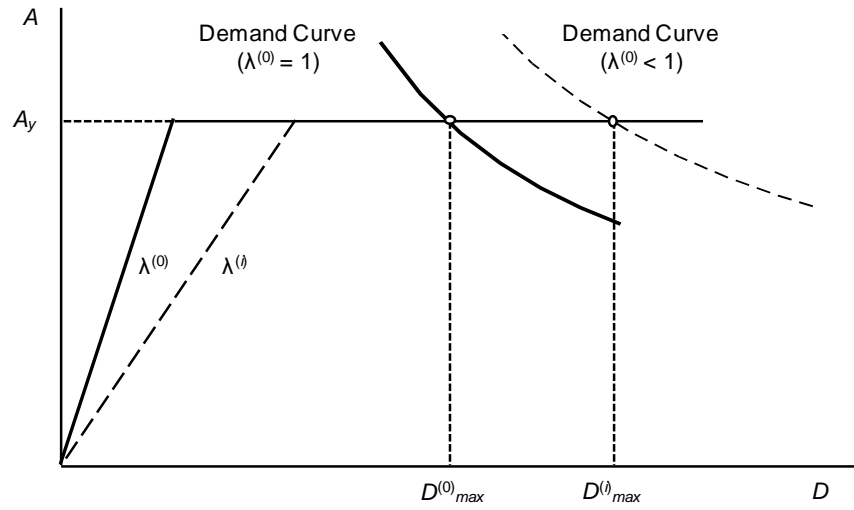


Figure 2.5 Effects of modifying relative stiffness factor λ on capacity and demand curves

Between two subsequent plastic hinging in the structure under increasing lateral deformation, the inter-story drift ratio γ and plastic hinge rotation θ at different locations increase linearly but at different rates. If neither θ nor γ reaches the allowable value during the previous iteration step $i-1$, a parameter $\eta^{(i)}$, defined in Equation 2.11 based on the deformation properties given in Equation 2.10, is considered to determine the relative stiffness factor $\lambda^{(i)}$ for the next iteration step i . The term related to γ in Equation 2.11 shall be removed if only plastic rotation θ is used to define optimization constraints in Equation 2.2. The parameter $\eta^{(i)}$ is used to control the iteration speed and determine when the iteration stops. If the absolute value of $|\eta^{(i)} - 1|$ is less than a value v^* , then either γ or θ becomes sufficiently close to its limit; thus the iteration stops and the minimum λ is obtained. The lower bound stiffness parameter $[\lambda]$ also needs to be considered. $\lambda^{(i)}$ defined by Equation 2.12 is used in step i to uniformly reduce the section stiffness of the frame members.

$$\eta^{(i)} = \text{Min} \left\{ \nabla \frac{[\theta]^{(i-1)}}{\theta^{(i-1)}} \cup \nabla \frac{[\gamma]}{\gamma^{(i-1)}} \right\} \quad \text{Equation 2.11}$$

$$\lambda^{(i)} = \frac{\lambda^{(i-1)}}{\eta^{(i)}} = \frac{1}{\prod_{m=1}^i \eta^{(m)}} \geq [\lambda] \quad \text{Equation 2.12}$$

Once $\lambda^{(i)}$ is determined, a new bilinear capacity curve in the equivalent SDOF system is created. Because $\lambda^{(i)}$ uniformly modifies member flexural stiffness in the MDOF system, it can be approximated that $\lambda^{(i)}$ equally affects the lateral stiffness of the equivalent SDOF system. Its effective period is then determined as $T^{(i)} = T^{(0)}/(\lambda^{(i)})^{0.5}$, because the equivalent mass is predominated by the mass of slab and can be assumed as unchanged. As shown in Figure 2.5, due to decreased system stiffness, the demand curve shifts to the right side, resulting in an increased spectral displacement. Equation 2.13 can be derived from Equation 2.10 and used to determine the spectral displacement $D_{max}^{(i)}$, story drift $\gamma^{(i)}$, and plastic hinge rotation $\theta^{(i)}$ of the modified structure in iteration step i .

$$\frac{D_{max}^{(i)}}{D_{max}^{(0)}} = \frac{\gamma^{(i)}}{\gamma^{(0)}} = \frac{\theta^{(i)}}{\theta^{(0)}} = \frac{1}{\lambda^{(i)}} \left(\frac{\mu^{(i)}}{\mu^{(0)}} \right) \quad \text{Equation 2.13}$$

where $\mu^{(i)}$ is determined from the R - μ - T relationship. The strength reduction factor $R^{(i)}$ needed to apply the R - μ - T relationship at step i is

$$R^{(i)} = \frac{S_{ae}^{(i)}}{A_y} \quad \text{Equation 2.14}$$

where $S_{ae}^{(i)}$ is the elastic spectral acceleration for the structure having an effective period of $T^{(i)}$.

Iterations with different values of λ are performed until one of the optimization variables in Equation 2.7 reaches a limit. Reducing λ increases both γ and θ ; meanwhile, $[\gamma]$ is unchanged and $[\theta]$ is reduced due to the increased reinforcement ratio and increased shear stress. Accordingly, the peak deformation demands in terms of γ and θ gradually approach the limiting values after each iteration step and a converged result can be obtained.

The minimum relative stiffness factor λ shall be the maximum one among all the relative stiffness factors derived from different selected performance objectives. The feasible region boundary in λ - α domain can be derived by repeating the process of searching minimum λ for different discretized α values. Then the points on this boundary in the λ - α domain is transform to those in the Ω_c - W_s domain. Based on λ and the section sizes of the beams and columns of the structure without stiffness modification ($\lambda = 1$), the element flexural stiffness and section sizes of the structure modified by λ can be obtained. The total concrete volume Ω_c can be derived accordingly. Because the relative strength factor α is unchanged, the flexural strength of the beams and columns of the structure without stiffness modification can be used to calculate the needed reinforcement areas of the elements for the modified structure based on the determined section sizes. The total reinforcement weight W_s can be accordingly derived.

2.3 Optimal Design Procedures

The procedure of the proposed optimal PBSO approach is summarized as follows:

Step 1: A force-based seismic design satisfying the requirements given in Section 2.1.2.2 is conducted to determine the needed flexural strengths of all members. The initial design results ($\lambda = 1$ and $\alpha = 1$) are subjected to optimization.

Step 2: A series of relative strength factors ($\alpha_G \leq \alpha < 1$) are selected. For each α , the member flexural strengths in the initial design are uniformly reduced and Steps 3 and 4 are implemented. The ratio of section dimension and the ratio of flexural strength among different members are maintained throughout optimization.

Step 3: For a specific α , the relative stiffness factor is set as $\lambda = 1$ and a nonlinear static analysis is conducted. The considered seismic hazards are defined using elastic spectral accelerations. Capacity spectrum method is then applied to determine the peak seismic deformation demands at different seismic hazards for the structure with $\lambda = 1$.

Step 4: For the structure with the α value considered in Step 3, the relative stiffness factor λ is optimized by solving Equation 2.7 using the numerical approach presented in Section 2.2.3.3.

Step 5: Based on the pairs of α and optimized λ determined from the previous steps, a feasible region is defined in the λ - α domain. For each pair of α and optimized λ , section flexural design is conducted and the total material consumptions Ω_c and W_s are evaluated. The feasible region in the λ - α domain is then accordingly converted into that in the Ω_c - W_s domain.

Step 6: The Ω_c and W_s that minimize total cost are determined by solving Equations 2.1 and 2.2. The values of λ and α corresponding the optimal Ω_c and W_s provide information regarding the optimal section size and flexural reinforcement design of each member. Finally, the design code requirement for minimum flexural reinforcement ratio is implemented..

Figure 2.6 shows the flow of the optimal PBSO method proposed in this study corresponding to the steps above.

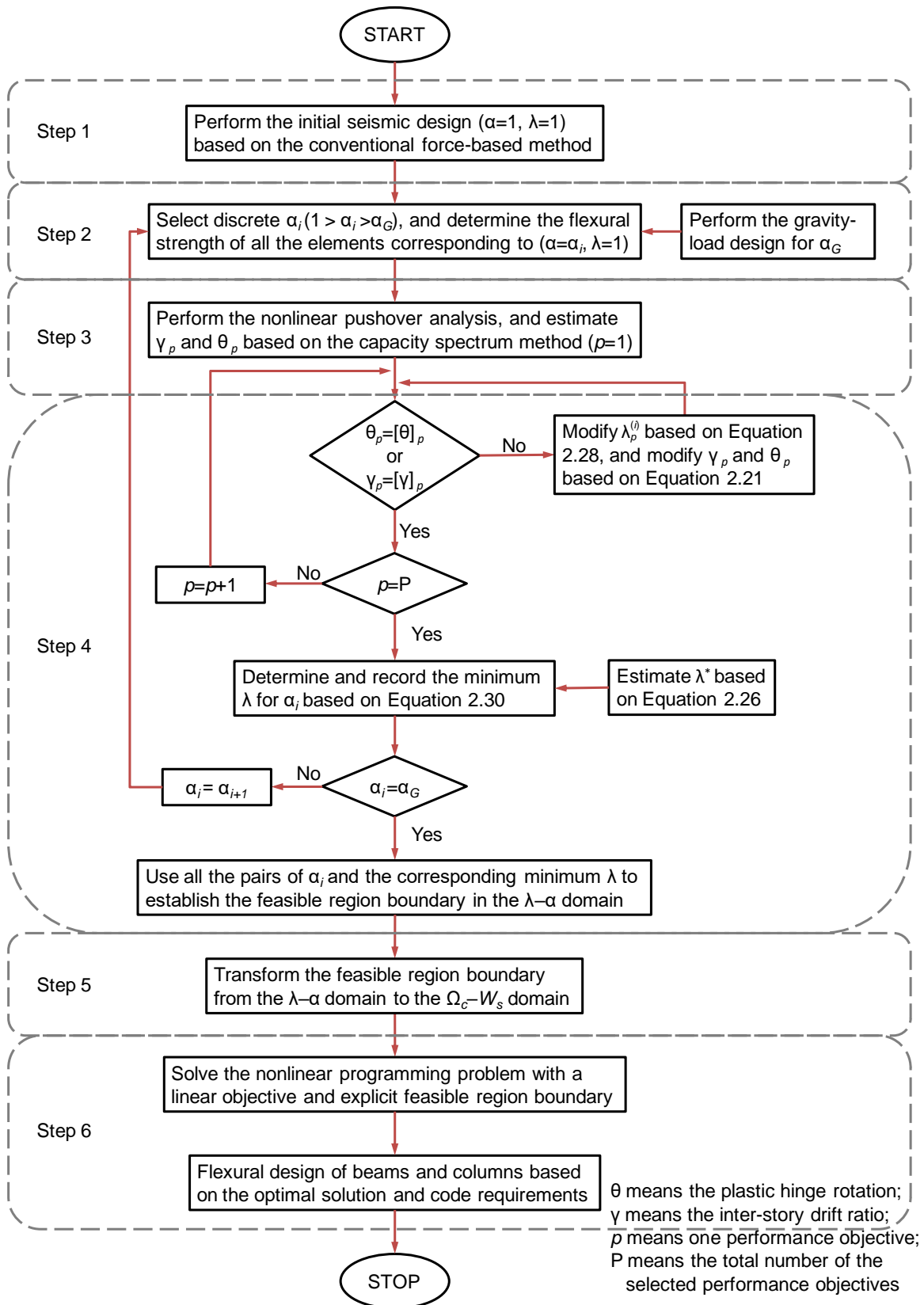


Figure 2.6 Flow of the optimal PBS method proposed in this study

2.4 Extension of the Proposed Optimal PBSD Method

To increase accuracy, computational efficiency, and applicability, some extensions can be incorporated into the proposed optimal PBSD method. First, the number of the discretized α between α_G and 1 affects the computational cost of the proposed method and the accuracy of the optimal result. When this number increases, the computational cost would increase; when this number decreases, the accuracy of the optimal result would decrease. To solve this conflict, the proposed method can be first applied with large interval between two successive α (Figure 2.7(a)) to obtain the range (between point A and B) of the probable optimal design (point C). Then the proposed method is applied with small interval around this range (Figure 2.7(b)), to achieve a more accurate optimal result based on part of the feasible region boundary with small intervals.

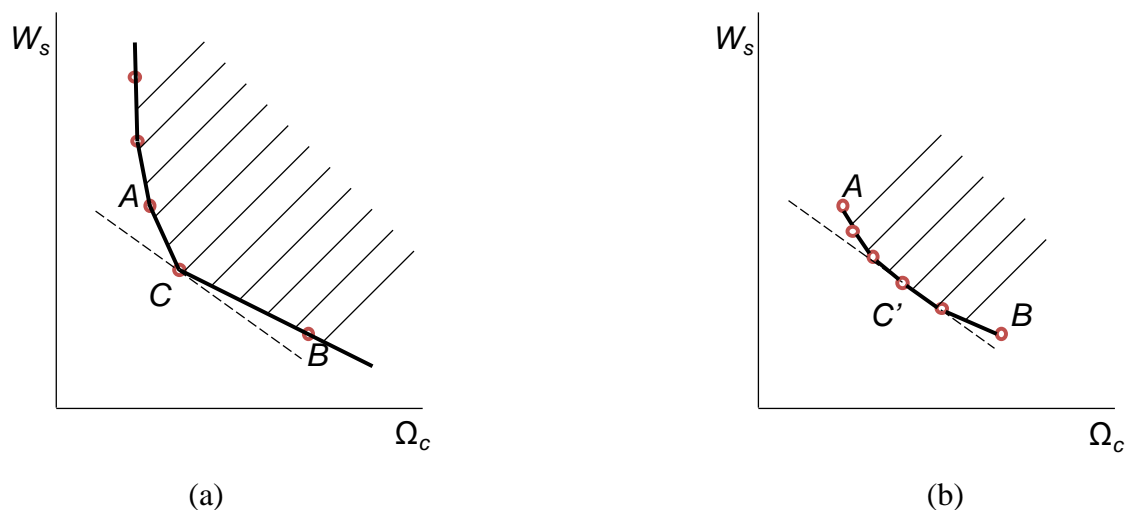


Figure 2.7 Illustration of the two times of optimal PBSD methods with (a) large interval; and (b) small interval

Second, the accuracy of the nonlinear pushover analysis depends on the lateral load

pattern, which simulates the total inertial forces of each story caused by ground acceleration. However, the inertial force distribution pattern along the height of the structure keeps changing after the member yielding (Krawinkler and Seneviratna, 1998; Kalkan and Kunnath, 2007), and the effect of higher modes increases accordingly. Therefore, an adaptive lateral load pattern can be used by assuming the lateral load pattern is proportional to either the story drift pattern of the structure (Fajfar and Fischinger, 1988) or to the story shear pattern (Bracci et al. 1997).

2.5 Uniqueness of Proposed Optimal PBSM Method

To compare the optimal strategies of the proposed method with the two-step method proposed by Zou and Chan (2005), the searching paths of these methods are demonstrated on the coordinate system defined by total concrete volume Ω_c and total reinforcement weight W_s , shown in Figure 2.8. Figure 2.8(a) illustrates the searching paths of the two-step OC or hybrid OC–metaheuristics optimal methods, such as the work by Zou and Chan (2005), Hajirasouliha et al. (2012), and Li et al. (2010). These methods first optimize the concrete consumption based on the performance constraints for occasional earthquake by reducing Ω_c , then optimize the reinforcement consumption by reducing W_s based on constraints for rare and very rare earthquakes. The computational cost of this strategy is reduced compared with the first one; however, this method essentially assumes that (1) no nonlinear deformation appears on the structure under the occasional earthquake; thus the deformation constraint of the first step is a straight line perpendicular to the Ω_c axis; (2) the optimal design (point A in Figure 2.8(b)) is

controlled by the deformation constraint of the occasional earthquake (corresponding to IO performance level). However, in ASCE 41-13 (2014) nonlinear deformation is allowed in the RC moment frame under occasional earthquake. In addition, no evidence has been proved that the optimal result is controlled by the constraint of the occasional earthquake, such as point A' in Figure 2.8(a).

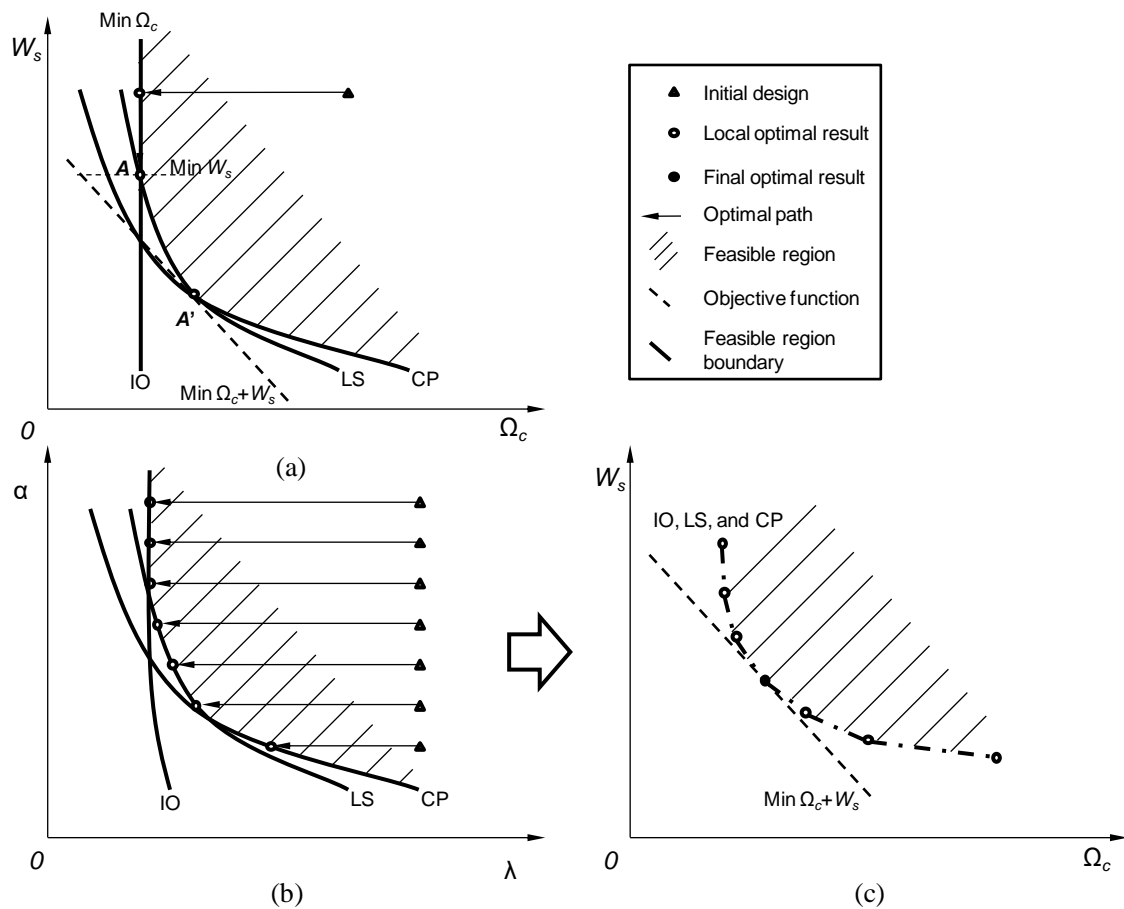


Figure 2.8 Comparison of the searching method of different optimal algorithms: (a) OC method proposed by Zou and Chan (2005); (b) and (c) optimal algorithm proposed in this study

Figures 2.8(b) and 2.8(c) demonstrates the searching paths of the two-step optimal

method proposed in this study. This method first adopts all the constraints of different hazard levels to determine the feasible region boundary in λ - α domain, then transforms it into Ω_c - W_s domain for optimal solution by nonlinear programming method. Several innovations of the proposed optimal PBSM method are that: (1) this method reduces numerous optimal variables (section size and reinforcement area of all elements) into only two variables (λ and α) based on some rational simplifications of construction and seismic design. Accordingly, the complexity of the optimization and the computational cost is highly reduced than the current optimal PBSM methods. (2) instead of repetitively applying complex nonlinear structural analyses, an explicit relationship is suggested to express the nonlinear deformation (plastic hinge rotation and inter-story drift) based on λ and single pushover analysis results, if the flexural strength of all elements remain unchanged. This explicit expression relates nonlinear deformation to λ and α , which can be transformed to Ω_c and W_s ; thus the optimal variables Ω_c and W_s in the objective function (Equation 2.1) can be used to formulate the nonlinear constraints (Equation 2.2). In addition, mathematical iteration is used to search the minimum λ for each α , instead of iterative method using complex nonlinear structural analyses. (3) the two-step method first determines the feasible region boundary by simultaneously using the constraints of multiple hazard levels; therefore, the possible inaccuracy described in Figure 2.8(c) is avoided. In addition, the two-step method separately using constraints and objective function at each step to reduce the complexity of the optimal process.

CHAPTER 3

IMPLEMENTATION OF THE PROPOSED OPTIMAL PBSD METHOD AND EXAMINATION OF THE OPTIMAL DESIGN

3.1 Implementation of the Proposed Optimal PBSD Method

3.1.1 Initial design of the original RC frame structure

The suggested optimal PBSD approach is applied to a six-story prototype RC moment frame building shown in Figure 3.1. The building, with a story height of 12 ft and a span of 30 in either direction, is located on a soft rock site in southern California, where the mapped short-period and 1-sec spectral accelerations for 5% critical damping for the hazard level with 2%/50 year probability of exceedance are $S_s = 1.50g$ and $S_1 = 0.60g$, respectively. Concrete compressive strength is assumed as 5000 psi and reinforcement yield strength as 60 ksi. The floors consist of 8 in. thick two-way slabs. A dead load of $DL = 117$ psf and a live load of $LL = 20$ psf act on the roof, whereas these values are 120 psf and 50 psf for all other floors.

Modal response spectrum analysis is used to perform a strength-based design. Based on requirements of ASCE 7-10 (2010), two vibration modes are considered to obtain design base shear and lateral loads. To meet the 2% inter-story drift limit, the section size of the beams is chosen as 22 in. \times 32 in. for the 1st to the 3rd floors and 20 in. \times 28 in. for the 4th to the 6th floors, and the section size of the columns as 29 in. \times 29 in. for the 1st to the 3rd floors and 24 in. \times 24 in. for the 4th to the 6th floors. The flexural design of members follows the seismic design provisions in ACI 318-14 (2014) as well as the additional design requirements described in Section 2.1.2.2.

Table 3.1 gives the needed negative and positive moment resistances for the beams and columns of an interior frame of the original design.

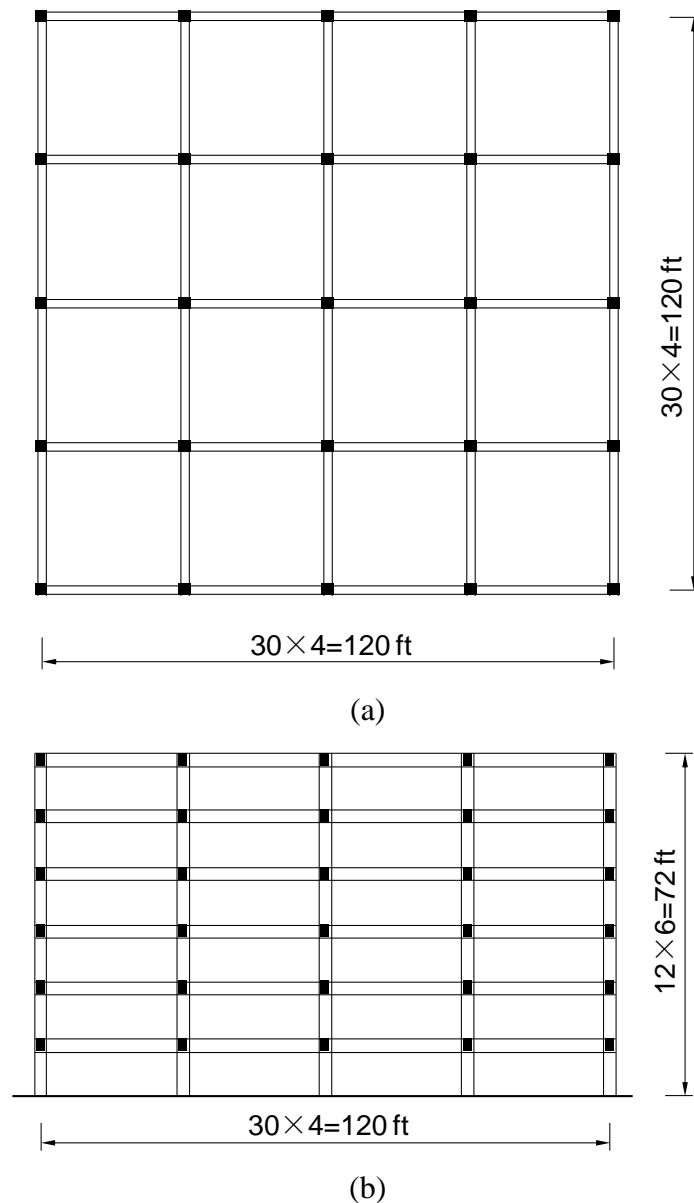


Figure 3.1 Prototype RC frame building: (a) floor plan; and (b) elevation plan

Table 3.1 Flexural capacity of the elements in the original structure (unit: kip-in.)

Floor	Beam				Column	
	External		Internal		External	Internal
	M^-	M^+	M^-	M^+		
Roof	3682	2974	4505	2974	4204	5001
5	5240	2974	5532	2974	5001	6399
4	5647	2974	6054	3027	5505	7798
3	6762	4310	7107	4310	9603	13400
2	6992	4310	7222	4310	10400	15002
1	6514	4310	6868	4310	11099	17002

3.1.2 Finite element model

Because the proposed optimal PBSB method is based on the nonlinear static analysis results of a two-dimensional (2D) frame, the interior RC moment frames designed with and without optimal PBSB are simulated using the software Open System for Earthquake Engineering Simulation (OpenSees 2017). The structural elements (beams and columns) are modeled using displacement-based line elements with zero-length plastic hinges at the element ends as shown in Figure 3.2(a). Each element contains two types of regions along its length: zero-length plastic hinge at element ends and elastic portion between the plastic hinges (Figure 3.2(b)). The nonlinear model suggested by Ibarra et al. (2005) is used to define the backbone moment-rotation of the zero-length plastic hinges (Figure 3.2(c)). The parameters of the backbone curves are defined based on ASCE 41-13 (2014). The elastic flexural stiffness of the beams and columns are defined as 30% and 50% of uncracked sectional stiffness, respectively. The gravity loads applied on the beams include factored dead load plus 50% of design live load.

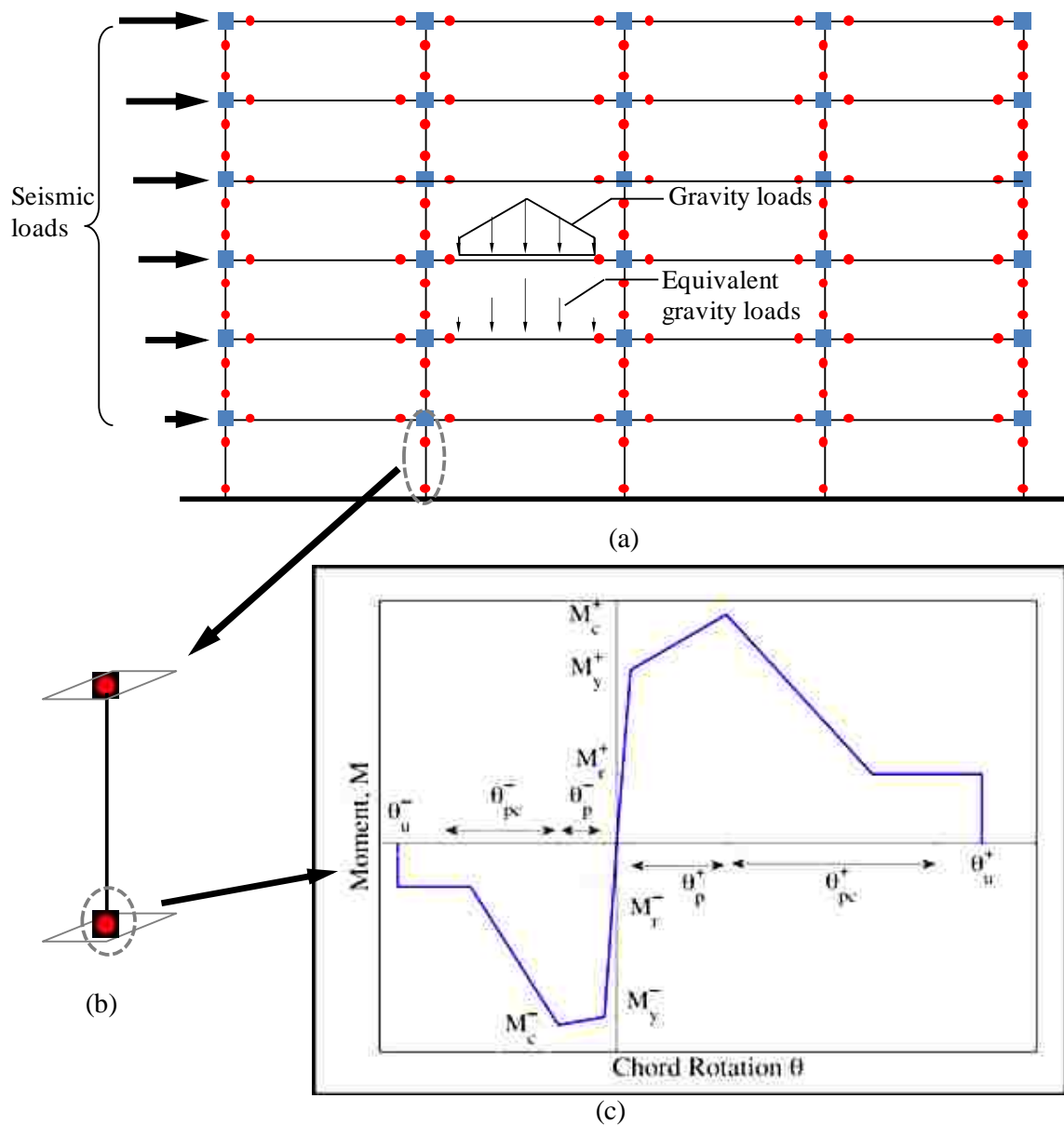


Figure 3.2 Illustration of (a) location of the zero-length plastic hinge elements; (b) concentrated plasticity model of one column; and (c) moment-rotation backbone curve of the plastic hinge suggested by Lignos and Krawinkler (2012)

The member flexural stiffness K_{ele} is composed by the stiffness of the line element K_{bc} and the stiffness of the zero-length plastic hinges K_{ph} , which are needed to be defined for the nonlinear model used in OpenSees. As a series system, K_{ele} is expressed as

$$K_{ele} = \frac{1}{\frac{1}{K_{bc}} + \frac{1}{K_{ph}}} = \frac{K_{bc}K_{ph}}{K_{bc} + K_{ph}} \quad \text{Equation 3.1}$$

K_{ele} shall be distributed appropriately to avoid the numerical instability problem caused by concentrating of all the stiffness on either the line element or the plastic hinges. Therefore, a method suggested by Ibarra and Krawinkler (2005) is adopted. This model defines the flexural stiffness of the plastic hinges is n times of the line element. Therefore, the value of K_{bc} and K_{ph} can be expressed by K_{ele} using Equation 3.2. Ibarra and Krawinkler (2005) suggested that the value of n shall be much larger than 1. However, due to the lack of further explanation, a series of numerical experiments are performed on the models with different n values (10, 100, and 1000). No difference is found among the results of these experiments; thus, the value of n is defined as 10 in this study.

$$K_{bc} = \frac{n+1}{n} K_{ele} \quad K_{ph} = (n+1) K_{ele} \quad \text{Equation 3.2}$$

DL of the beams and columns is normally assumed to be distributed along their longitudinal directions. Nevertheless, the *DL* of slabs, the superimposed DL and LL are uniformly applied on the top surfaces of slabs. As a results, the gravity loads transferred from the slabs to the beams (Figure 3.3(a)) are not uniformly distributed on the beams; instead, the load distribution should be linear, as shown in Figure 3.3(b). However, OpenSees cannot apply this linearly increased load along elements. Thus, these loads are transformed equivalently to five

concentrated loads, as shown in Figure 3.3(c). These concentrated loads can generate shear and flexural moment (Figure 3.3(b)) at beam ends identical to those in the beams subjected to linearly distributed loads. The lateral loads used to simulate the inertia forces caused by the ground acceleration are applied on the joints between beams on each story and the middle column. P-delta effects are considered in the OpenSees model through the geometry transformation of the columns.

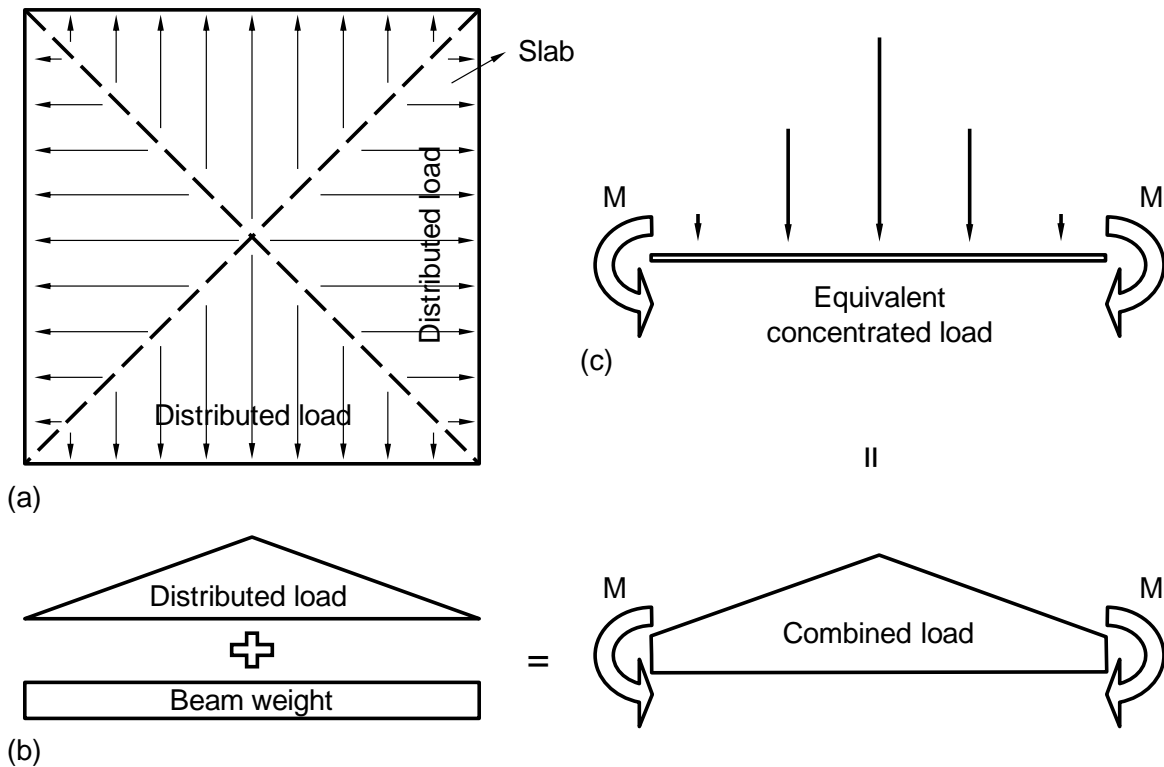


Figure 3.3 Transformation of loads: (a) two-way slab load distribution; (b) load combination; and (c) equivalent concentrated loads

3.1.3 Optimization

3.1.3.1 Feasible region boundary in λ - α domain

To apply the capacity spectrum method during optimization, S_{ae} needs to be determined for different levels of seismic hazard. Based on ASCE 7-05 (2005), S_{ae} is formulated as a function of mapped spectral accelerations at short period (S_s) and 1-sec periods (S_1) as well as the site condition. S_s and S_1 are 1.50g and 0.60g for very rare earthquakes (2%/50 years events) and 1.00g and 0.377g for rare earthquakes (10%/50-yrs events), respectively. S_s and S_1 for occasional earthquakes (50%/50 years events) unavailable from the seismic maps can be calculated based on ASCE 41-06 (2007) by Equation 3.3.

$$S_i = S_{i10/50} \left(\frac{P_R}{475} \right)^n \quad \text{Equation 3.3}$$

where S_i is the spectral response acceleration parameter at the desired probability of exceedance (“ i ”=“ S ” for short period, or “ i ”=“ 1 ” for 1-sec period); $S_{i10/50}$ is the spectral response acceleration parameter at a 10%/50-year exceedance rate (“ i ”=“ S ” for short period, or “ i ”=“ 1 ” for 1-sec period); the value of n is 0.29 for the earthquakes in California. Based on this equation and a mean return period of 72 years, S_s and S_1 are evaluated as 0.436g and 0.164g for occasional earthquakes. R - μ - T relationship suggested by Vidic et al. (1994), which is expressed by Equation 1.6 to 1.9 is employed. The peak ground motion acceleration (a_g) and velocity (v_g) at a specified seismic hazard, needed for applying the R - μ - T relationship, are determined based on the mapped

data provided by U.S. Geological Survey, and listed in Table 3.2.

Table 3.2 Peak ground motion acceleration and velocity for three hazard levels

	Three hazard levels		
	2%/50 year	10%/50 year	50%/50 year
a_g (cm/s ²)	461.47	244.94	106.79
v_g (cm/s)	43.24	22.56	9.62

The optimization procedure described previously is followed. Eight values for the relative strength factor, including $\alpha = \alpha_G = 0.28$ and $\alpha = 0.4$ to 1 at an interval of 0.1, are selected to determine the feasible region boundary in the λ - α domain. For each α , the optimal relative stiffness factor λ is evaluated for the three considered levels of seismic hazard and shown in Figure 3.4. For comparison purpose, this figure shows the optimal λ values evaluated based on the individual types of constraint (i.e., plastic hinge rotation limit, drift limit, and minimum relative

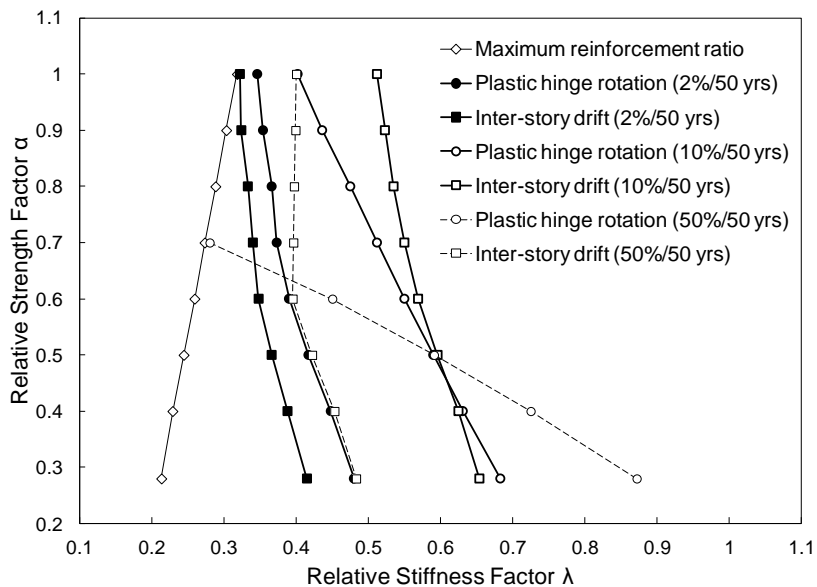


Figure 3.4 Feasible region of the six-story four-span RC moment frame in λ - α domain

stiffness factor) for each seismic hazard level. It is seen that λ is approximately linear with respect to α except for inter-story drift due to occasional earthquakes. In general, λ decreases with increased α . In other words, the flexural strength and stiffness of the structural members are not independent to each other in terms of the optimization results.

As seen in Figure 3.4, if no strength reduction is considered ($\alpha = 1$), inter-story drift limit for LS under rare earthquakes governs the optimal relative stiffness factor λ . In this case, λ is determined as 0.51, leading to a 29% reduction in cross-sectional area. If inter-story drift is not taken as a constraint, the optimal relative stiffness factor becomes $\lambda = 0.40$, controlled almost identically by plastic hinge rotation limit for LS under rare earthquakes or inter-story drift limit for IO under occasional earthquakes.

The pairs of selected α and the governing optimal λ based on all constraints constitute the feasible region boundary in the α - λ domain shown in Figure 3.4. The optimal λ is controlled by either inter-story drift ratio limit for Life Safety (LS) under rare earthquakes if $0.5 \leq \alpha \leq 1$ or plastic-hinge rotation limit for Immediate Occupancy (IO) under occasional earthquakes if $\alpha < 0.5$. Note that the inter-story drift limit under occasional earthquake is far from controlling the feasible region boundary. This result is remarkably different from some existing optimal PBSO approaches for RC frames (Zou and Chan, 2005; Li et al., 2010; and Zou et al., 2007), which optimized section size based only on the inter-story 0.2 drift limit under minor earthquakes. Moreover, deformation limits defined for CP under very rare earthquakes also have no impact on the feasible region boundary.

3.1.3.2 Feasible region boundary in Ω_c - W_s domain and optimal solution

For each pair of α and λ on the feasible region boundary shown in Fig. 3.3, the needed section size is determined, and the flexural designs of beams and columns are conducted. Then, the total weight of steel reinforcement W_s and total concrete volume Ω_c for all the beams (including those in the transverse direction) and the columns located between the slab center lines enclosing an interior frame are evaluated. Figure 3.5 shows the new feasible region boundary defined in the Ω_c - W_s domain. To define the objective function expressed in Equation 2.1, the unit cost of concrete and steel reinforcement, c_c and c_s , are calculated based on the construction cost data published by the BNi Building News (2015) and RS Means (2015) and listed in Table 3.3. c_c and c_s consider both material and labor cost; c_c also includes formwork cost defined based on four uses. For comparison purpose, Table 3.3 also provides the unit costs

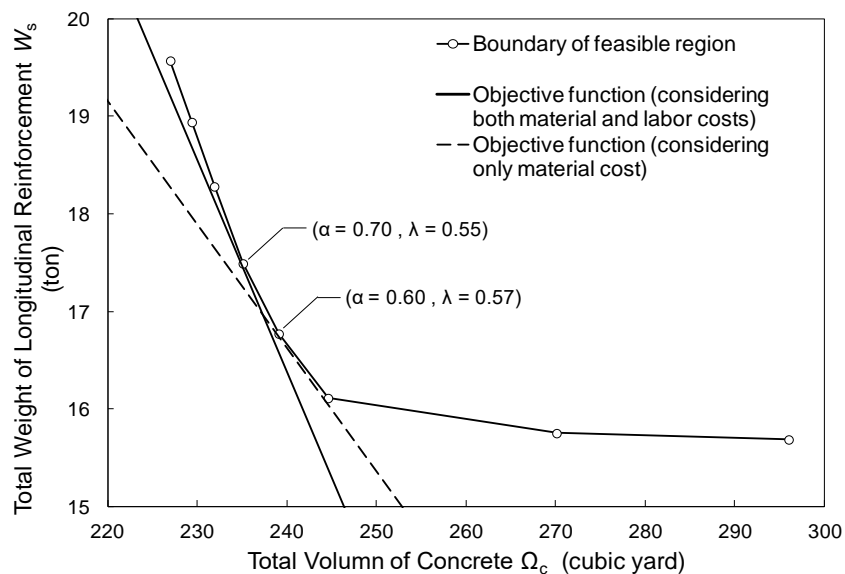


Figure 3.5 Feasible region boundary and optimal solutions in Ω_c - W_s domain

considering only the material cost.

Table 3.3 Unit cost of material only and combined material and labor cost

Material Cost Only		Material Cost and Labor Cost	
unit cost of concrete (c_c)	unit cost of steel reinforcement (c_s)	unit cost of concrete (c_c)	unit cost of steel reinforcement (c_s)
\$119/C.Y.	\$940/ton	\$352/C.Y.	\$1624/ton

The solid line in Figure 3.5 shows the object function. The tangent point between the objective function and feasible region gives the optimal solution in terms of W_s and Ω_c , which correspond to $\alpha = 0.70$ and $\lambda = 0.55$. The optimal design leads to a 30% reduction in needed flexural strength and a 26% reduction in cross-sectional area from the initial strength-based design. For comparison purpose, the dashed line in Figure 3.5 represents the object function considering only material cost, which is generally used by existing optimal PBS methods (Fragiadakis and Papadrakakis, 2008; Grierson et al., 2006; and Xu et al., 2006). The optimal solution is $\alpha = 0.60$ and $\lambda = 0.57$. The optimal design corresponds to a 40% reduction in seismic design loads and a 25% reduction in section area from the initial strength-based design.

Figure 3.6 shows the capacity curve for the optimized structure ($\lambda = 0.55$, $\alpha = 0.70$) in the equivalent SDOF system and the demand curves (inelastic displacement–acceleration spectra) for the three levels of considered earthquake hazard. As shown by the capacity curve derived from nonlinear static analysis, the structure experiences little strength degradation after reaching the peak load. Moreover, the demand curve for occasional earthquakes intersects the first branch

of the idealized bilinear capacity curve, indicating an overall elastic behavior of the optimized structure under occasional earthquakes.

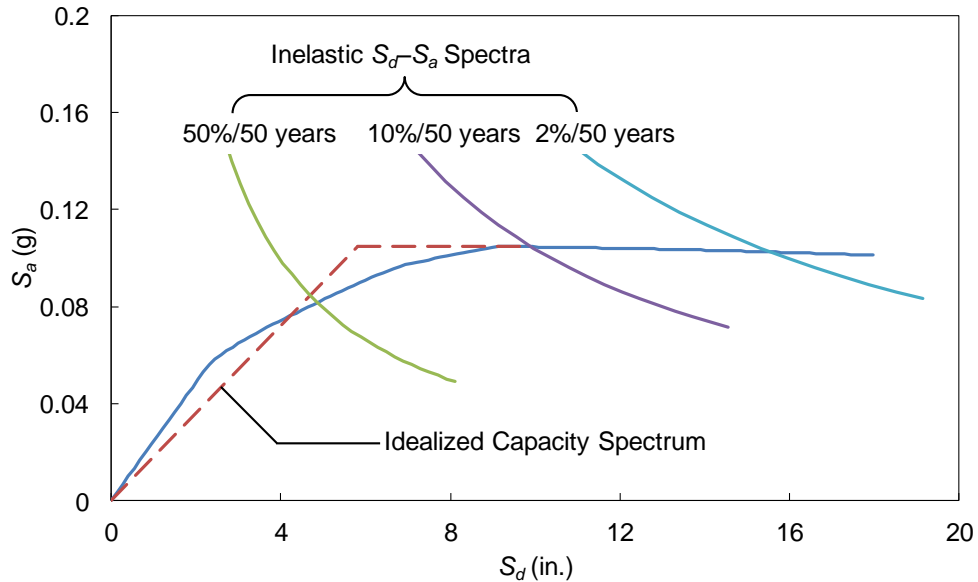


Figure 3.6 Application of the capacity spectrum method to determine the seismic deformation demands of occasional, rare, and very rare earthquakes

3.1.3.3 Construction cost reduction due to optimal design

The costs of the interior frame based on the initial design and the cost based on the optimal design are evaluated and compared in Table 3.4. The optimal design reduces the needed flexural strengths of the beams and columns by 30%. However, because of the 14% decrease in section size, the cost of flexural reinforcement in the optimal design is reduced by only 5%. Major cost saving is contributed by the significantly decreased concrete consumption and the corresponding labor cost. The transverse reinforcement needed for shear and confinement in the beams and columns are designed based on ACI 318-14 (2014). The section size reduction

decreases the length of the transverse reinforcement but increases the number of needed transverse reinforcements. Therefore, the total weight of transverse reinforcement is almost identical between the optimal and original structures.

Table 3.4 Comparison of cost for the initial and optimal designs

	Original design (\$)	Optimal Design (\$)	Cost Reduction (%)
Concrete	37,497	27,977	25.4
Flexural reinforcement	17,305	16,441	4.99
Transverse reinforcement	30,860	29,171	5.47
Labor	86,098	66,805	22.4
Total cost without transverse reinforcement	140,900	111,223	21.1
Total cost with transverse reinforcement	171,760	140,394	18.3

3.2 Examination of Optimal Design

Compared with the initial strength-based design, the optimal PBSB considerably reduces needed flexural stiffness and strength of the beams and columns. Moreover, the proposed optimization approach estimates the peak dynamic response of a nonlinear system using capacity spectrum method. Therefore, whether the optimal design derived from the proposed method can satisfy the requirements of the selected performance levels under multiple hazard levels shall be examined. If the hysteretic behavior of structural components is properly defined (Deierlein et al., 2010), nonlinear time-history analyses provide a more realistic structural response than the nonlinear static methods considered in the spectrum method, especially for moderate and severe earthquakes and for tall buildings, if the hysteretic behavior of structural components is properly

defined (Deierlein et al., 2010). Therefore, nonlinear dynamic analyses using ten ground motions are performed to examine the seismic performance of the optimized building.

3.2.1 Hysteretic behavior model

The concentrated plasticity model with two zero-length plastic hinges at the element ends and an elastic portion between the plastic hinges described in Section 3.1.2 is used in the time-history analyses of the 2D models of the optimal and original structures. The elastic portion has a reduced flexural stiffness to account for the effects of concrete cracking. The plastic hinges are defined with a backbone moment-rotation relationship and hysteretic behavior. The hysteretic behavior of the plastic hinges is defined by the element strength and stiffness degradations under cyclic loading. Figure 3.7 demonstrates the modified Ibarra-Medina-Krawinkler deterioration model (Ibarra et al., 2005) used in this study. This model was calibrated by experimental data of

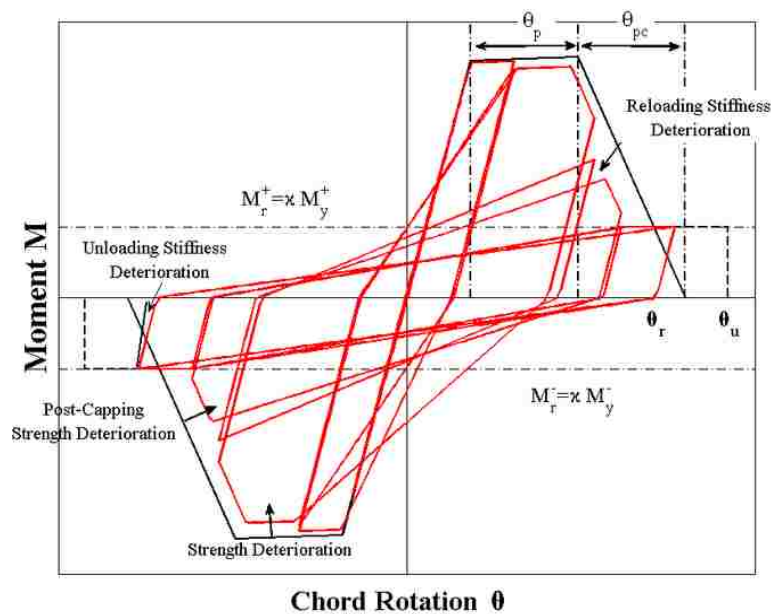


Figure 3.7 Hysteretic behavior of modified Ibarra-Medina-Krawinkler model (Lignos and Krawinkler, 2012)

200 RC beams and proved reliable.

When using the Ibarra-Medina-Krawinkler model, the strength, stiffness and ductility properties are defined per ASCE 41-13 (2014) to generate the backbone curve. The hysteretic behavior of this model is determined mainly based on two groups of parameters: cyclic deterioration parameters and deterioration rate (Ibarra et al., 2005). The parameters in the former group reflect the cumulative rotation capacity, while the latter reflects the rate of cyclic deterioration. Each group of parameters includes four types of deterioration: basic strength, post-capping strength, unloading stiffness, and accelerated reloading stiffness. Using an identical value for the four deterioration parameters in the same group can adequately describe the deterioration behavior (Lignos, 2008). Therefore, the values of cyclic deterioration parameters are selected in this study all as 1.0, which has about 50% probability of exceedance (Lignos and Krawinkler, 2010). The reasonable range of deterioration rate is between 1.0 to 2.0; thus, in this study, the default value in OpenSees for the rate of deterioration (1.0) is adopted to define the hysteretic behavior of the model with a fast deterioration process in the early cycles but a slow deterioration process in the late cycles.

3.2.2 Earthquake record selection and scaling

3.2.2.1 Earthquake record selection

Ten earthquake records are selected from the PEER (Pacific Earthquake Engineering Research Center) ground motion database NGA-West 2 to conduct dynamic analyses. The ground motion records cover different fault types, last durations, and distances to the fault. Table

3.5 gives the selected motions, earthquake magnitude, duration, closest distance to surface projection of the fault plane (R_{jb}), closest distance to the fault plane (R_{rup}), and fault type.

Table 3.5 Details of selected ground motions

No.	Year	Earthquake	Record No. in database	Magnitude	Duration (sec.)	R_{jb} (km)	R_{rup} (km)	Fault Type
1	1983	Coalinga	357	6.36	12.2	32.8	34.0	REV
2	1984	Morgan Hill	472	6.19	21.8	31.9	31.9	SS
3	1989	Loma Prieta	748	6.93	12.3	43.9	44.1	REV/OB
4	1994	Northridge	948	6.69	17.3	41.1	41.4	REV
5	1999	Chi-Chi	1259	7.62	20.1	43.5	47.9	REV/OB
6	1999	Hector Mine	1762	7.13	26.7	41.8	43.1	SS
7	1992	Landers	3752	7.28	27.3	45.3	45.3	SS
8	2004	Niigata	4230	6.63	40.3	36.8	39.4	REV
9	2007	Chuetsu-oki	5261	6.80	56.8	42.0	45.4	REV
10	2008	Iwate	5779	6.90	29.1	36.3	36.3	REV

Note: Fault mechanism = REV: Reverse; SS: Strike-slip; OB: Oblique

The selected ground motions with different magnitude from M6.2 to M7.3 earthquakes at soft rock sites, where the average shear wave velocity in the upper 30 meters of the site ($v_{s,30}$) is between 360 m/sec. and 760 m/sec.. Moreover, the duration between 5% to 95% of total cumulative energy for each selected record is longer than 12 sec. to ensure adequate structural reaction time. Six of the ten selected ground motions were recorded in California. Fourier transformation is performed on each record by SeismoSignal platform to eliminate the records that may resonate with the optimal or original structures. To avoid the effect of the near-source earthquake, both R_{rup} and R_{jb} for each record are larger than 30 km, which was taken as the maximum distance for near-source earthquakes by Iervolino and Cornell (2008). Figure 3.8

shows the unscaled horizontal ground acceleration time-history of the 10 selected earthquakes.

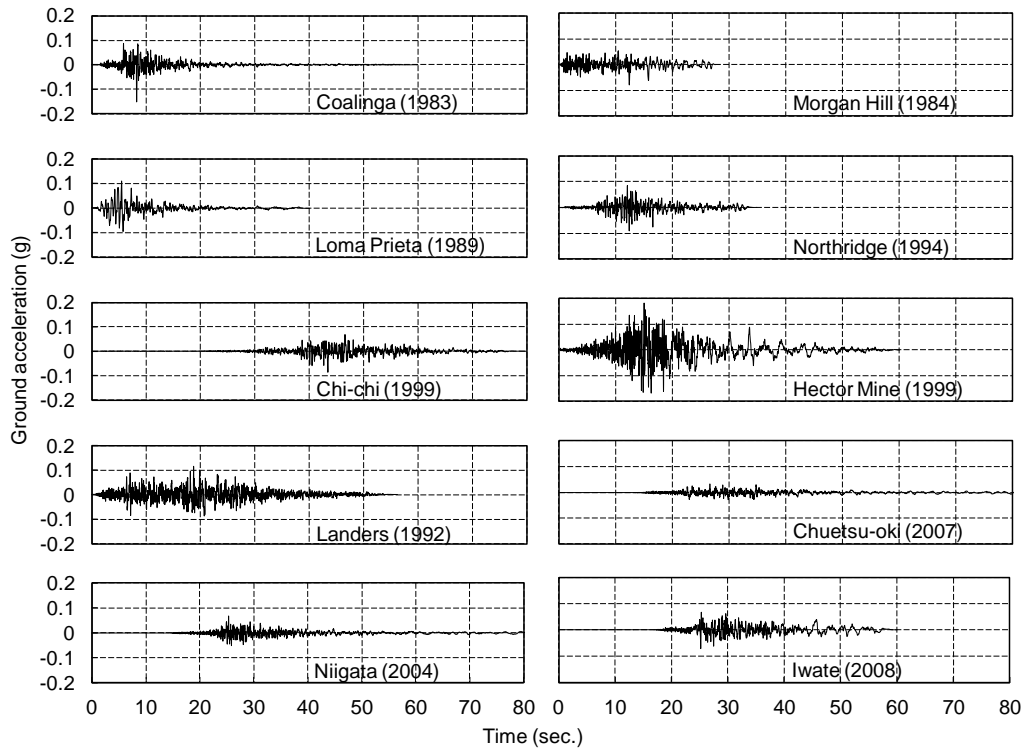


Figure 3.8 Time-history of unscaled horizontal ground acceleration for ten earthquakes

3.2.2.2 Earthquake record scaling

To represent the three hazard levels, the peak ground accelerations (PGAs) of the chosen records are scaled so that the response spectrum for each seismic hazard matches the design spectrum.

ASCE 7-10 (2010) requires that the arithmetic mean of the response spectrum acceleration shall not be less than the acceleration of design spectrum with 5% damping ratio within $0.2T$ to $1.5T$, if the 2D analyses are performed using at least seven record. The online tools provided by PEER ground motion database are adopted to scale the ten ground motion records. Considering the increase of the structure vibration period during the seismic effect, the weight factors for $0.2T$, $1.0T$ and $1.5T$ are determined as 4.0, 10.0 and 6.0, respectively. Table 3.6 lists the scaled factors

and the scaled PGA values for the ten ground motions. Figures 3.9, 3.10, and 3.11 show the scaled time-history records corresponding to very rare, rare and occasional hazard levels, respectively. Figure 3.12 shows the response spectrum of each ground motion, the average response spectrum, and the design spectrum for very rare, rare and occasional earthquakes.

Table 3.6 Details of scaled ground motions

No.	Earthquake	Scaled Factor			Scaled PGA (g)		
		occasional	rare	very rare	occasional	rare	very rare
1	Coalinga	1.994	4.583	7.190	0.301	0.692	1.086
2	Morgan Hill	2.520	5.792	9.087	0.199	0.458	0.718
3	Loma Prieta	1.376	3.164	4.963	0.153	0.351	0.551
4	Northridge	2.664	6.124	9.607	0.242	0.557	0.874
5	Chi-Chi	2.230	5.126	8.041	0.194	0.446	0.700
6	Hector Mine	0.862	1.982	3.109	0.157	0.361	0.566
7	Landers	1.758	4.042	6.341	0.200	0.461	0.723
8	Niigata	4.012	9.223	14.470	0.273	0.627	0.984
9	Chuetsu-oki	4.362	10.027	15.731	0.144	0.331	0.519
10	Iwate	1.930	4.434	6.957	0.139	0.319	0.501

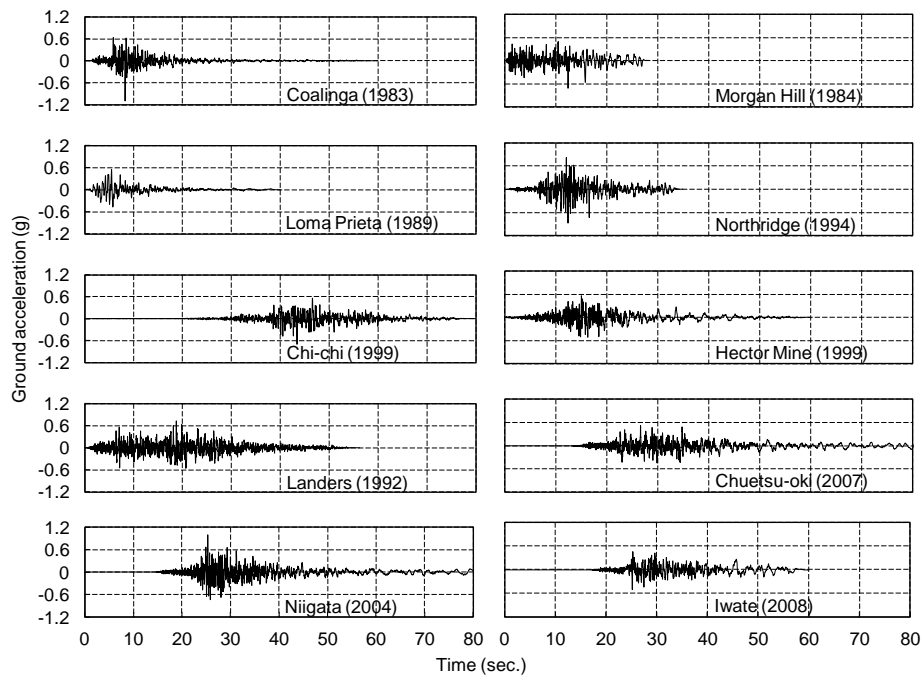


Figure 3.9 Time-history of ten horizontal ground acceleration scaled according to very rare earthquake level

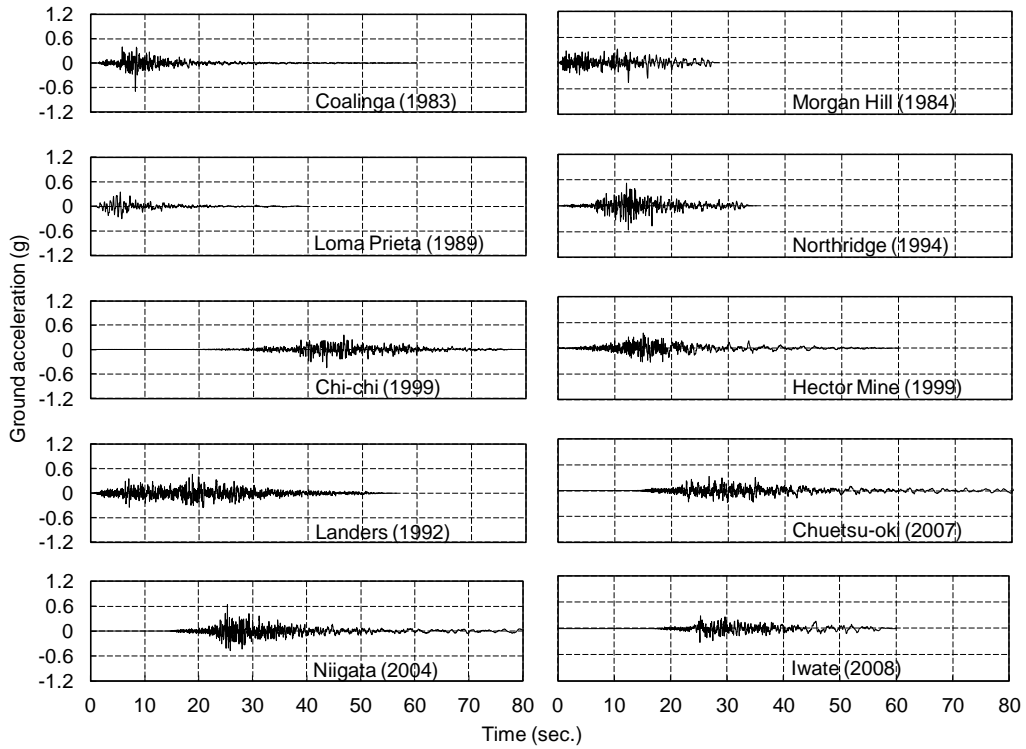


Figure 3.10 Time-history of ten horizontal ground acceleration scaled according to rare earthquake level

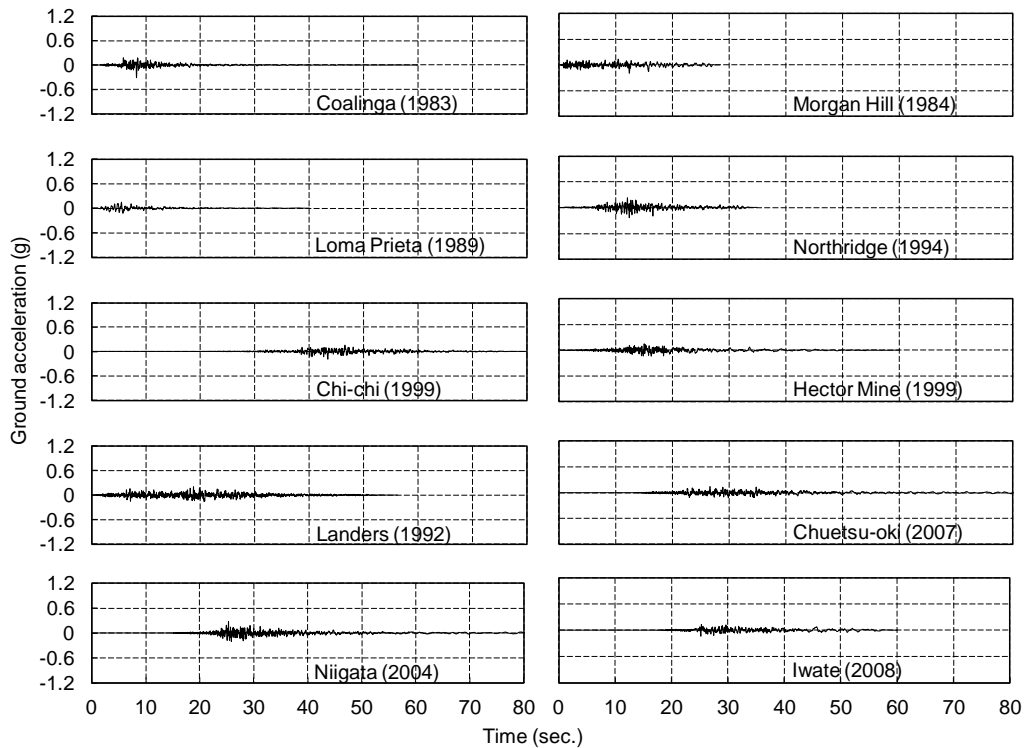


Figure 3.11 Time-history of ten horizontal ground acceleration scaled according to occasional earthquake level

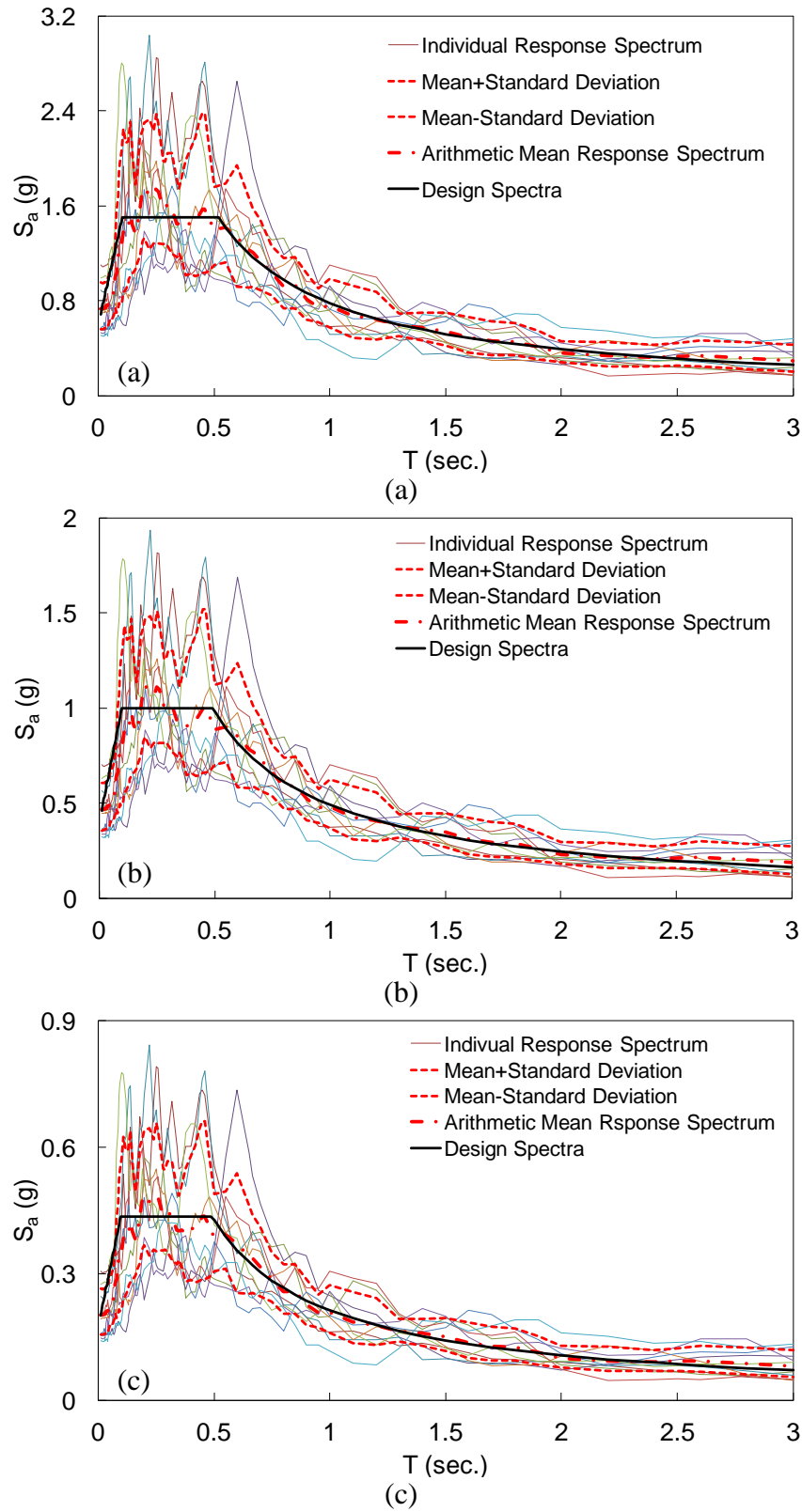


Figure 3.12 Acceleration response spectra and scaled ground motions for different hazard levels: (a) very rare earthquake; (b) rare earthquake; and (c) occasional earthquake

3.2.3 Examination results and discussions

Dynamic analyses are conducted on the optimal and original structures using the scaled ground motions under three hazard levels. The simulation results are then summarized and analyzed. Two types of peak nonlinear deformation (inter-story drift ration and plastic hinge rotation) of the optimal and original structures are examined by their performance-based limits.

3.2.3.1 Results of optimal design

Inter-story drift ratio

In general, the average peak dynamic response in terms of inter-story drift ratio meets the target performance requirements under the three levels of seismic hazard. Figure 3.13 shows the profiles of peak inter-story drift γ_{max} caused by individual ground motions and the average γ_{max} . In this figure, the average γ_{max} under occasional and rare earthquakes are almost identical to the target limits of IO performance level ($[\gamma]_1 = 1\%$) and of LS performance level ($[\gamma]_2 = 2\%$), while the average γ_{max} very rare earthquakes is much less than the target limit of CP performance levels ($[\gamma]_3 = 4\%$). These observations are consistent with the results shown in Figure 3.4 derived from the proposed optimal PBSB method, except that the average peak inter-story drift of occasional earthquakes obtained from the dynamic analyses is larger than the results shown in Figure 3.4. In addition, mainly due to the effect of higher modes, the maximum average γ_{max} of the structure occurs in either the 4th or the 5th floor, rather than in the 1st or 2nd floor.

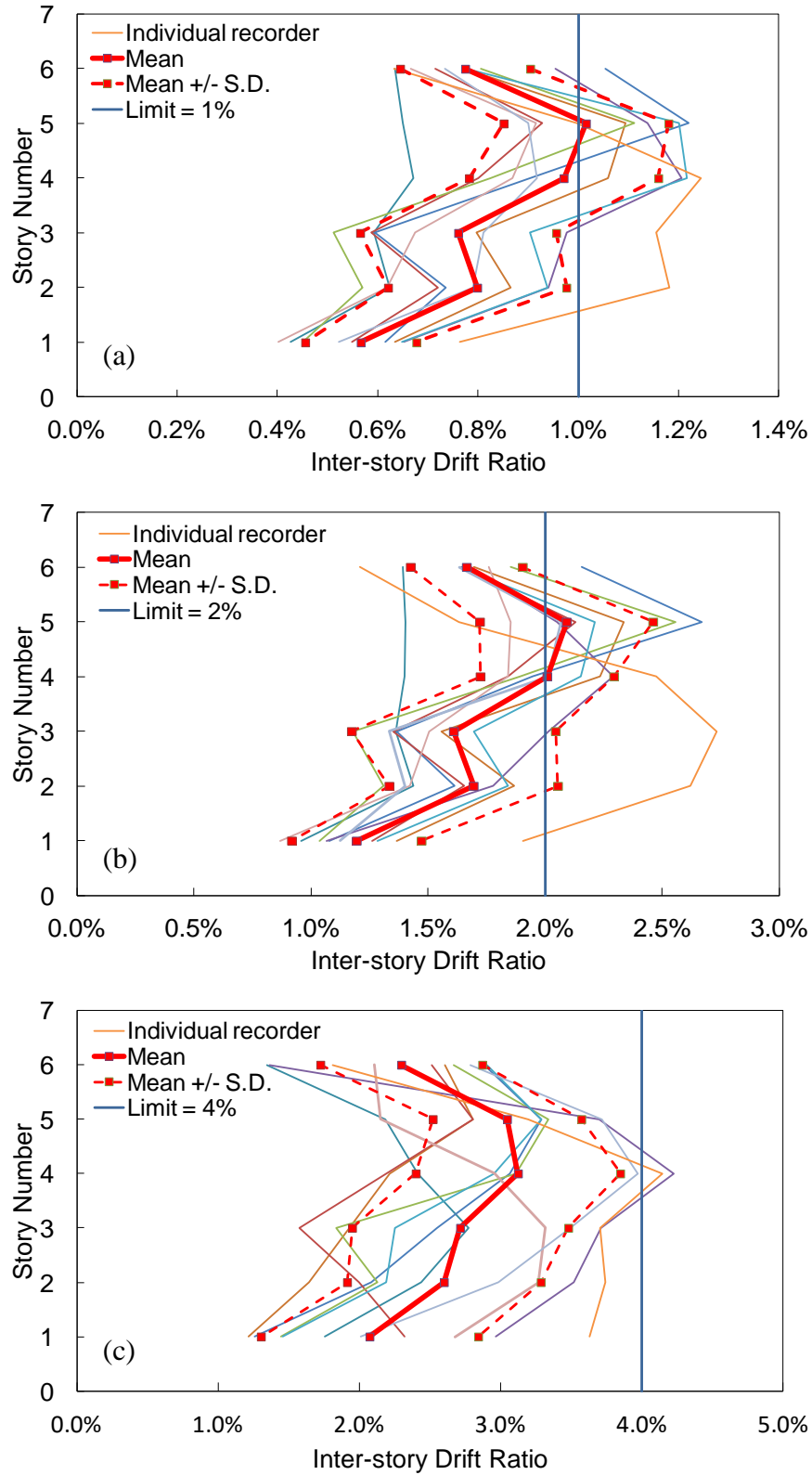


Figure 3.13 Peak inter-story drift ratio for optimal design subjected to ground motions scaled for (a) occasional earthquakes; (b) rare earthquakes; and (c) very rare earthquakes

Table 3.7 shows that, for all three hazard levels, the maximum standard deviations (S.D.) of the peak inter-story drift appear on the 3rd story, above which the section sizes of beams and columns change. The relative variability of the inter-story drift is measured by the coefficient of variation (COV), the ratio between S.D. and the mean value. Because the values of COV are similar among the three hazard levels, a similar dispersion exists even though the nonlinearity of the structure as well as hazard levels are different.

Table 3.7 Maximum standard deviation of inter-story drift ratios of optimal structure

	2%/50 year	10%/50 year	50%/50 year
Story of max. S.D.	3	3	3
Maximum S.D.	0.0077	0.0044	0.0020
Mean drift ratio of max. S.D.	0.0272	0.0161	0.0076
COV	0.28	0.27	0.26

Plastic hinge rotation

The rotation capacity of a plastic hinge varies during dynamic loading due to the change in beam shear or column axial force. Thus, a normalized plastic hinge rotation, defined as the ratio of average peak plastic hinge rotation demand to capacity ($\theta_{max}/[\theta]_p$), is considered ($p = 1, 2, 3$ for IO, LS and CP performance levels, respectively). Figure 3.14 shows the location of normalized plastic hinge rotation for the three levels of seismic hazard. Under occasional earthquakes, only one ground excitation causes yielding and, as shown in Figure 3.14(a), the yielding occurs only in a few beams on the 4th and 5th stories. Under rare earthquakes, all the beams yield (Figure 3.14(b)). The normalized plastic hinge rotation ranges from 0.20 to 0.518 and

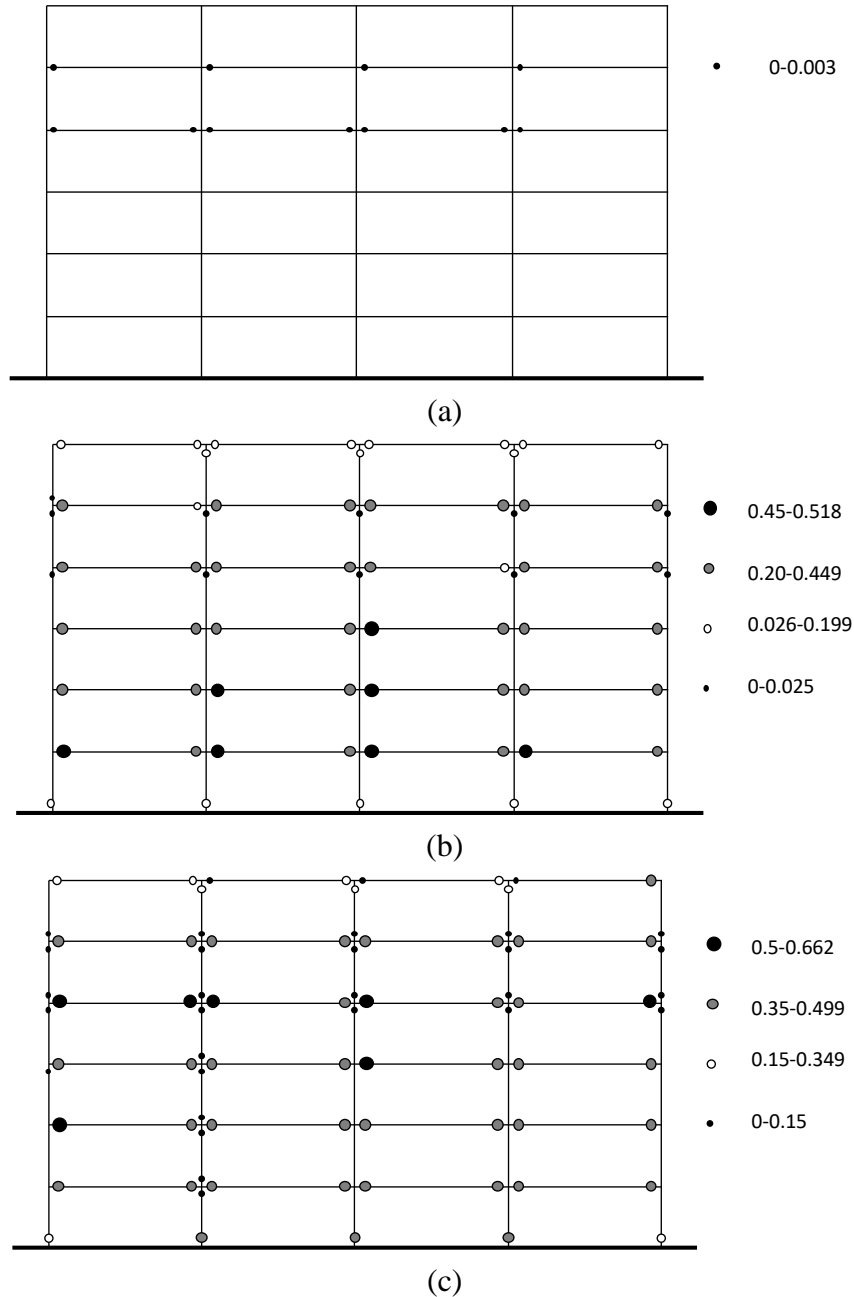


Figure 3.14 Ratio of average peak plastic hinge rotation demand to capacity ($\theta_{\max}/[\theta]$) for optimal design subjected to ground motions scaled for (a) occasional earthquakes; (b) rare earthquakes; and (c) very rare earthquakes

is much lower in the columns than in most of the beams. The large $\theta_{\max}/[\theta]_2$ (0.45 to 0.518)

appear on the 1st to 3rd stories. Under very rare earthquakes, the average peak plastic rotation

demand is less than 67% of capacity in any member (Figure 3.14(c)). The large $\theta_{max}/[\theta]_3$ (0.5 to 0.662) appear on the 3rd to 4th stories. Figure 3.14(c) also shows that the normalized column plastic rotations at the supports of the exterior columns are less than that of the three interior columns.

As shown in Figures 3.14(b) and 3.14(c), column yielding occurs at the upper stories, which is not predicted by the nonlinear static analyses, indicating the effects of higher vibration modes. Note that even though the average peak plastic hinges appear at both ends of all the columns on the same story, these plastic hinges occur at different time or under different earthquake records; thus weak story failure mechanism does not appear.

3.2.3.2 Result of original design

Inter-story drift ratio

In general, the force-based design is conservative, because the average peak inter-story drifts are far less than the target performance requirements under the three hazard levels, as shown in Figure 3.15, the values of the maximum $\gamma_{max}/[\gamma]$ among all stories are 0.73, 0.81 and 0.59 for the occasional, rare and very rare earthquakes, respectively. This observations is consistent with the optimal results derived from the optimal PBSD, in which the largest and smallest $\gamma_{max}/[\gamma]$ appear under rare and very rare earthquakes, respectively. In addition, the effect of higher modes occurs on the model, because the maximum average γ_{max} appears on the 5th floor.

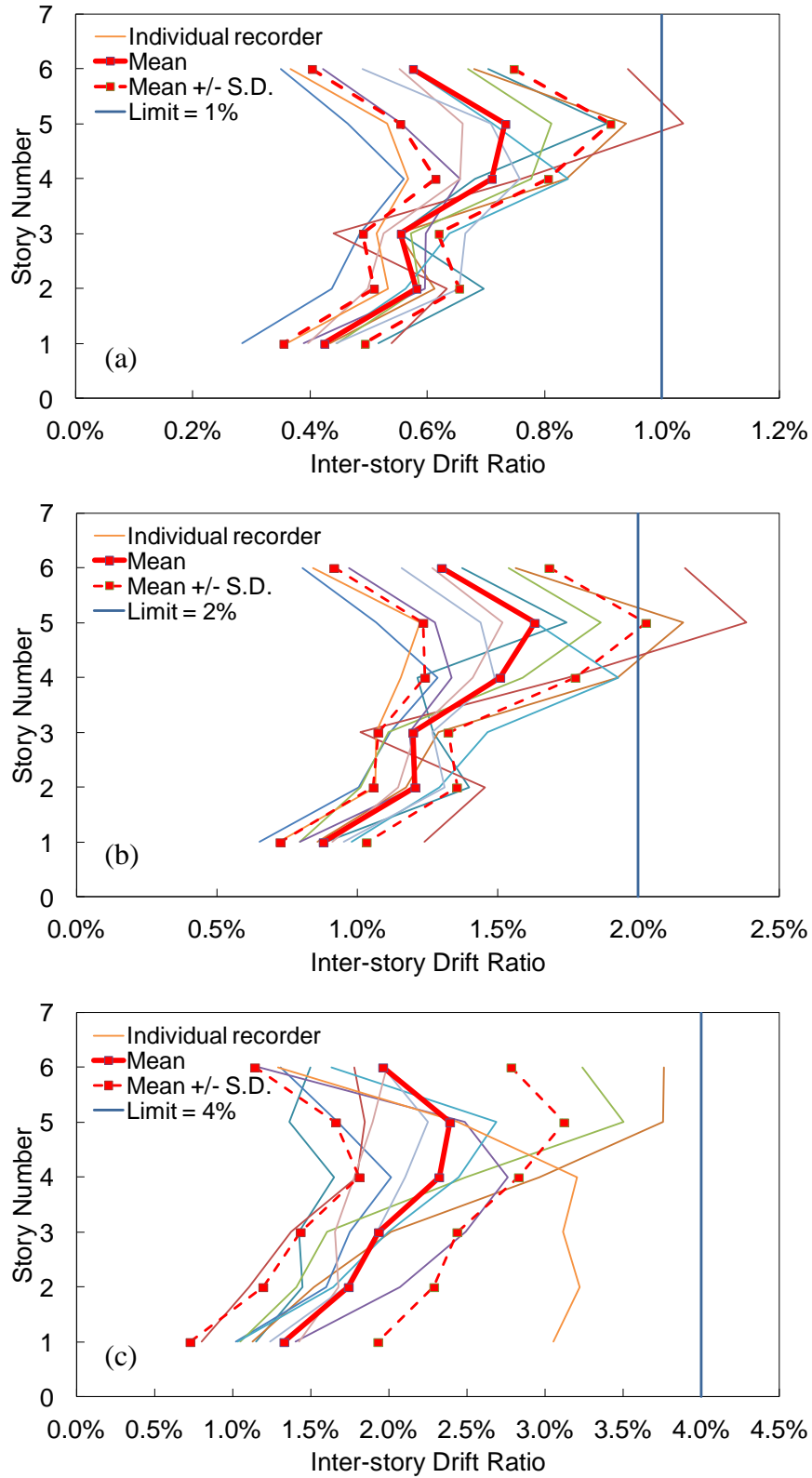


Figure 3.15 Inter-story drift ratio for original design subjected to ground motions scaled for (a) occasional earthquakes; (b) rare earthquakes; and (c) very rare earthquakes

Table 3.8 shows that, for all three hazard levels, the maximum S.D. of the peak inter-story drift appears on the 5th story, where the maximum peak inter-story drift occurs. The values of COV for both optimal and original structures are similar, which indicates that an identical dispersion exist even though the strength and stiffness of the structures as well as hazard levels are different.

Table 3.8 Maximum standard deviation of inter-story drift ratio of original structure

	2% / 50 year	10% / 50 year	50% / 50 year
Story of max. S.D.	5	5	5
Maximum S.D.	0.0073	0.004	0.0018
Mean drift ratio of max. S.D.	0.0239	0.0163	0.0073
COV	0.31	0.25	0.25

Plastic hinge rotation

No plastic hinge appears on the original structure under the ground motions scaled for occasional earthquakes. Figure 3.16 shows the distribution of normalized plastic hinge rotation for two greater levels of seismic hazard. The maximum normalized plastic hinge rotations are 0.43 and 0.47 for the rare and very rare earthquakes, respectively. Under rare earthquakes, all the beams and some columns on the 5th and 6th stories yield (Figure 3.16(a)). As shown in this figure, most large values of $\theta_{\max}/[\theta]_2$ (0.2 to 0.425) appear on the 3rd to 5th stories. Under very rare earthquakes, large values of $\theta_{\max}/[\theta]_3$ (0.35 to 0.472) appear on the 3rd to 5th stories (Figure 3.16(b)). Column yielding occurs in the upper stories, which is not predicted by the nonlinear static analyses, indicating the effects of higher vibration modes.

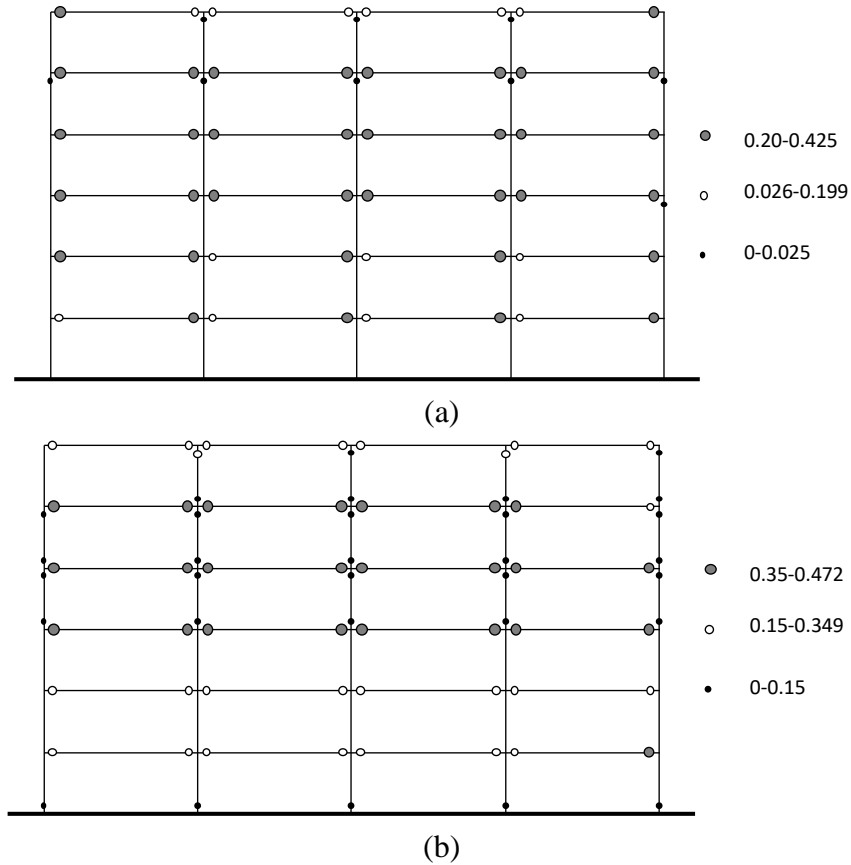


Figure 3.16 Ratio of average peak plastic hinge rotation demand to capacity ($\theta_{max}/[\theta]$) for original structure subjected to ground motions scaled for (a) rare earthquakes and (b) very rare earthquakes

3.3 Verification of the Optimal Design

To verify whether the feasible region boundary has an abrupt change around the optimal design, further analyses are extended to the seismic response and construction cost of the eight structures with the design variable values close to the optimal design ($\lambda = 0.55$, $\alpha = 0.70$). Compared with the nonlinear static analysis used in the proposed optimal PBSO method, nonlinear dynamic analysis can better reflect the actual structural response under the seismic effect. Therefore, the dynamic analyses are performed on the eight structures to obtain their

seismic response. The values of pairs of λ and α used to design these eight structures are (0.5, 0.65), (0.5, 0.7), (0.5, 0.75), (0.55, 0.65), (0.55, 0.75), (0.6, 0.65), (0.6, 0.7), and (0.6, 0.75) as shown in Figure 3.17(a). Based on the method described in Section 2.2.3.3, these nine points are

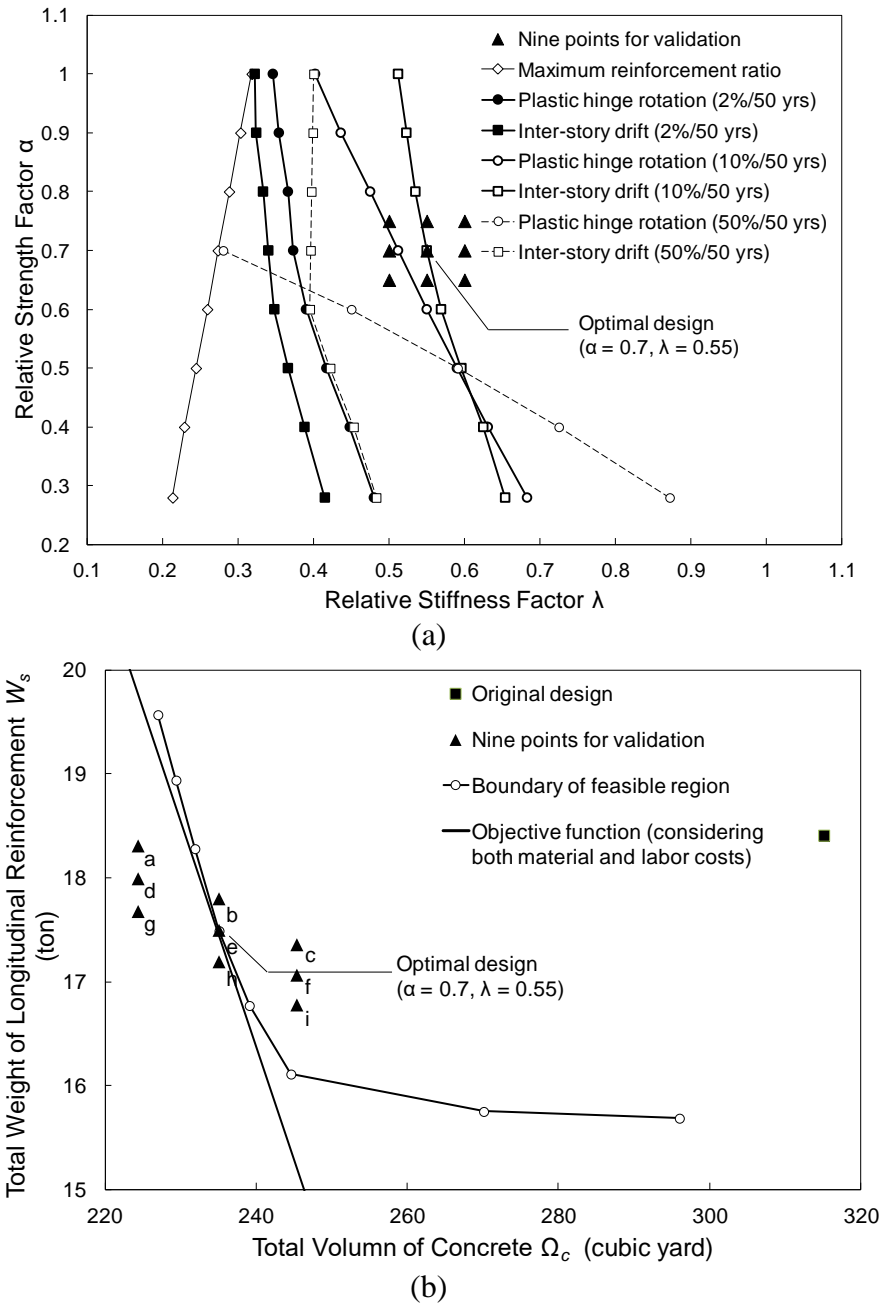


Figure 3.17 Feasible region and the design variables of nine structures in (a) λ - α domain and (b) Ω_c - W_s domain

transformed from the λ - α domain to the Ω_c - W_s domain shown in Figure 3.17 (b) to show the corresponding material consumptions.

The eight structures are designed based on the values of corresponding λ and α shown in Figure 3.17 (a) and requirements of ASCE 7-10 (2010). Nonlinear analysis models of these eight structures are established based on the method given in Section 3.1.2. Dynamic analyses are performed on the eight structures to obtain the peak normalized deformations. Ten earthquake records selected in Section 3.2.2.1 are adopted to simulate the seismic effect. These records are scaled based on the response spectra of the three hazard levels, very rare, rare, and occasional earthquake hazard levels, as mentioned in Section 3.2.2.2. The peak normalized deformations, $\gamma_{max}/[\gamma]$ and $\theta_{max}/[\theta]$, of the structures under a hazard level are the average values of the normalized deformations caused by the ten ground motions.

The dynamic analysis results for each of the eight structures indicate that the peak inter-story drift ratio of the structure under rare earthquake governs the peak normalized deformations. This observation is consistent with the peak normalized deformation of the optimal design ($\lambda = 0.55$, $\alpha = 0.70$). Figure 3.18 shows the values of peak normalized inter-story drift ratio of the eight structures and the structure with optimal design under rare earthquake. In this figure, the peak inter-story drift ratio of seven structures, including the optimal design, is larger than 1.0, that is, the nonlinear deformations of these structures exceed performance limits. For the other two structures ($\lambda = 0.6$, $\alpha = 0.7$ and $\lambda = 0.6$, $\alpha = 0.75$), the peak normalized inter-story drift ratio is less than 1.0. Among the eight points and the optimal design, if the values

of λ are identical, the value of $\gamma_{max}/[\gamma]$ increase with the decline of α , except point d; if the values of α are identical, the value of $\gamma_{max}/[\gamma]$ increase with the reduction of λ , except point g. The value of $\gamma_{max}/[\gamma]$ at points d and g are very close to that of the points around them. Therefore, in general, a continuous variation tendency exists in the area determined by the eight points without abrupt change. In addition, the optimal solution determined from dynamic analyses must be located within the area determined by points b, c, e, f, h, and i.

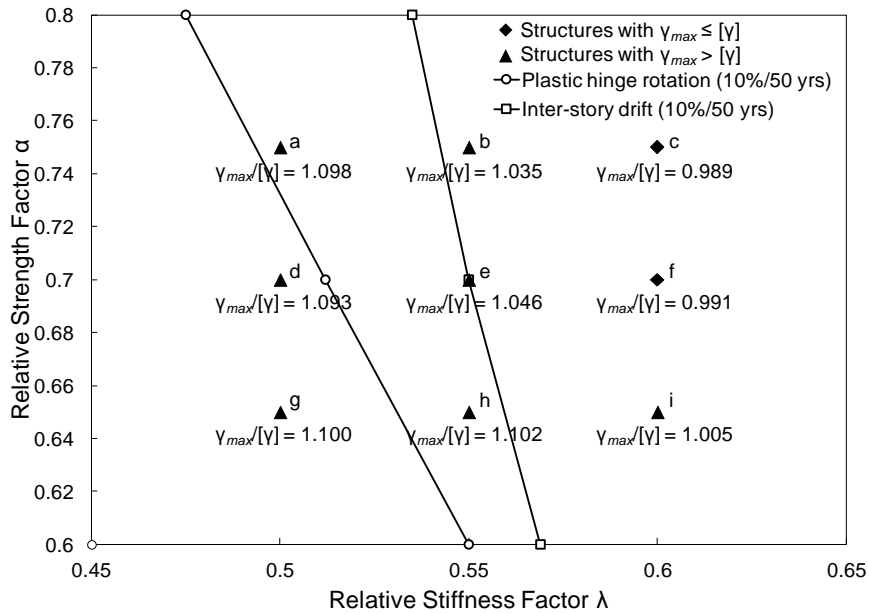


Figure 3.18 Peak inter-story drift ratio of the nine structures under rare earthquake derived from dynamic analyses and the feasible region boundary determined from static analyses.

To further illustrate the continuous tendency in the area determined by eight points, contours of $\gamma_{max}/[\gamma]$ are generated from linear interpolation and shown in Figure 3.19, based on the values of $\gamma_{max}/[\gamma]$ for the structures design with the nine pairs of α and λ shown in Figure 3.18.

The second contour line (in red color) from the right represents $\gamma_{max} = [\gamma]$. The optimal solution

determined from dynamic analyses must be located on this contour line. The tendency of all the contours in Figure 3.19 is continuous especially for the area determined by points b, c, e, f, h, and i.

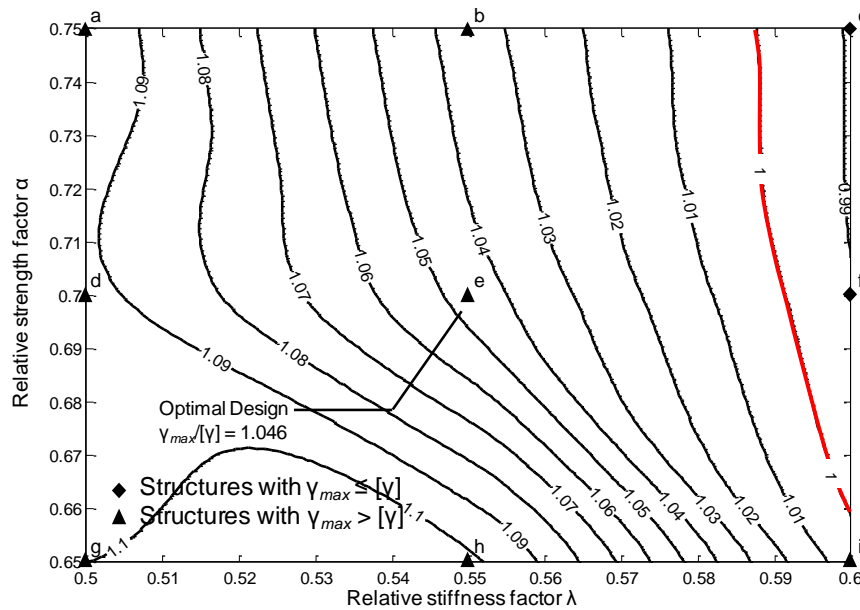


Figure 3.19 Contours of the peak normalized inter-story drift ratio and the design variables of the nine structures

Figure 3.20 shows the total construction cost including the cost of both concrete and reinforcement of nine structures. For the structures with identical λ value, the concrete consumptions are identical, and the reinforcement consumptions increase with the value of α . Due to the increase in section dimension, the required reinforcement area generate identical element flexural strength is reduced. Thus, the reinforcement consumption of the structures with identical α value decreases with the rise of λ . In Figure, 3.20, the construction cost of the optimal design derived from the proposed method is 3% less than the maximum construction cost among

the eight points at point c. However, the construction cost of the optimal design is about 20% less than the initial design derived from the force-based seismic design method.

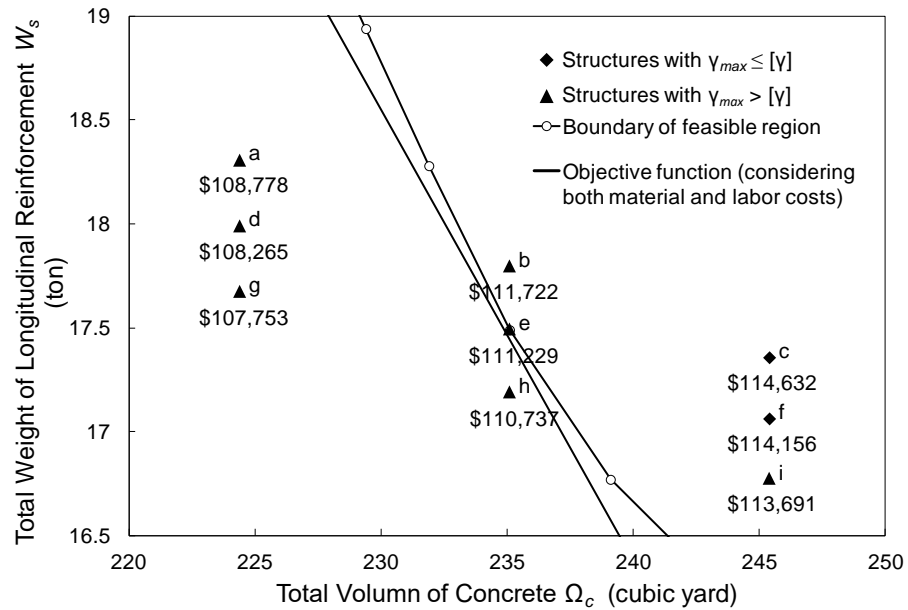


Figure 3.20 Construction cost of the nine structures for verifying the validity of the proposed optimal PBSM method.

CHAPTER 4

RELIABILITY EVALUATION OF PROTOTYPE BUILDING

4.1 Overview of Reliability Evaluation

The prototype structure designed by the conventional force-based seismic design method is conservative. The degree of conservatism is reduced when the prototype structure is optimized by the optimal PBSO method. For the optimal structure, one or more types of deformation are equal to their performance limits. The deformations of this optimal structure and the limits are derived based on the nominal values of external loads, model parameters, and deformation limits. However, large uncertainties exist in these three aspects; thus, the deformations of the optimal structure may be larger than their limits in some extreme conditions. For economic reasons, these extreme conditions are not eliminated. However, the probability of occurrence of these extreme conditions shall be controlled to make sure that the optimal design has sufficient reliability. Accordingly, the reliability evaluation is necessary for the optimal design derived from the proposed optimal PBSO method. Reliability evaluation is also applied to the original design to compare with the evaluation results of the optimal design. Furthermore, reliability evaluations are performed on the other 26 structures with different relative strength factor α and relative stiffness factor λ to observe how these two variables affect the probability of occurrence of the extreme conditions.

The reliability evaluations include three procedures in this study. First, Latin Hypercube

sampling method is used to select the discrete values of the random variables, and combines these discrete model parameters to create 8000 structure model samples for both the optimal and the original structures. Second, 8000 samples are simulated by nonlinear dynamic analysis method for the peak normalized deformation ($\theta/[\theta]$ and $\gamma/[\gamma]$). Third, the outputs of these samples are used to generate the regression lines of peak normalized deformation and fragility function curves. In addition, to analyze how relative strength factor α and relative stiffness factor γ affect the reliability evaluation results, the previous procedures are applied on 28 structures besides the optimal and original structures with seven α levels ($\alpha = 0.4, 0.5, 0.6, 0.7, 0.8, 0.9, \text{ and } 1.0$) and four λ levels ($\lambda = 0.55, 0.7, 0.85, 1.0$). The structure nonperformance contours are generated based on the results of these structures.

4.2 Statistical Properties of Variables

Uncertainty exists in diverse aspects of structural seismic response, and can be derived from five sources (Bulleit, 2008): time (future external loads and structural characteristics affected by time), statistical limits (lack of data for their probabilistic distribution), model limitation (simplifications and assumptions within models), randomness (uncertainty in structural properties), and human error (mistakes in design and construction). These uncertainties can be classified into three types (Ayyub and McCuen, 2016): stochastic, epistemic and numerical uncertainty. Stochastic uncertainty reflects the unpredictability of natural hazard, such as seismic and snow loads; thus, this type of uncertainty is unavoidable. Epistemic uncertainty is caused by

the lack of statistical data or knowledge of understanding. Numerical uncertainty exists when a mechanical model is adopted to simulate actual buildings, such as when the finite-element method is used.

Large uncertainties exist in the external loading, structure model for simulation and performance limits. In this study, the uncertainties in seven aspects (dead load, live load, seismic effect, flexural strength and effective stiffness of elements, and the limits of inter-story drift and plastic hinge rotation) are considered. In addition, the uncertainty in some other aspects, such as structural damping ratio, site condition type, and deterioration of strength and stiffness of plastic hinge model, also influence the structural nonlinear deformation. However, they are not considered in this study due to the lack of statistical data. The statistical properties of seven types of uncertainties are shown in Table 4.1. In this table, \bar{x} and x_n are the mean value and the nominal value of parameter x ; λ is the bias factor, which is the ratio between the mean value and the nominal value of one type of parameter x ; V_s is the coefficient of variation, which is the ratio between the standard deviation (σ_x) and mean value of parameter x . V_s is a standardized measure of dispersion of a probability distribution.

Table 4.1 Summary of statistical properties of input variables

Random Variable Type	Mean (\bar{x})	Bias Factor ($\lambda = \frac{\bar{x}}{x_n}$)	Coefficient of Variation ($V_x = \frac{\sigma_x}{\bar{x}}$)	Type of Distribution
Dead load (DL)	–	1.05	0.10	Normal (Ellingwood 1980)
Live load (LL)	–	1.00	0.25	Type I (Gumbel) (Ellingwood 1980)
Flexural Strength (M) (Reinforced Concrete, Grade 60)	–	1.1025	0.11	Normal (Ellingwood 1980)
Inter-story drift limit ($[\gamma]$)	–	1.00	0.1	Lognormal (SEAOC 1995)
Plastic hinge rotation limit ($[\theta]$)	–	1.00	0.1	Beta (SEAOC 1995)
Seismic effect (PGA)	0.1156	–	5.48	Lognormal (Abrahamson et al. 2014)
Ratio between effective stiffness and gross stiffness (EI_{eff} / EI_g)	0.403	–	0.643	Lognormal (Elwood et al. 2007) Fitting based on Matlab

4.2.1 Statistical properties of external loads

External loading can be divided into two groups. The first group includes dead load (DL) and live load (LL) applied vertically as constant loading in this study. The second group includes seismic load (E) applied horizontally as period loading. The uncertainties of DL and LL are simulated by applying random value generated based on their statistical properties on different beams and joints. On the other hand, the uncertainty of earthquake exists in peak ground acceleration (PGA), duration, and frequent content of earthquakes. Many studies (Abrahamson et al., 2014; Boore et al., 2014; Campbell and Bozorgnia, 2014; Chiou and Youngs, 2014; and Idriss,

2014) focused on the statistical properties of PGA, but none for duration or frequent content. Therefore, the uncertainty of PGA is simulated by the statistical parameters listed in Table 4.1, and the uncertainty of duration and frequency content is simulated by 10 earthquake recorders listed in Table 3.5.

4.2.1.1 Dead load and live load

As suggested by Ellingwood (1980), probability distribution types of DL and LL are assumed to be normal and Type I (Gumbel), respectively. Classic probability density function (PDF) curves for these two types of distribution are shown in Figure 4.1. These probability distribution types are widely used in many studies (Gaxiola et al., 2017; Kogut and Chou, 2004; and Ellingwood, 2003). The corresponding bias factor and coefficient of variation listed in Table 4.1 are based on a 50-years reference period. For the nominal live load, L_n , Ellingwood (1980) suggested that it can be calculated by Equation 4.1 based on A58 standard (1980). The nominal value calculated by this equation is statistical equal to the 50-year mean value, L . Therefore the bias factor λ (the ratio between the mean value to the nominal value) for live load is assumed as 1 in this study.

$$L_n = \left(0.25 + \frac{15}{\sqrt{A_I}} \right) L_0 \quad \text{Equation 4.1}$$

where A_I is influence area and L_0 is basic unreduced live load based on A58 (1980).

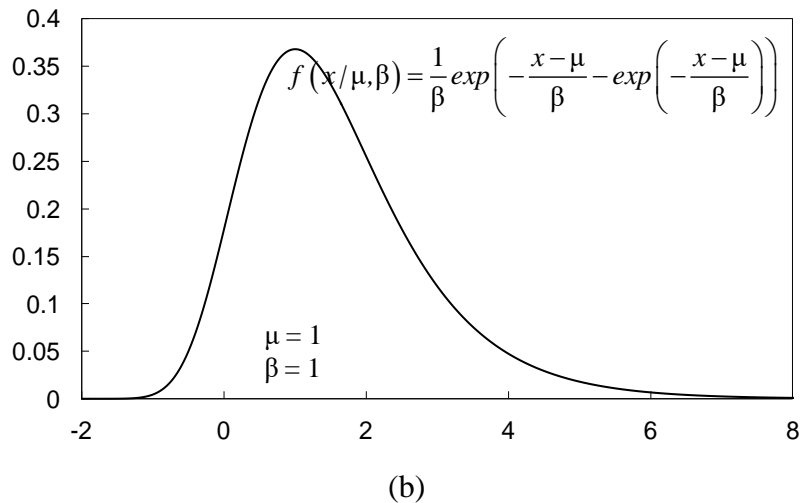
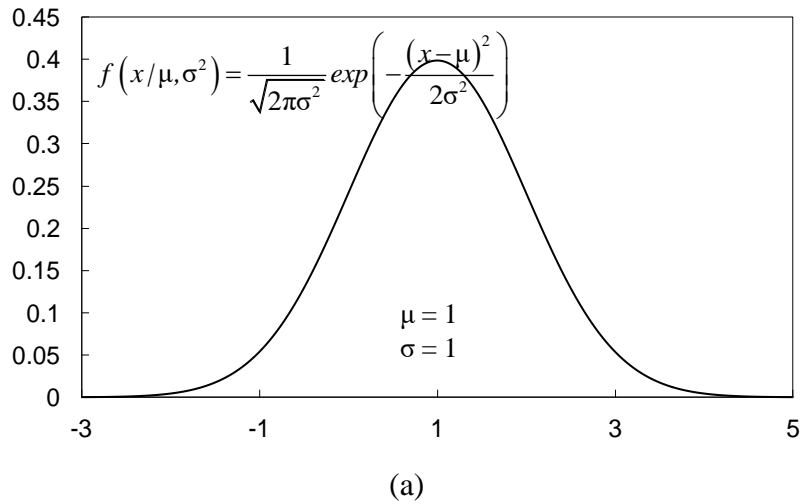


Figure 4.1 Probability density function (PDF) curve of: (a) normal distribution; and (b) Type I distribution

The nominal value of DL includes the self-weight of all components (beams, columns and slabs), and superimposed dead load (roofing, curtain wall, and mechanical). The nominal value of LL includes the weight of building users, furniture and other moveable equipment.

4.2.1.2 Seismic load

The seismic load applied on a RC moment frame structure is influenced mainly by the intensity measurement, duration, and frequency content of an earthquake. Many factors can

describe the intensity measurement of earthquake, such as peak ground acceleration (PGA) or peak ground velocity. PGA is the most widely used, and conveniently applied in the dynamic structural analysis. The statistical properties of PGA at a specific location can be determined through different types of attenuation formulations, which correlate ground motion magnitude to the distance away from fault rupture. These formulations were established in 2008 and updated in 2014 by five separate research teams: Abrahamson et al. (2014), Boore et al. (2014), Campbell and Bozorgnia (2014), Chiou and Youngs (2014), and Idriss (2014). In this study, the statistical properties of PGA are determined by the next-generation attenuation proposed by Abrahamson et al. (2014), and listed in Table 4.1. This attenuation formulation was established based on 2754 ground motion records from 135 earthquakes, and considered the effect of fault type and geometry, hanging wall effect, site type and other factors. The probability distribution type of PGA is normally assumed as lognormal (Yazdani et al., 2016; Khatibinia et al., 2013; and Huyse et al., 2010). Classic PDF curve of lognormal distribution is shown in Figure 4.2.

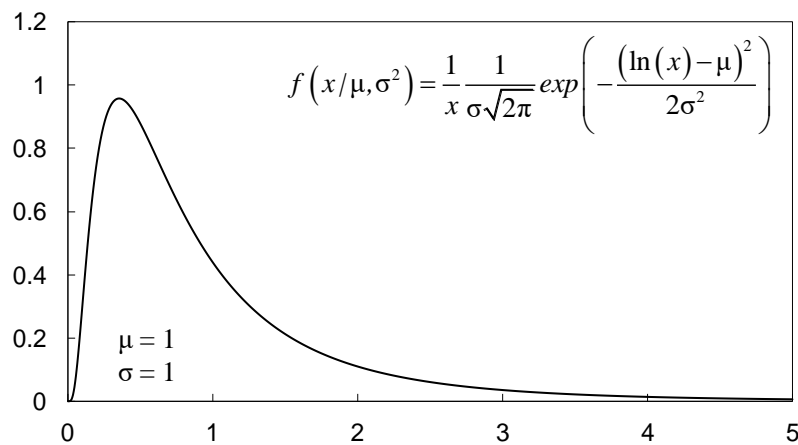


Figure 4.2 Probability density function curve of lognormal distribution

In addition to the intensity measurement quantified by PGA, earthquake duration and frequency content can also influence the structural seismic response. Duration is related to total input energy of earthquake, and frequency content of earthquake determines the magnitude of the resonance effect on the structure. Based on Fourier transform, chaotic and random earthquake wave can be decomposed into a series of sine waves with different phase, frequency and amplitude. Resonance occurs when the structure free vibration frequency is equal to the frequency of a sine wave. The resonance magnitude depends on the amplitude of this wave. In this study, the uncertainty of earthquake duration and frequency content is covered by the different durations, fault types, and occurrence locations of the ten selected earthquakes listed in Table 3.5.

4.2.2 Statistical properties of member resistance

4.2.2.1 Elemental flexural strength

The structural resistance against gravity and seismic loads is affected by component effective stiffness (K) and flexural strength (M_u). These properties influence structural vibration period and load redistribution within the structure during external loading. Therefore, the uncertainties of K and M_u are two major considerations for member resistance in seismic reliability assessment. The statistical properties of these two variables listed in Table 4.1 cover both material and construction uncertainties.

According to Ellingwood (1980), the probability distribution of M_u is assumed to have a normal distribution. The bias factor of M_u of reinforcement concrete component with grade 60

reinforcement was assumed to be 1.05 based on static loading experiments. However, the strength of concrete and reinforcement tends to increase by 5% due to a high loading rate under earthquakes. Therefore, in the dynamic analysis, the bias factor of M_u is also increased by 5% so that it is equal to 1.1025. The nominal value of M_u is determined by the seismic design of RC moment frame structure.

4.2.2.2 Elemental effective stiffness

Due to concrete cracking and bar slip, the K of a RC component under seismic loads is less than that evaluated based on gross section. In addition, shear deformation is found to occupy 15% of total component deformation (Elwood and Eberhard, 2009; and Kenneth et al. 2009). Therefore, total effective displacement of RC component should include the deformations caused by flexure, longitudinal bar bond slip, and shear deformation. K is the reciprocal of total effective displacement under unit load.

No study has ever suggest the distribution type, mean value or standard deviation of K . Nevertheless, Elwood and Eberhard (2006) collected 221 experiment results of the ratio between the effective flexural stiffness, EI_{eff} , and the gross bending stiffness, EI_g , of rectangular column, as shown in Figure 4.3.

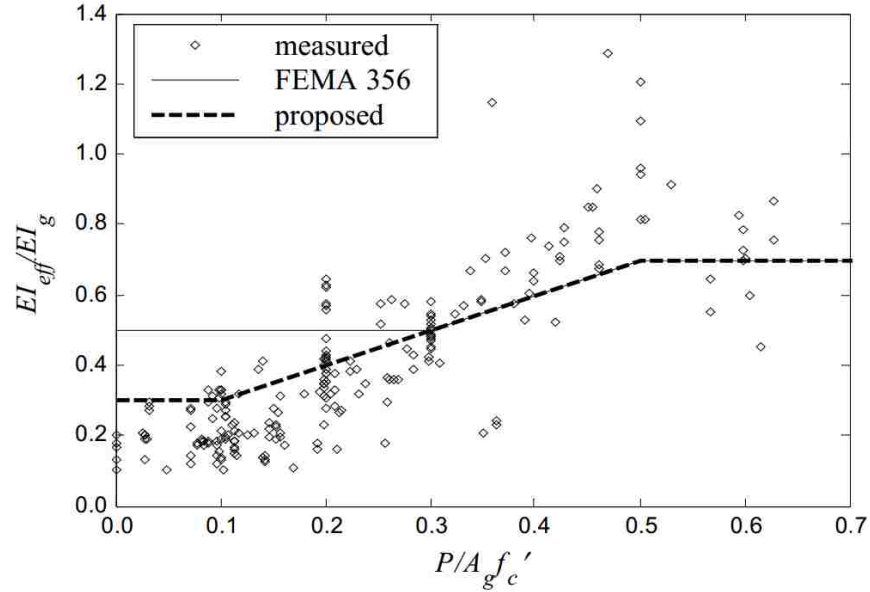


Figure 4.3 Measured ratio between effective stiffness and gross bending stiffness (Elwood et al., 2007)

Although only the flexural experiments of column are summarized in these results, beam can be taken as a flexural component without axial load. Therefore, in this study, the K of beams and columns are assumed to have statistical properties identical to those of the experimental data given by Elwood and Eberhard (2009). However, in these papers, neither the distribution type or the statistical properties of the ratio between effective stiffness and gross stiffness is not given. Therefore, Matlab distribution fitting toolbox is used in this study to obtain a suitable probability distribution type and corresponding statistical properties of K . First, 221 discrete value of the ratio between effective stiffness and gross stiffness are distributed into twelve frequency histogram columns with an interval of 0.1 stiffness ratio, as shown in Figure 4.4(a). Then, eighteen distribution types in Matlab toolbox are used to fit this frequency histogram of stiffness data without excluding the extreme value. Based on the fitting results, Lognormal and

Birnbaum-Saunders distributions are suitable to the discrete data of the stiffness ratio with log likelihood factor 41.51 and 43.89. A higher log likelihood factor expresses a better fitting between the PDF or CDF curve and the frequency distribution histogram. At last, Lognormal distribution is chosen as the probability distribution type of the stiffness ratio in this study, because it is more widely used than Birnbaum-Saunders distribution. The corresponding

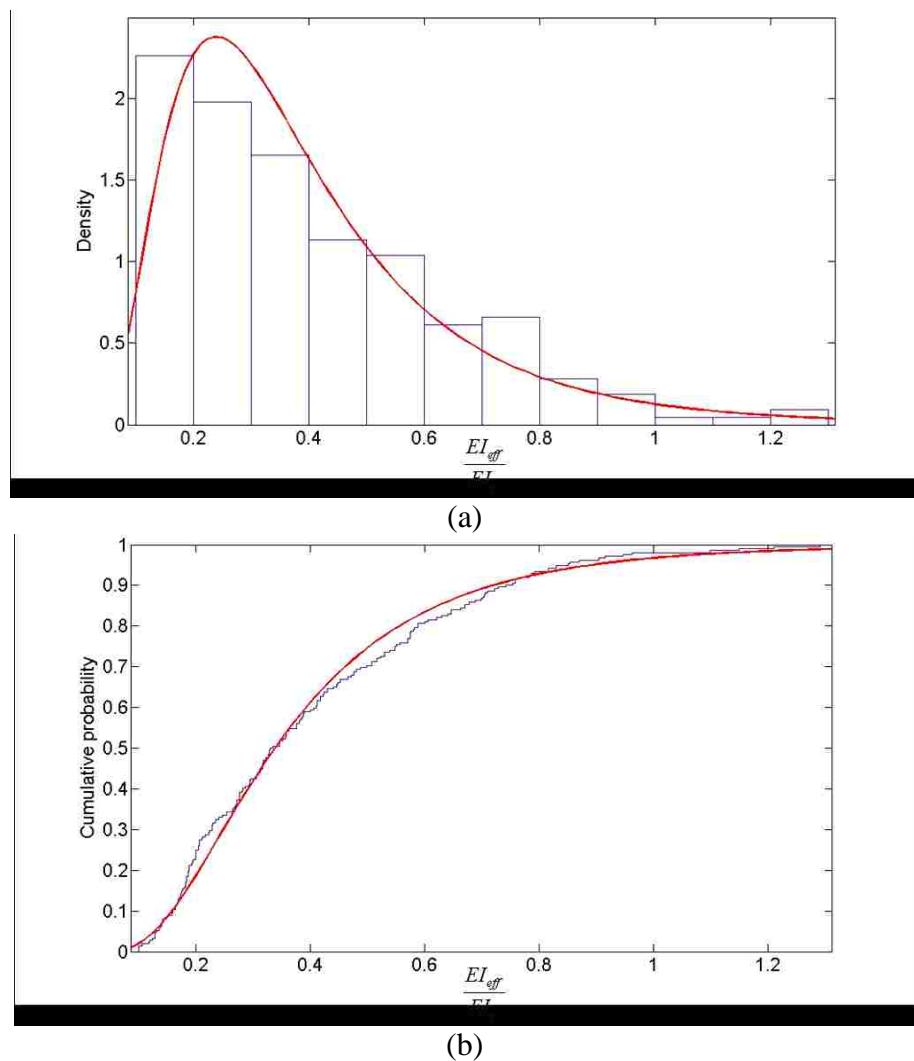


Figure 4.4 Distribution fitting of discrete stiffness ratio (a) frequency histogram of discrete stiffness ratio and PDF of fitting lognormal distribution; (b) cumulate frequency histogram of stiffness ratio and CDF of fitting lognormal distribution

mean value and COV are listed in Table 4.1. The cumulative distribution function curve can closely match the discrete data, as shown in Figure 4.4(b).

In Figure 4.4(a), 221 discrete experiment data in Elwood and Eberhard (2009) are distributed into twelve frequency histogram columns. Eighteen distribution types in Matlab toolbox are used to fit this frequency histogram of stiffness data without excluding the extreme value. Based on the fitting results, Lognormal and Birnbaum-Saunders distributions are suitable to the discrete data of the stiffness ratio with log likelihood factor 41.51 and 43.89. A higher log likelihood factor expresses a better fitting between the PDF or CDF curve and the frequency distribution histogram. As the most widely used distribution type, Lognormal distribution is chosen as the probability distribution type of the stiffness ratio in this study. The corresponding mean value and COV are listed in Table 4.1. The cumulative distribution function curve can closely match the discrete data, as shown in Figure 4.4(b).

4.2.3 Statistical properties of deformation limits

Inter-story drift and plastic hinge rotation are two major deformation measurements of the seismic performance assessment of RC moment frame structure. However, no sufficient information is provided in ASCE 41-13 (2014), the standard used in this study for performance-based seismic evaluation, to select appropriate bias factor or COV for allowable values of inter-story drift $[\gamma]$ and plastic hinge rotation $[\theta]$. In addition to ASCE 41-13 (2014), SEAOC (1995) can be used to assess seismic performance. In this document, the statistical properties of inter-story drift, local damage index and global damage index are provided. The

local damage index, considering both component section rotation and energy dissipation effect, is defined by Park and Ang (1985) and Moller et al. (2009), as

$$LDI = \frac{\phi_m - \phi_y}{\phi_u - \phi_y} + 0.25 \frac{\int dE}{M_y \phi_u} \quad \text{Equation 4.2}$$

where ϕ_m is the maximum cross-sectional rotation; ϕ_u is the ultimate rotation during a monotonic load; ϕ_y is the recoverable rotation during unloading; $\int dE$ is the energy dissipation caused by hysteretic deformation; and M_y is section yield moment. In Equation 4.2, both section rotation part and energy dissipation part are impact mainly by plastic hinge rotation; thus, it is rational to assume $[\theta]$ and local damage index have identical statistical properties. In this study, $[\theta]$ is assumed to have Beta distribution, which is the distribution type of local damage index in SEAOC (1995). A classic Beta distribution is drawn in Figure 4.5. The value of $[\gamma]$ and $[\theta]$ in ASCE41-13 are used as the nominal value, and the bias factor is assumed to be 1.0.

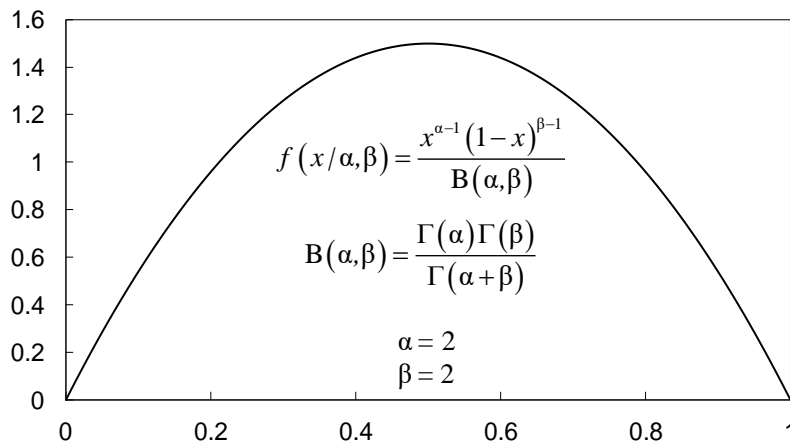


Figure 4.5 Probability density function curve of Beta distribution

4.3 Sampling Methods

Sampling method is a survey methodology used to predict statistical properties of whole sample population by repeatedly testing a finite number of samples within this population. For this purpose, simulations by performing nonlinear dynamic structural analyses of the optimized structure with seven input parameters are conducted in this study.

4.3.1 Monte Carlo sampling method

Monte Carlo sampling method is a conventional sampling method, which has been used so solve statistical problems in many fields. Monte Carlo sampling method repeats random sampling of input variables and experimental or numerical simulation to obtain a probabilistic distribution of the results. Monte Carlo sampling method is reliable; however, the difficulty of using this method in practice is its extremely high experimental or computational cost for complex system or small probability of occurrence. In a structural seismic failure simulation, complex nonlinear dynamic analysis is applied to obtain the nonlinear deformation of the structure considering the uncertainties within seismic records. In addition, the allowable failure probability of the structure under the very rare earthquake is as small as 0.001 (Paulay and Priestley, 1992). Therefore, the required sampling number is enormous and even impracticable. Soong and Grigoriu (1993) proposed a method to estimate the approximate number required for using Monte Carlo sampling method, as shown in Equation 4.3.

$$N = \frac{1-P}{V^2 \times P} = \frac{1-10^{-3}}{0.05^2 \times 10^{-3}} = 399600 \quad \text{Equation 4.3}$$

where N is the required number of samples; P is the estimated failure probability; and V is the COV of sample population. Based on Equation 4.3, the required sampling number of Monte Carlo sampling method for the problem with a 0.001 failure probability and 5% COV is 399600. Although controversy exists about the exact required number of samples in the Monte Carlo sampling method (Shooman, 1968; Soong and Grigoriu 1993), it is definitely an extreme large number, and difficult to be applied to the failure probability analysis of RC frames.

4.3.2 Latin Hypercube sampling method

An alternative approach is Latin Hypercube sampling method proposed by Iman and Conover (1980). It is a near-random sampling method to estimate the probability properties of the sample population. The Latin Hypercube sampling method requires smaller sampling number than Monte Carlo sampling method, and has been proved to be effective and reliable in evaluating the structural failure probabilities under seismic or wind load effect (Yazdani et al., 2016; Li and Hu, 2014; and Khatibinia et al., 2013).

4.3.2.1 Procedure of Latin Hypercube sampling method

To select near-random input variables for each sample by Latin Hypercube sampling method, two steps are used to establish a $N \times K$ input variable matrix with a total sample number of N and a total number of input variable types of K shown in Figure 4.6(d). First, for every type of input variable, such as dead load, N discrete representative values are selected according to the

cumulative distribution function of this variable, as shown in Figure 4.6(a). Second, the sequential order of the selected value of each variable is adjusted according to the table of random permutation of rank number, as shown in Figure 4.6(c). This procedure is repeated for every input variable, and the $N \times K$ input variable matrix shown in Figure 4.6(d) is established. The values of the input variables of the i^{th} sample are the data on the i^{th} row in the $N \times K$ input variable matrix, and all the discrete representative values of the j^{th} input variable are the data on the j^{th} column in this matrix.

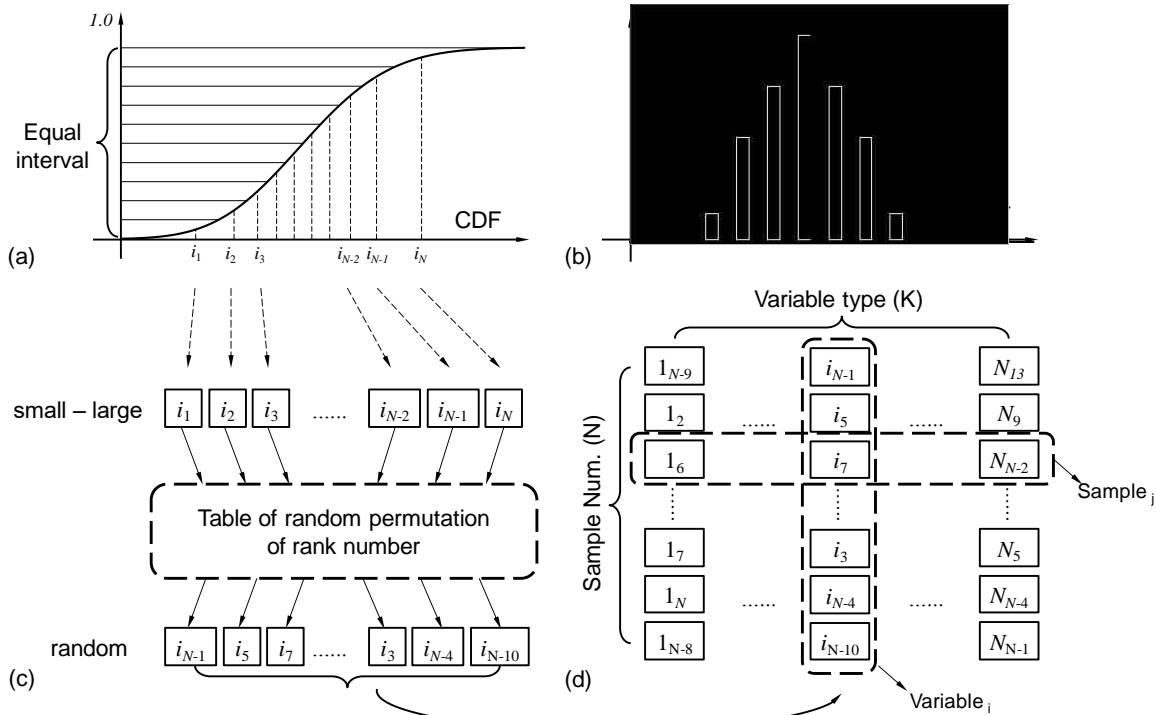


Figure 4.6 Procedure of Latin Hypercube sampling method: (a) representative values selection from CDF of one variable; (b) frequency histogram and PDF of selected representative values; (c) order rearranging of representative values of one variable; and (d) input data matrix of all variables and samples

To obtain N discrete representative values of a variable in the first step, cumulative distribution function curve of this variable is separated into N intervals with identical difference in probability, as shown in Figure 4.6(a). The frequency histograms of these selected values shown in Figure 4.6(b) still statistically obey the probability density function of this variable shown in Figure 4.6(a). The representative value of each interval is the variable value with a centroid probability of the corresponding interval defined in Equation 4.4. Currently, all selected values are ordered from small to large. In the second step, the small-to-large ordered representative values are rearranged according to the table of random permutation of rank number into a random order, as shown in Figure 4.6(c). The rank number of this variable is an arrange of integers $[1, 2, \dots, N]^T$ coupling to the selected representative values in a small-to-large order. In the table of random permutation of rank number, this rank number is rearranged randomly to reflect the uncertainty in nature. These two steps are repeated for K variables, and a $N \times K$ matrix is established, as shown in Figure 4.6(d). The data on the i^{th} column of this matrix are the representative values in random order of variable i , and the data on the j^{th} row are the input values of variables of sample j . Eventually, the data of this matrix are inputted into N models for numerical or experimental simulations.

$$F_K^{-1}\left(\frac{m_{nK} - 0.5}{N}\right) \quad \text{Equation 4.4}$$

where F_K^{-1} is inverse cumulative distribution function of variable K , and m_{nK} is rank number of

the n^{th} interval of variable K .

4.3.2.2 Elimination of correlation between variables

Based on Figure 4.6, for each type of input variable, an unique table of random permutation of rank number with N random values exists; thus for totally K types of input variables, all the tables of random permutation of rank number can be composed of a $N \times K$ matrix. This matrix reflects the uncertainty of each variable and the independency among the variables. This independency can be described as a linear relationship between any two types of input variables, as shown in Figure 4.7. In Figure 4.7(a), two variables have obviously positive linear correlation, that is, sample values of one type of variable tend to increase with the other type of variable. However, two variables in Figure 4.7(b) are comparatively independent. Because the table of random permutation of rank number used in Latin Hypercube Sampling method is generated randomly, the linear correlation between two variables cannot be completely avoided.

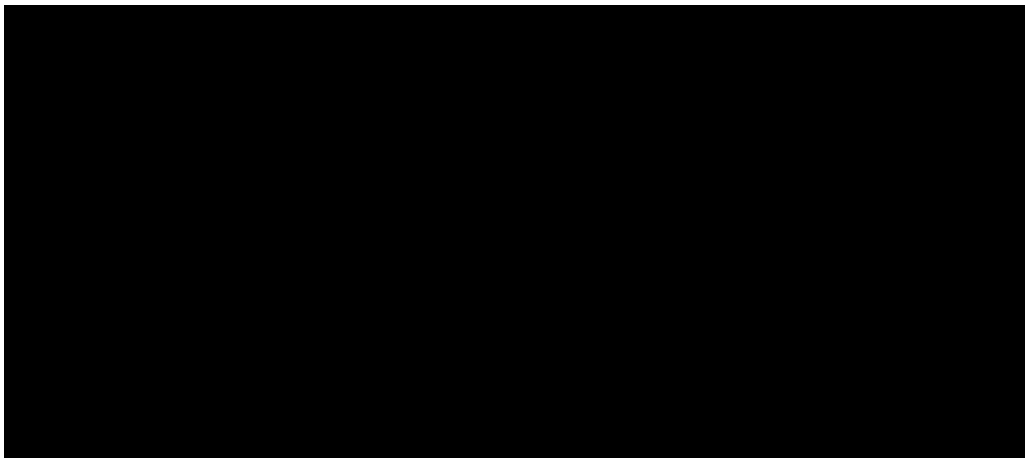


Figure 4.7 Relationship between two variables: (a) correlation and (b) independent

A modified Latin Hypercube sampling method using specifically modified tables of random permutations of ranked number and Spearman coefficient is proposed by Yang (2006) to eliminate this linear correlation. First, a measurement of the correlation level called Spearman rank-order correlation coefficient (Spearman coefficient) is proposed by Hettmansperger and McKean (1978) and defined as follows. The N representative values of two variables, P and Q , are selected and arranged from small to large with same rank numbers $[1, 2, \dots, n]^T$. To reflect uncertainty of the nature, the order of Q_i is changed according to one table of random permutation of rank number, that is, the rank number of Q_i becomes to $[R_1, R_2, \dots, R_n]^T \neq [1, 2, \dots, n]^T$, where R_i is corresponding to the out-of-order rank number of Q_i . The Spearman coefficient r_s between variables P and Q can be defined by Equation 4.5. Spearman coefficient is always located between -1 and $+1$, which reflect the negative and positive linear correlations exist between two variables. Thus the more Spearman coefficient close to zero, the more two variables get independent.

$$r_s = \frac{\sum_{i=1}^n \left(i - \frac{n+1}{2}\right) \left(R_i - \frac{n+1}{2}\right)}{\sqrt{\sum_{i=1}^n \left(i - \frac{n+1}{2}\right)^2 \sum_{i=1}^n \left(R_i - \frac{n+1}{2}\right)^2}} \quad \text{Equation 4.5}$$

Second, a critical coefficient or threshold should be determined to check whether the correlation between two variables is higher than necessary. This is because an absolutely independent relationship between two variables is hard to get due to the limited sampling number.

Such an independent relationship is also unnecessary due to its negligible effect on the statistical probability. Accordingly, threshold Spearman coefficient r_s^* is proposed, and the rank number of two variables is modified if this threshold is exceeded.

If the Spearman coefficient between two variables is higher than r_s^* , the following process can be performed to reduce the undesired correlation. For a system with K variables and, N sample numbers, the $N \times K$ table of random permutations of ranked number is defined as R , in which the data in column is the random rank number of one of the K variables. A $K \times K$ Spearman coefficient matrix, T , can be established according to Equation 4.5, and T_{ij} represents the Spearman coefficient between the i^{th} and j^{th} variable. Obviously, T is a symmetrical matrix, and always assumed as positive. T satisfies Equations 4.6 to 4.8. A lower triangular matrix, S , is used to establish the modified table of random permutations of ranked number, R_B . Cholesky factorization scheme can be used to solve the problem with lower triangular matrix.

$$S \times T \times S^T = 1 \quad \text{Equation 4.6}$$

$$S = Q^{-1} \quad \text{Equation 4.7}$$

$$T = Q \times Q^T \quad \text{Equation 4.8}$$

where Q is a lower triangular matrix. A modified table of random permutations of ranked number, R_B , can be obtained by Equation 4.9.

$$R_B = R \times S^T \quad \text{Equation 4.9}$$

The procedure described above is repeated until no element in T is larger than r_s^* , that is, matrix T gets close to unit matrix. In the current step, this modified table of random permutations of ranked number can be used to produce uncorrelated representative values of variables. It has been proved that this modified Latin Hypercube sampling method can significantly reduce the output variance of probability analysis (Yang, 2006). One example of applying modified Latin Hypercube sampling method is illustrated in Figure 4.8, through eliminating the correlation between inter-story drift limit and PGA of input earthquake acceleration.

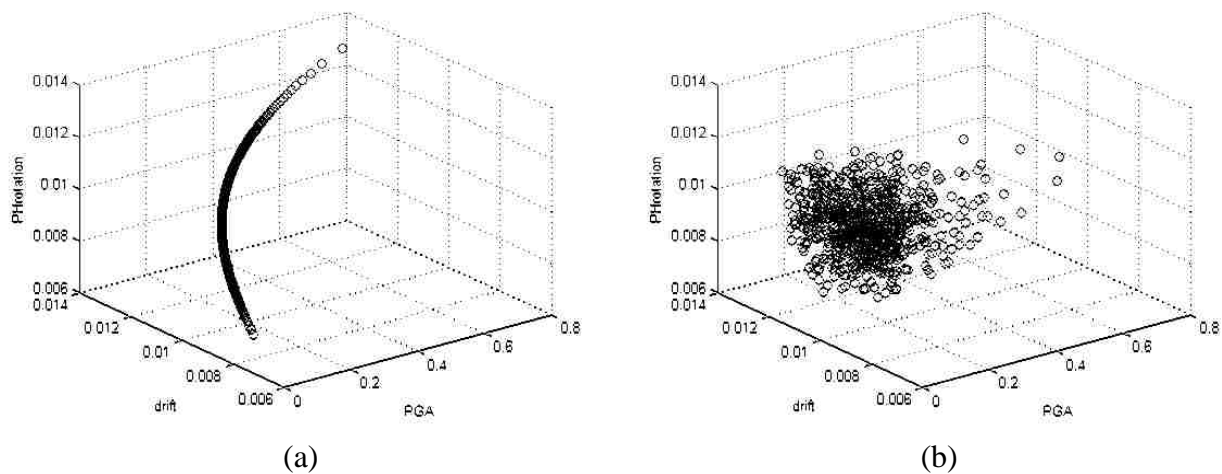


Figure 4.8 Illustration of the relationship between two input variables: (a) correlated relationship (b) independent relationship

4.4 Probability-based Nonperformance Probability

For each structure with determined relative strength and stiffness factors, 8000 samples are created based on the discrete variables for seven uncertainties selected and combined by Latin Hypercube sampling method. The deformation of these 8000 samples are estimated by

nonlinear dynamic analysis method described in Section 3.2. The examined output data of the dynamic analysis are two types of peak normalized deformation in terms of plastic hinge rotation and inter-story drift: peak $\theta/[\theta]$ and peak $\gamma/[\gamma]$.

To determine the reliability of a structure, the probability of nonperformance of this structure is evaluated by its limits. Nonperformance due to a certain type of deformation is defined as the peak normalized value of this type of deformation is larger than 1. In this study, three types of nonperformance are defined: nonperformance due to plastic hinge (peak $\theta/[\theta] > 1$), nonperformance due to inter-story drift (peak $\gamma/[\gamma] > 1$), and nonperformance due to either plastic hinge or inter-story drift (either peak $\theta/[\theta] > 1$ or peak $\gamma/[\gamma] > 1$). Because the values of both $[\theta]$ and $[\gamma]$ are different for diverse performance levels (CP, LS, and IO performance levels), each type of nonperformance can be measured by the limit for different performance levels. To define a nonperformance of a structure, both nonperformance type and performance level shall be indicated, such as nonperformance due to inter-story drift for LS performance level. For a structure, the nonperformance due to a certain type of deformation for a performance level indicates that this type of deformation of the structure cannot satisfy the deformation limit of this performance level.

For a structure, the probability of nonperformance due to a certain type of normalized deformation for a performance level, P_{fE} , is the ratio between the number of the samples with peak normalized deformation larger than 1 and 8000 samples. This nonperformance probability is for 50-year duration. Because the nonperformance limit suggested by Paulay and Priestley

(1992) listed in Table 1.3 is for 1-year duration, the annual probability of nonperformance due to a certain type of deformation for a performance level, $P_{f,a}$, can be calculated based on by Equation 4.10.

$$P_{f,a} = 1 - \exp(-vP_{fE}) \quad \text{Equation 4.10}$$

where v is the mean occurrence rate of the earthquakes, which is normally assumed as $v = 0.2$ for a Poisson process (Khatibinia et al., 2013; Moller et al., 2015).

4.5 Fragility Curve Generation

Fragility function indicates the relationship between the probability of nonperformance and a intensity measure of ground motion, which can be quantified as the peak ground acceleration (PGA) (Baker, 2015). In this study, the fragility functions of the optimal and original structures are generated by the method suggested by Baker (2015) based on the normalized deformations of 8000 samples. These samples include 800 PGA levels, and 10 types of earthquake records for each PGA level. First, the nonperformance probability for each PGA, which is the ratio between the number of nonperformance samples and 10, is obtained. Then, the median and standard deviation of the nonperformance probability for all PGA are estimated by maximum likelihood method. Based on the estimated median, $\tilde{\mu}$, and estimated standard deviation of $\ln(\text{PGA})$, $\tilde{\sigma}$, a lognormal cumulative distribution function is typically used to create the fragility function based on Equation 4.11.

$$P(IM = x) = \Phi\left(\frac{\ln(x/\tilde{\mu})}{\tilde{\sigma}}\right) \quad \text{Equation 4.11}$$

where $\Phi()$ is the standard normal cumulative distribution function. The estimated median and standard deviation instead of the actual ones are used here, because these parameters are derived from only the samples, which is part of the population.

4.6 Results and Discussion

4.6.1 Normalized deformation

For the optimal and original structures, the peak normalized deformation (peak $\theta/[\theta]$ and peak $\gamma/[\gamma]$) of 8000 samples are obtained by nonlinear dynamic analyses. The larger peak normalized deformations between peak $\theta/[\theta]$ and peak $\gamma/[\gamma]$ of 8000 samples are drawn in Figure 4.9. The single type of peak normalized deformation (peak $\theta/[\theta]$ or peak $\gamma/[\gamma]$) of 8000 samples are drawn in Figures 4.10 and 4.11, respectively. In these figures, regression analyses are performed to obtain a mean value line of peak normalized deformation (solid line) as a function of peak ground acceleration. The functions of these lines are defined as $y = a_1x + b_1$ for the larger peak normalized deformation between peak $\theta/[\theta]$ and peak $\gamma/[\gamma]$, $y = a_\theta x + b_\theta$ for peak $\theta/[\theta]$, and $y = a_\gamma x + b_\gamma$ for peak $\gamma/[\gamma]$. In addition, the 95% confidence band are drawn as the dash lines in each figure.

Based on the slope a of the regression line, the probability of different types of nonperformance can be estimated. If the nonperformance probability when either $\theta/[\theta] > 1$ or

$\gamma/[\gamma] > 1$ is define as 100%, then the probability when both $\theta/[\theta] > 1$ and $\gamma/[\gamma] > 1$ can be calculated by $a_2 = (a_\theta + a_\gamma - a_1)/a_1$. The probability when $\theta/[\theta] > 1$ but $\gamma/[\gamma] < 1$ can be calculated by $a_\theta/a_1 - a_2$; similarly, when $\gamma/[\gamma] > 1$ but $\theta/[\theta] < 1$, the probability can be calculated by $a_\gamma/a_1 - a_2$. The results of different types of nonperformance are listed in Table 4.2.

Table 4.2 Composition of different types of nonperformance (unit: %)

Performance level	Optimal Structure			Original Structure		
	$\theta/[\theta] > 1$ but $\gamma/[\gamma] < 1$	$\theta/[\theta] < 1$ but $\gamma/[\gamma] > 1$	$\theta/[\theta] > 1$ and $\gamma/[\gamma] > 1$	$\theta/[\theta] > 1$ but $\gamma/[\gamma] < 1$	$\theta/[\theta] < 1$ but $\gamma/[\gamma] > 1$	$\theta/[\theta] > 1$ and $\gamma/[\gamma] > 1$
CP	5.3	27.3	67.3	2.9	37.9	59.2
LS	5.5	27.1	67.4	2.5	38.3	59.2
IO	12.5	17.1	70.4	8.0	27.5	64.5

Based on Table 4.2, the probabilities of different types of nonperformance are similar between CP and LS performance levels. The probability of both $\theta/[\theta] > 1$ and $\gamma/[\gamma] > 1$ is much higher than the other types of nonperformance, while the probability of $\theta/[\theta] > 1$ but $\gamma/[\gamma] < 1$ is much lower than the other types of nonperformance. It can be concluded that (1) the probability of simultaneous appearance of both types of nonperformance ($\theta/[\theta] > 1$ and $\gamma/[\gamma] > 1$) is higher than the probability due to other types of deformation; (2) nonperformance due to plastic hinge hardly appears alone without the nonperformance due to inter-story drift; (3) No matter the type of deformation, the nonperformance probabilities of optimal and original structures are close.

The width of the 95% confidence band w reflects the uncertainty of the normalized deformation. The width is normalized by the slope of the regression line as w/a to compare the

uncertainty of the sample with different magnitudes. The normalized width of the 95% confidence band of three types of failure for both optimal and original structures in different performance levels are listed in Table 4.3. In this table, the higher value reflects higher uncertainty.

Table 4.3 Normalized width of the 95% confidence band (w/a)

Performance level	Optimal Structure			Original Structure		
	peak $\theta/[\theta]$	peak $\gamma/[\gamma]$	max(peak $\theta/[\theta]$ & peak $\gamma/[\gamma]$)	peak $\theta/[\theta]$	peak $\gamma/[\gamma]$	max(peak $\theta/[\theta]$ & peak $\gamma/[\gamma]$)
CP	0.445	0.236	0.243	0.519	0.217	0.221
LS	0.335	0.164	0.165	0.439	0.161	0.163
IO	0.173	0.096	0.094	0.265	0.099	0.102

Based on Table 4.3, the normalized width of the 95% confidence band for peak $\theta/[\theta]$ is much higher than the other two types of deformation. the normalized width of the 95% confidence band for CP performance level is higher than the other two performance levels. It can be concluded that (1) the uncertainty of normalized plastic hinge is much higher than the other two types of deformation; (2) the uncertainty of different peak normalized deformation for CP performance level is higher than the other two types of performance levels.

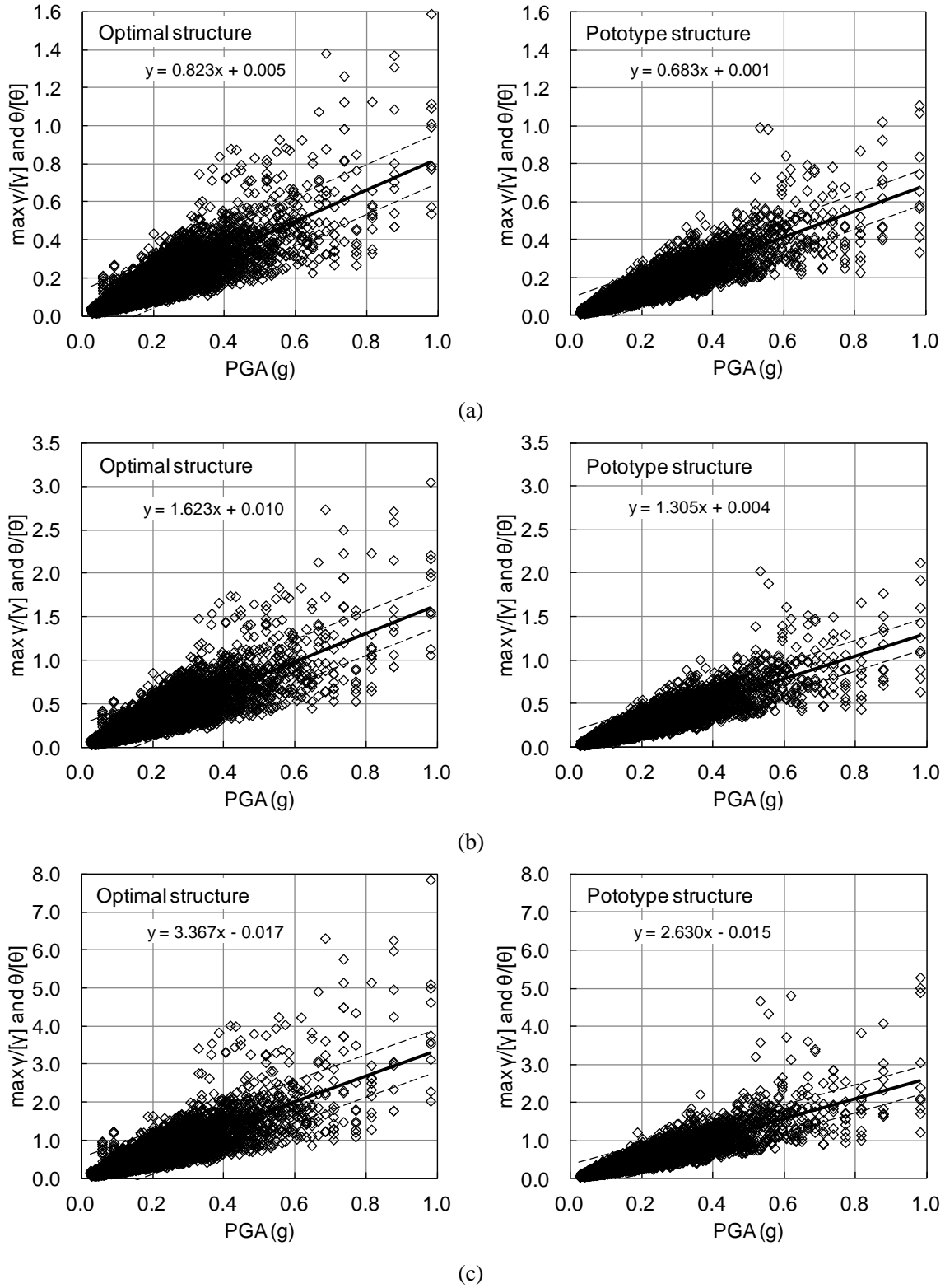


Figure 4.9 Statistical result of the peak normalized plastic deformations (maximum value of $\gamma/[\gamma]$ and $\theta/[\theta]$) of the optimal and original design in various performance levels: (a) collapse prevention; (b) life safety; and (c) immediate occupancy

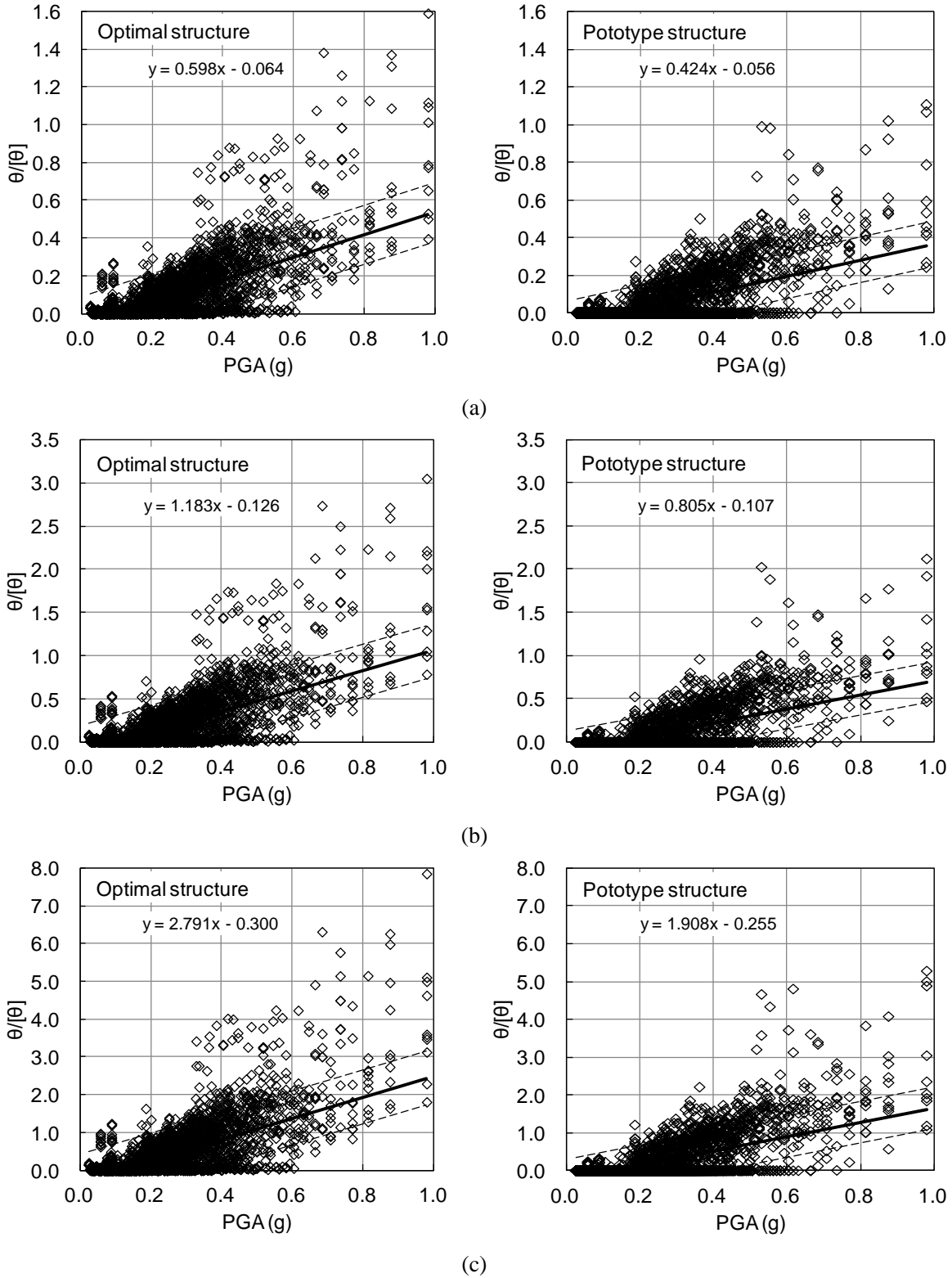


Figure 4.10 Statistical result of the peak normalized plastic deformations (peak $\theta/[\theta]$) of the optimal and original design in various performance levels: (a) collapse prevention; (b) life safety; and (c) immediate occupancy

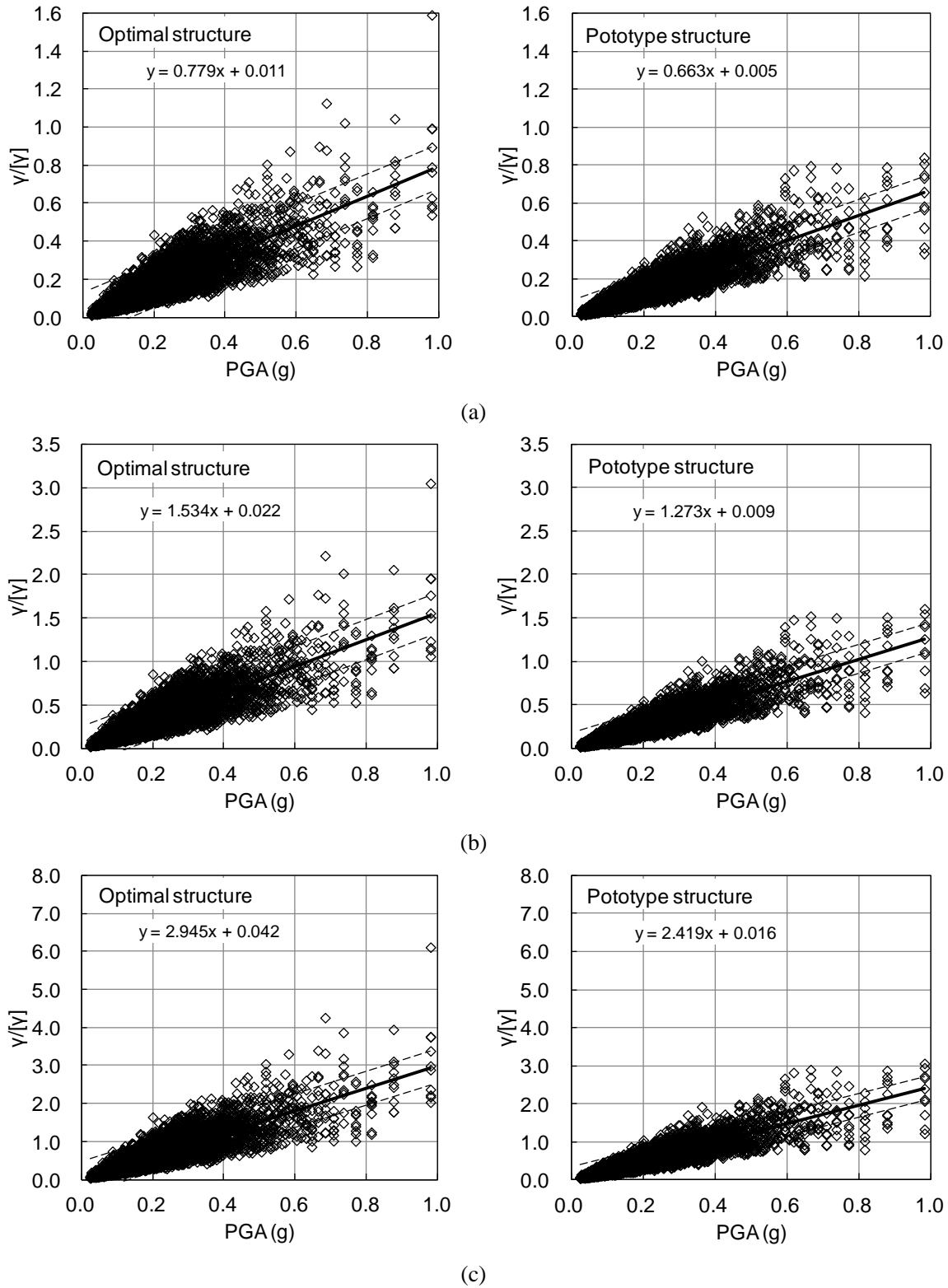


Figure 4.11 Statistical result of the peak normalized plastic deformations (peak $\gamma/[\gamma]$) of the optimal and original design in various performance levels: (a) collapse prevention; (b) life safety; and (c) immediate occupancy

4.6.2 Nonperformance probability

For the optimal and original structure, the probabilities of nonperformance due to plastic hinge rotation, inter-story drift, and either plastic hinge rotation or inter-story drift for three performance levels are shown in Table 4.4. In addition, the allowable nonperformance probabilities of different performance levels $[P_{fE}]$ suggested by Paulay and Priestley (1992) are also listed in this table.

Table 4.4 Probabilities of nonperformance due to different types deformation of the optimal and original structures

Performance level	$[P_{fE}]$	Optimal Structure			Original Structure		
		$\theta/[\theta] > 1$	$\gamma/[\gamma] > 1$	either $\theta/[\theta] > 1$ or $\gamma/[\gamma] > 1$	$\theta/[\theta] > 1$	$\gamma/[\gamma] > 1$	either $\theta/[\theta] > 1$ or $\gamma/[\gamma] > 1$
IO	0.100	0.0635	0.1435	0.1464	0.0395	0.0745	0.0770
LS	0.010	0.0095	0.0160	0.0180	0.0031	0.0064	0.0069
CP	0.001	0.0015	0.0005	0.0015	0.0004	0.0000	0.0004

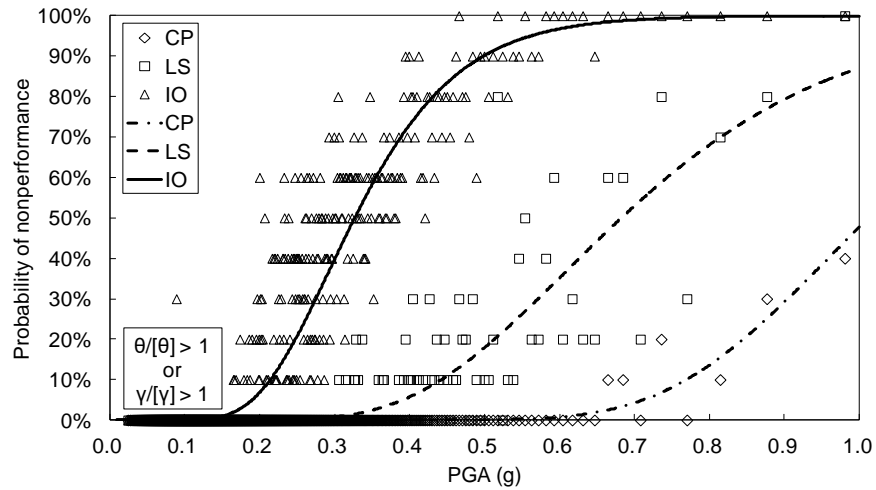
Based on Table 4.4, for the original structure, the probabilities of nonperformance due to all three types of deformation for all three performance levels satisfy the probability limits suggested by Paulay and Priestley (1992). For the optimal structure, the probabilities of nonperformance due to plastic hinge for all three performance satisfy the probability limits. The probability of nonperformance due to inter-story drift for CP performance level satisfies the probability limit, while those for LS and IO performance levels are about 50% higher than the probability limits. The probabilities of nonperformance due to either plastic hinge or inter-story drift for all three performance levels are about 50% higher than the probability limits. These

results indicate that the optimal structure shall be designed based on higher relative strength and/or relative stiffness factors to ensure that the probabilities of nonperformance satisfies the probability limits.

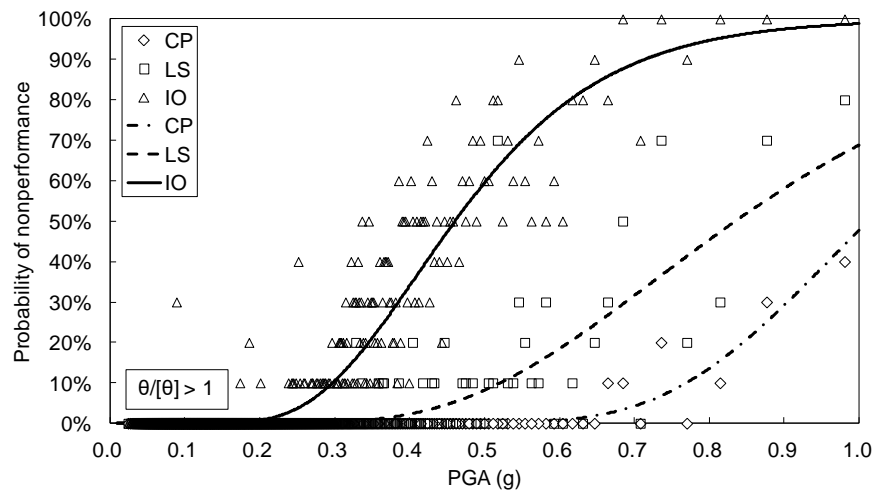
4.6.3 Fragility curve of nonperformance probability

The fragility curves of the optimal and original structures are generated by using the method described in Section 4.5, and drawn in Figures 4.12 and 4.13, respectively. The estimated median value and estimated standard deviation used to create the lognormal distributed fragility curves are achieved based on the normalized deformations of the 8000 samples for each structure. In Figures 4.12 or 4.13, the fragility curves of three types of nonperformance (due to either plastic hinge or inter-story drift, only due to plastic hinge, and only due to inter-story drift) are drawn. The fragility curves of each type of nonperformance include three curves for three performance levels (CP, LS, and IO).

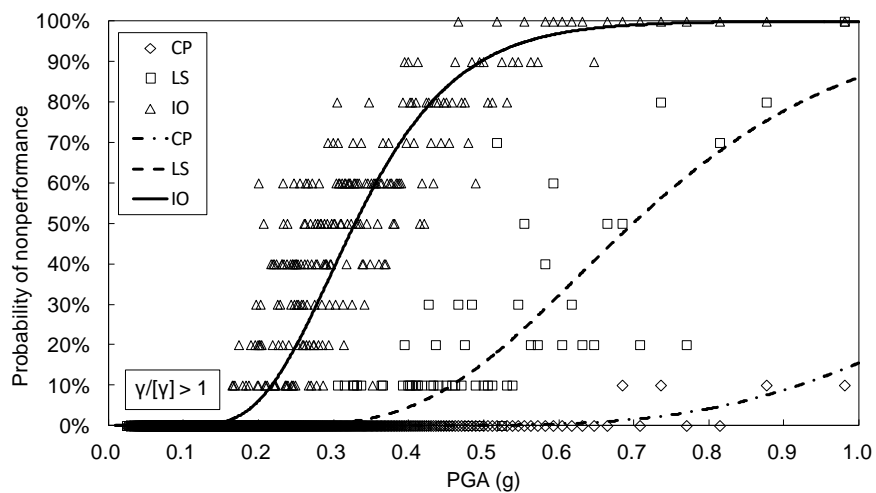
These fragility curves can be used to determine the failure probability of a structure under a selected PGA. In this study, the PGA corresponding to very rare, rare, and occasional earthquakes are 0.6g, 0.4g and 0.174g. In addition, the fragility curves of different performance levels can be used to define structure damage states: None, slight, moderate and extensive. As shown in Figure 4.14, these four types of structure damage states can be defined as: (1) none damage, when deformation is less than deformation limit of IO performance level; (2) slight damage, when deformation is more than deformation limit of IO performance level but less than that of LS performance level; (3) moderate damage, when deformation is more than deformation



(a)

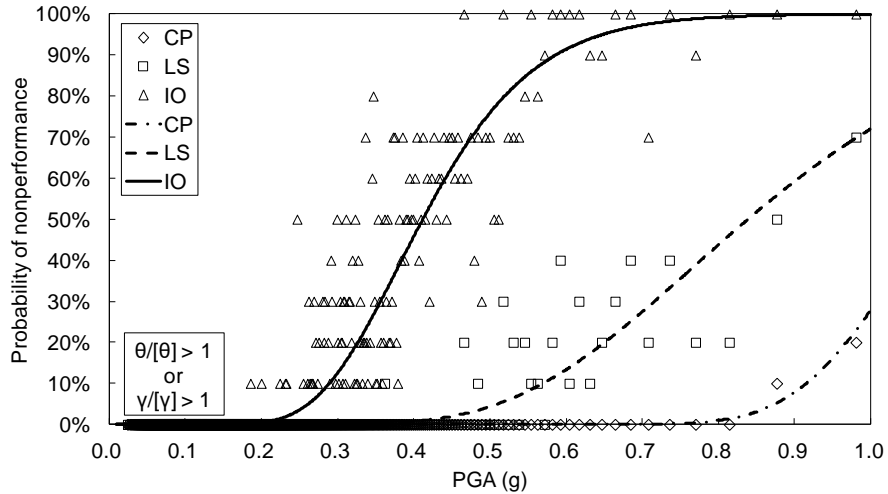


(b)

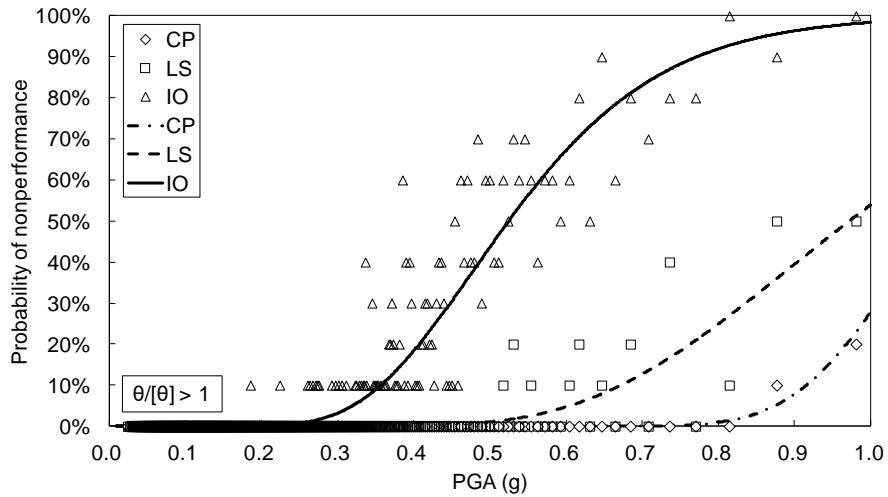


(c)

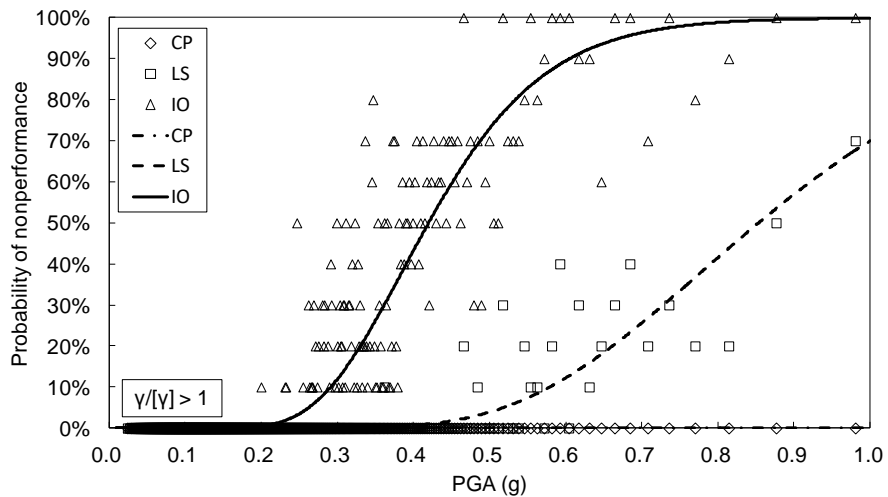
Figure 4.12 Fragility curves for the optimal design in different nonperformance types: (a) either $\theta/[\theta] > 1$ or $\gamma/[\gamma] > 1$; (b) $\theta/[\theta] > 1$; and (c) $\gamma/[\gamma] > 1$



(a)



(b)



(c)

Figure 4.13 Fragility curves for the original design in different nonperformance types: (a) either $\theta/[\theta] > 1$ or $\gamma/[\gamma] > 1$; (b) $\theta/[\theta] > 1$; and (c) $\gamma/[\gamma] > 1$

limit of LS performance level but less than that of CP performance level; extensive damage, when deformation is more than deformation limit of CP performance level. The probability of occurrence each damage state of a structure under a specific PGA is defined as p_i ($i = 1, 2, 3,$ or 4 for None, slight, moderate or extensive damage states). Probability of nonperformance of a structure for a specific PGA is defined as P_j ($j = \text{IO, LS, or CP performance level}$). Therefore, based on Figure 4.14, p_i can be calculated based on Equation 4.12.

$$\begin{aligned}
 p_i &= 1 - P_j & (i = 1, j = \text{IO}) \\
 &= P_j - P_{j+1} & (i = 2 \text{ or } 3, j = \text{IO or LS, } j+1 = \text{LS or CP}) \\
 &= P_j & (i = 4, j = \text{CP})
 \end{aligned}
 \tag{Equation 4.12}$$

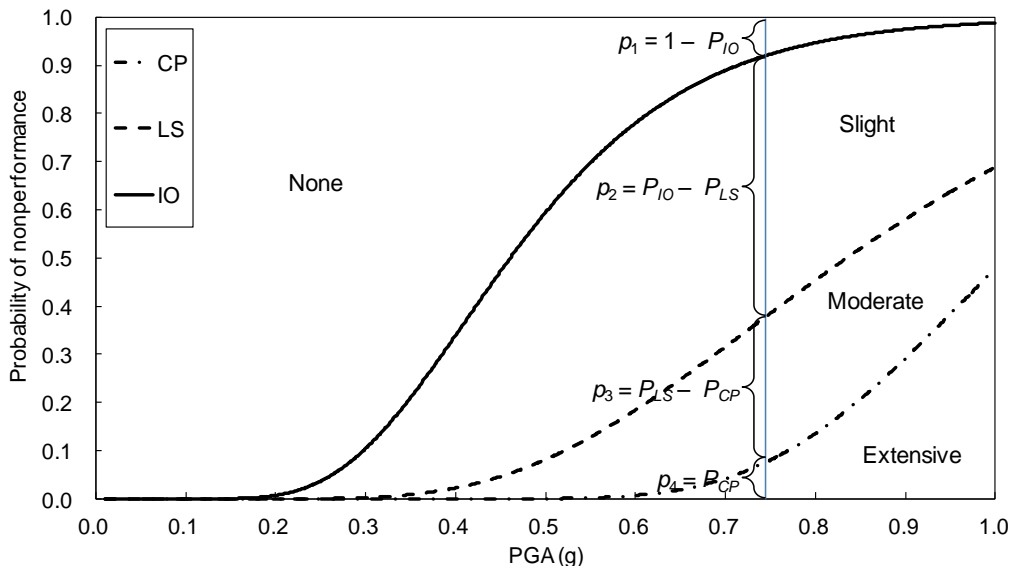


Figure 4.14 Definition of the four types of damage states

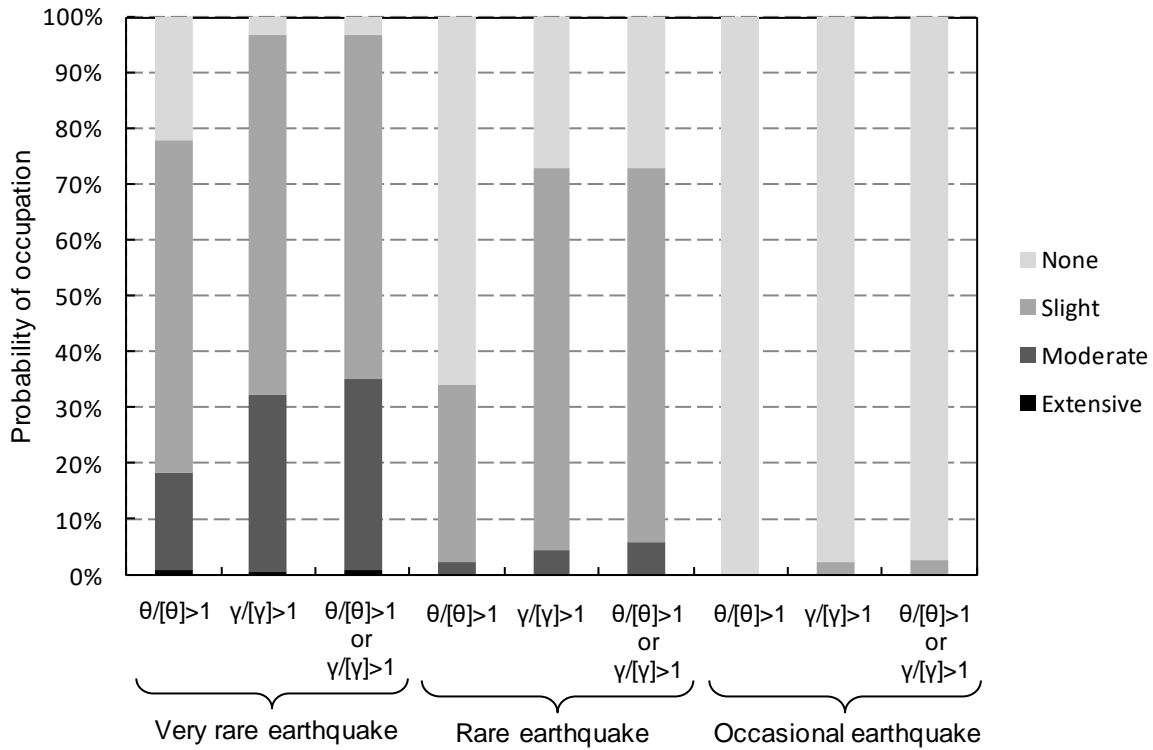
The p_i for both optimal and original structures under three hazard levels (very rare, rare, and occasional earthquake levels) are calculated and summarized in Table 4.5. Three PGA levels

are selected for both optimal and original structures according to the three hazard levels used in this study. For each selected PGA, Equation 4.12 is used to calculate the value of p_i based on P_j . Because P_j for three types of nonperformance (only due to plastic hinge, only due to inter-story drift, and due to either plastic hinge or inter-story drift) are given in Figures 4.12 and 4.13, p_i for this three types of nonperformed are summarized in Table 4.5.

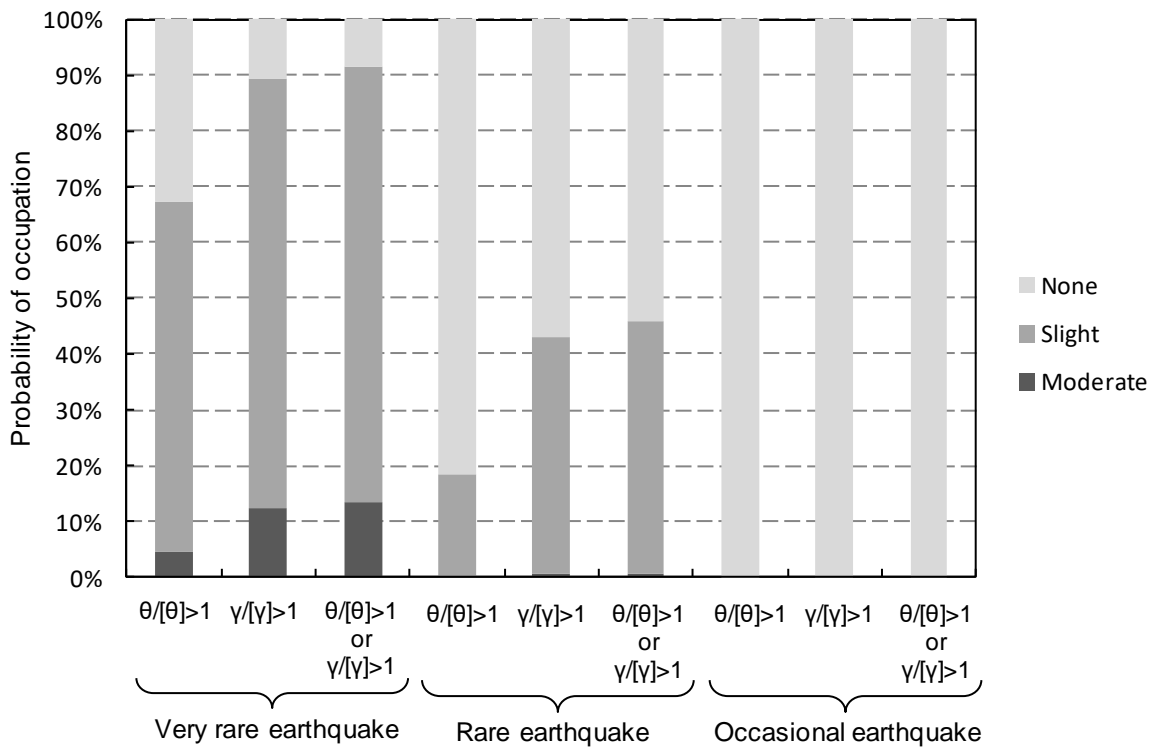
Table 4.5 Probability of occurrence of the optimal and original structures under three hazard levels (unit: %)

PGA (g)	Damage states	Optimal Structure			Original Structure		
		$\theta/[\theta] > 1$	$\gamma/[\gamma] > 1$	$\theta/[\theta] > 1$ or $\gamma/[\gamma] > 1$	$\theta/[\theta] > 1$	$\gamma/[\gamma] > 1$	$\theta/[\theta] > 1$ or $\gamma/[\gamma] > 1$
0.6 (Very rare)	Extensive	0.7	0.4	0.7	0	0	0
	Moderate	17.7	31.8	34.4	4.67	12.2	13.3
	Slight	59.6	64.8	61.6	62.53	77.3	78.1
	None	22.0	3.0	3.3	32.80	10.6	8.6
0.4 (Rare)	Extensive	0	0	0	0	0	0
	Moderate	2.3	4.5	5.7	0.10	0.6	0.7
	Slight	31.7	68.4	67.3	18.23	42.6	45.0
	None	66.1	27.1	27.0	81.67	56.8	54.3
0.174 (Occasional)	Extensive	0	0	0	0	0	0
	Moderate	0	0	0	0	0	0
	Slight	0.2	2.4	2.8	0	0.1	0.1
	None	99.8	97.6	97.2	100	99.9	99.9

To have a better understand of the data in Table 4.5, these data are drawn in Figure 4.15 for both optimal and original structures. Four type of structural damage states (extensive, moderate, slight, and none) are representative by four different colors form dark to light. For the original structure, no extensive damage state exists. In this figure, the tendency of the probability



(a)

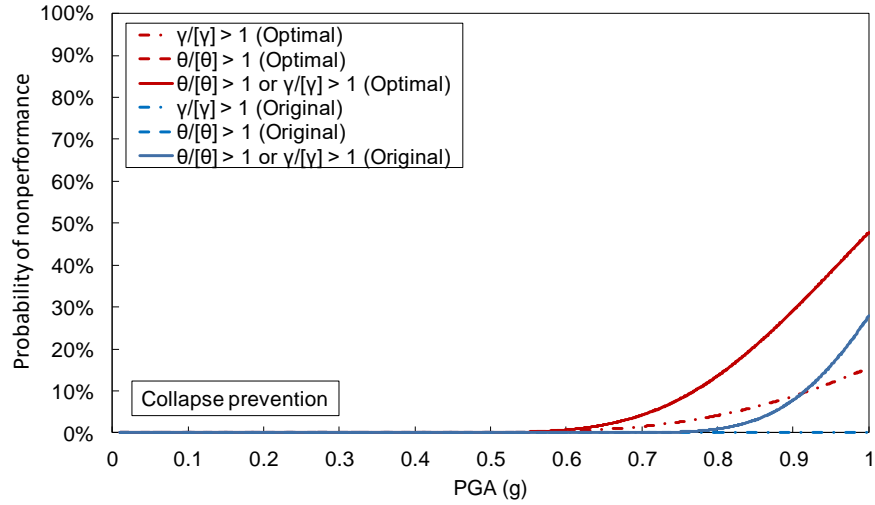


(b)

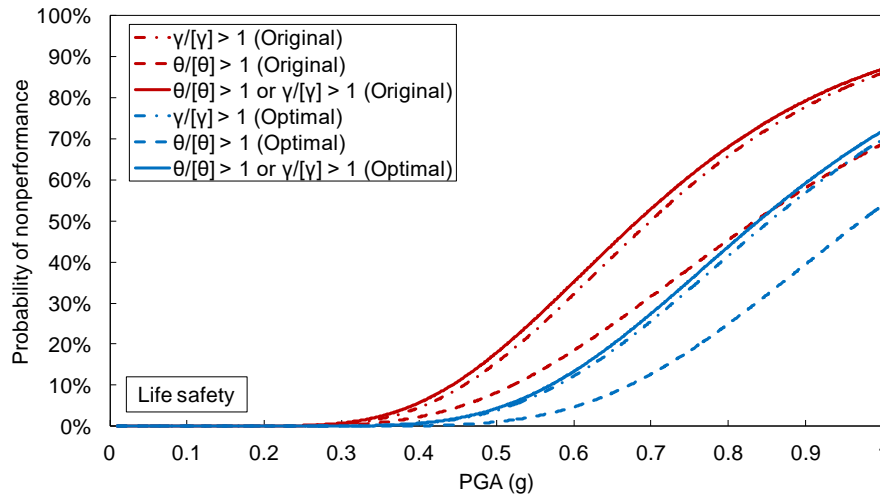
Figure 4.15 Probability histogram of four damage states of the (a) optimal and (b) original structures

of occupation of different damage state can be summarized as (1) under occasional earthquake hazard level, none damage state is predominate for both optimal and original structures; (2) under rare earthquake hazard level, none damage state is predominate for original structure, while slight damage state is predominate for optimal structure; (3) under very rare earthquake hazard level, slight damage state is predominate for both optimal and original structures; (4) under rare earthquake hazard level, the probability of occurrence of slight damage or moderate damage state when $\theta/[\theta] > 1$ is about half of that when $\gamma/[\gamma] > 1$ or when either $\theta/[\theta] > 1$ or $\gamma/[\gamma] > 1$ for both optimal and original structure; (5) under very rare earthquake level, the probability of occurrence of moderate damage state when $\theta/[\theta] > 1$ is about half of that when $\gamma/[\gamma] > 1$ or when either $\theta/[\theta] > 1$ or $\gamma/[\gamma] > 1$ for both optimal and original structure.

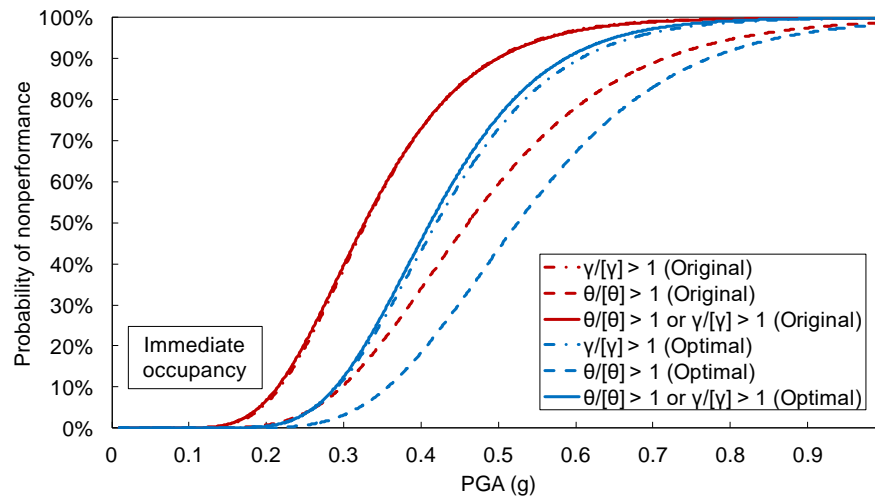
The fragility curves in Figures 4.12 and 4.13 are rearranged in Figure 4.16 based on the performance level. For comparison purpose, the fragility curves of both optimal and original structures for a selected performance level are drawn together. As shown in Figure 4.16(a), the minimum PGA when the probability of nonperformance for CP performance level is larger than zero for optimal and original structures are about 0.55g and 0.75g, respectively. The maximum difference of the probability of nonperformance between the fragility curves of optimal and original structures is about 20%. In Figure 4.16(b), when PGA is more than about 0.3g, the probability of nonperformance for LS performance level of the optimal structure is larger than zero; while when PGA is more than about 0.35g, the probability of nonperformance for LS performance level of the original structure is larger than zero. When PGA is more than 0.6g, the



(a)



(b)



(c)

Figure 4.16 Fragility curves for both the optimal and original designs in different performance levels: (a) collapse prevention; (b) life safety; and (c) immediate occupancy

difference between the fragility curves of the optimal and original structures remain constant as about 20%. Figure 4.16(c) shows that the fragility curves of IO performance level for both optimal and original structures. The minimum PGA when the probability of nonperformance for IO performance level is larger than zero for optimal and original structures are about 0.15g and 0.2g, respectively. The maximum PGA when the probability of nonperformance for IO performance level is close to 1.0 are 0.75g and 0.8g. When PGA is located between 0.3g and 0.5g, the difference between the fragility curves of the optimal and original structures remain constant as about 20%. In these figures, the probability of nonperformance of the fragility curve of the optimal structure is always higher than that of the optimal structure.

4.6.4 Nonperformance probability contour

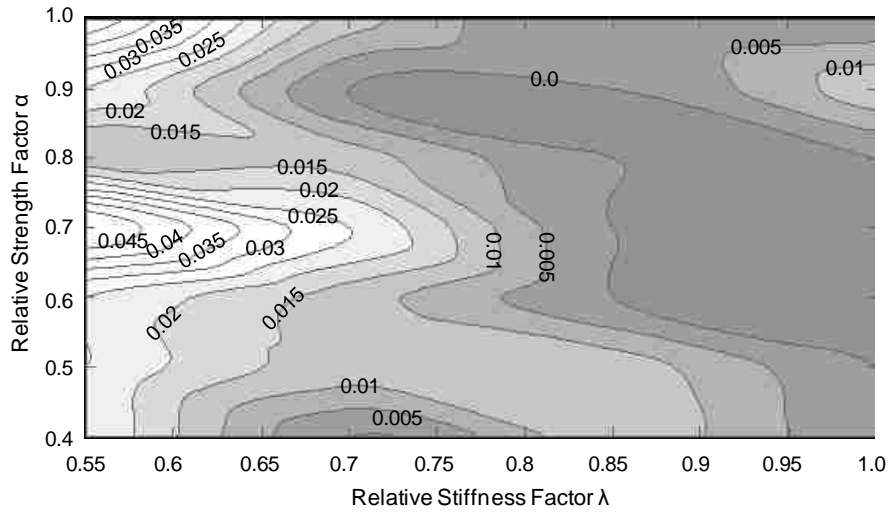
Reliability evaluations are performed on the 28 structures generated from the original structure using seven relative strength levels ($\alpha = 0.4, 0.5, 0.6, 0.7, 0.8, 0.9, \text{ and } 1.0$) and four relative stiffness levels ($\lambda = 0.55, 0.7, 0.85, 1.0$) to establish the nonperformance probability contours. Three types of nonperformance are considered: nonperformance due to inter-story drift, nonperformance due to plastic hinge rotation, and nonperformance due to either inter-story drift or plastic hinge rotation. Probability contours, as shown in Figures 4.17, 4.19 and 4.20, are created for each type of nonperformance at different performance levels (CP, LS and IO) to reflect the magnitude of the deformation.

Figure 4.17 shows the probability contours of nonperformance evaluated based only on inter-story drift. According to Figure 4.17(a), if a structure is designed with a relative strength

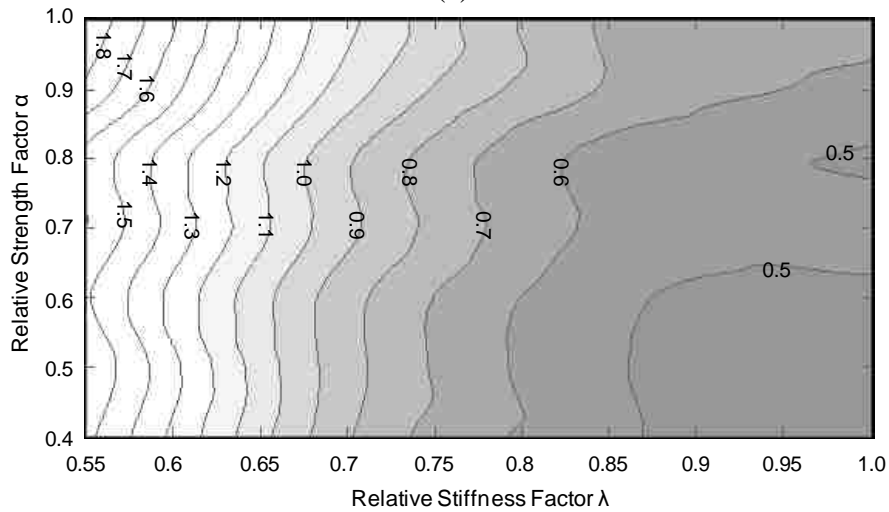
factor $\alpha > 0.4$ and a relative stiffness factor $\lambda > 0.55$, the nonperformance probability for CP is always lower than the probability limit(0.1%) of this performance level. Due to the very low probability of nonperformance, no obvious tendency can be identified from the nonperformance contours for CP.

As shown in Figure 4.17(b), when $\lambda > 0.8$, the nonperformance contours for LS can be approximated as lines oriented about 60 degrees relative to the horizontal axis. If the value of λ is fixed, the structure with lower α has lower nonperformance probability. This observation agrees with the performance of a SDOF system predicted using the $R-\mu-T$ relationship considered in this study (Section 1.2.2.3). Figure 4.18 shows the relationship between spectral displacement versus spectral acceleration for inelastic SDOF systems. As seen in this figure, if two structures have identical stiffness but different yield strength, the structure with a lower yield strength tends to have smaller lateral displacement demand. In addition, for each contour in Figure 4.17(b), two bumps exist when α is equal to about 0.8 and 0.6. This may be caused by the resonance between some earthquakes and the structures with α values equal to 0.8 and 0.6. When λ is larger than 0.8, the slope of the contour increases. When the nonperformance probability of the contours is lower than 0.5 for LS, the number of the nonperformance samples is too small to obtain an obvious tendency related to λ and α .

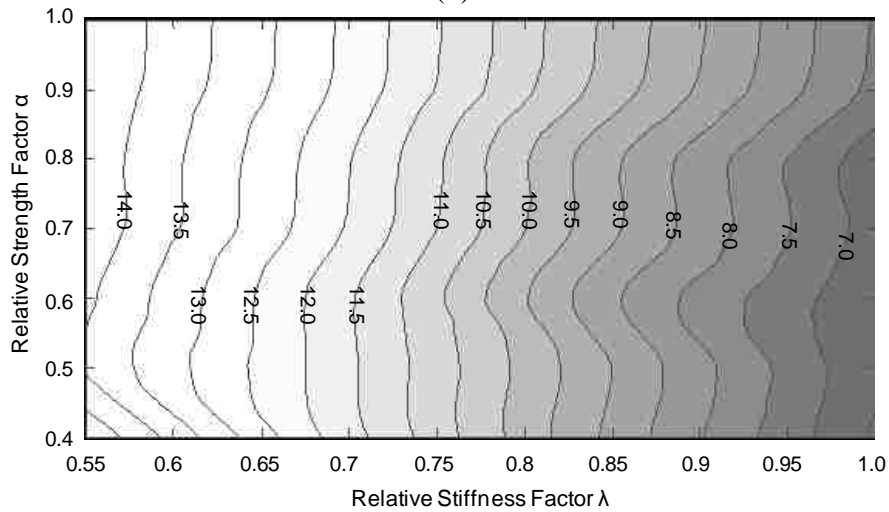
According to Figure 4.17(c), the nonperformance contours for IO performance level can be taken as lines with about a 70-degree slope with respect to the horizontal axis. Two bumps also exist in the contours when α values are about equal to 0.8 and 0.6. Because the probability of



(a)



(b)



(c)

Figure 4.17 Probability contours of nonperformance due to inter-story drift for different performance levels (a) collapse prevention' (b) life safety and (c) immediate occupancy (unit: %)

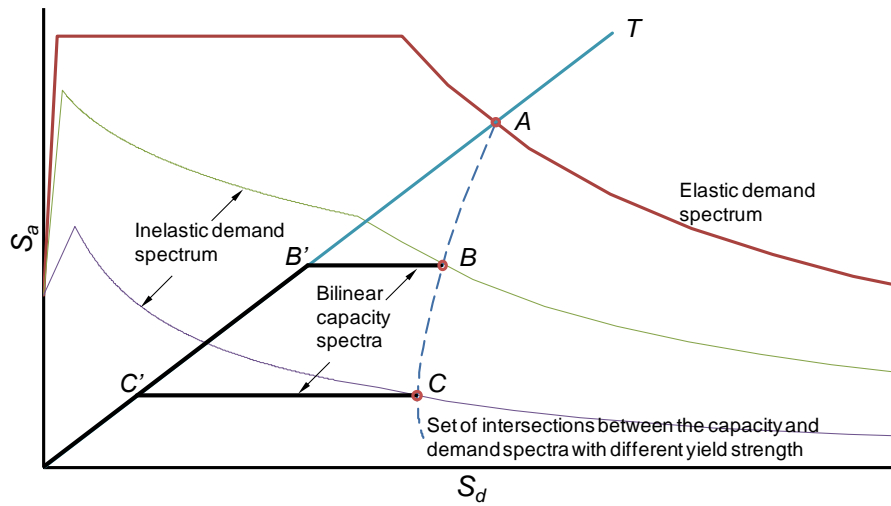
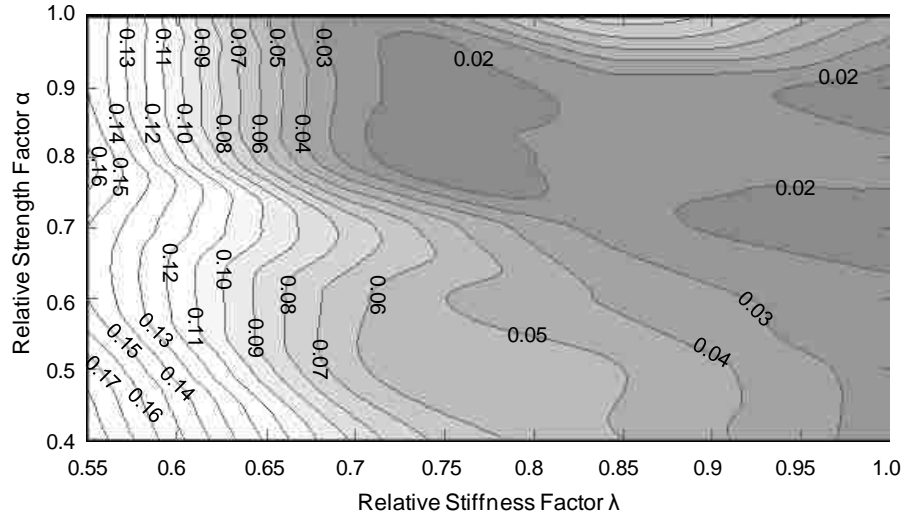


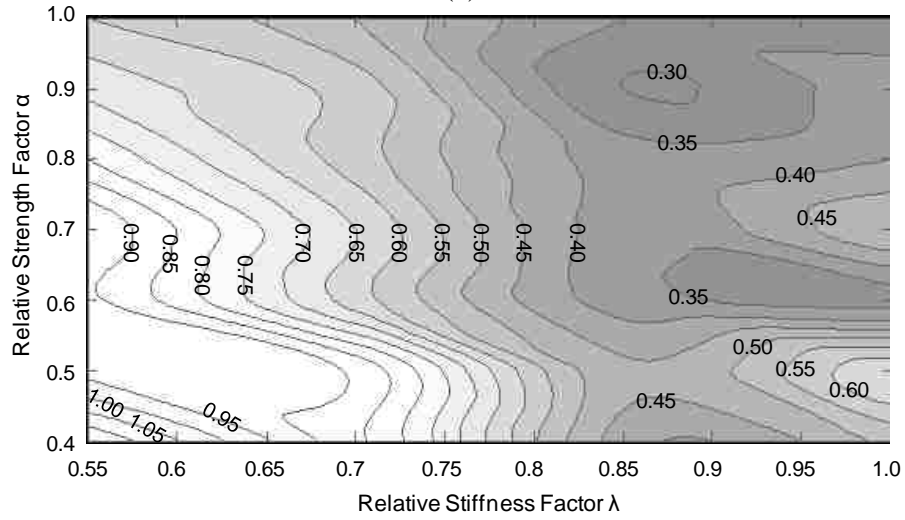
Figure 4.18 Deformation demand of inelastic SDOF systems with identical stiffness but different yield strength

nonperformance at IO performance level is higher than the other performance levels, the tendency of the contours is clearer. For both LS and IO performance levels shown in Figures 4.17(b) and 4.17(c), the nonperformance probability due to inter-story drift is affected mainly by the relative stiffness factor λ rather than the relative strength factor α . For the structures with an identical λ , the nonperformance probability due to inter-story drift is generally reduced with the decrease in α .

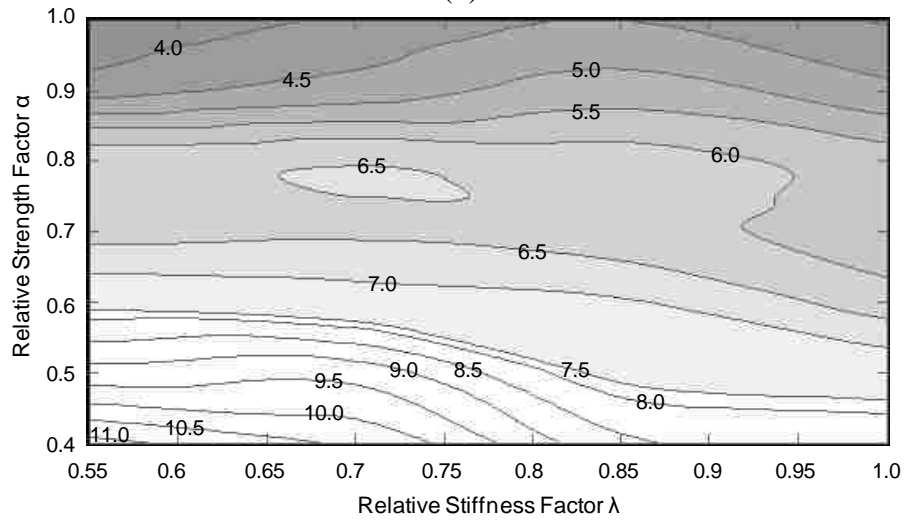
Figure 4.19 shows the contours of nonperformance caused by excessive plastic hinge rotation. In Figure 4.19(a) for CP, when $\lambda < 0.7$ and $0.9 < \alpha < 1.0$, or $\lambda < 0.7$ and $0.55 < \alpha < 0.65$, the nonperformance contours can be approximated as vertical lines. This reflects that, in these areas of λ and α , nonperformance probability is affected mainly by λ . When $\lambda < 0.7$ and $0.75 < \alpha < 0.9$, or $\lambda < 0.7$ and $0.4 < \alpha < 0.55$, the nonperformance contours can be taken as lines with a



(a)



(b)



(c)

Figure 4.19 Probability contours of nonperformance due to plastic hinge rotation for different performance levels (a) collapse prevention; (b) life safety and (c) immediate occupancy (unit: %)

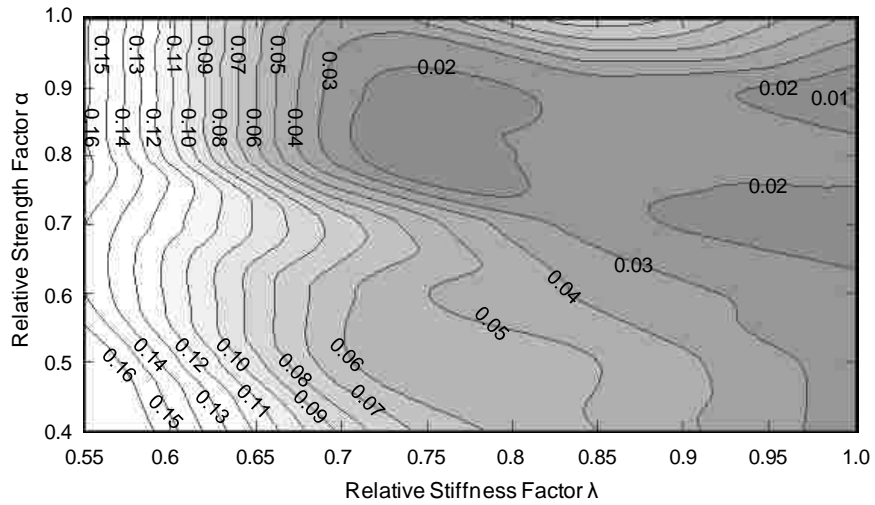
negative 45-degree slope with respect to the horizontal axis. Under this condition, if the value of λ is fixed, the nonperformance probability increase with the decrease of α . This indicates that to obtain an identical nonperformance probability, the structure can be designed based on higher α but lower λ , or based on lower α but higher λ . When $\lambda < 0.7$ and $0.65 < \alpha < 0.75$, the nonperformance contour can be approximated as lines with positive slope. This tendency shows that the structure designed with lower values of both λ and α would have an identical nonperformance probability to those with higher λ and α if $\lambda < 0.7$ and $0.65 < \alpha < 0.75$. When λ is more than 0.7 and α is less than 0.6, the nonperformance contours have about 45-degree angle with respect to the horizontal axis. Under this condition, if the value of λ is fixed, nonperformance probability increases with the decrease of α . For the other contours with very low nonperformance probability (0.02%), no obvious tendency can be identified. In Figure 4.19(a), especially for $\lambda < 0.7$, the feature of the contours of nonperformance due to plastic hinge rotation is similar to that due to inter-story drift shown in Figure 4.19(b). This could be because plastic hinge rotation is governed by inter-story drift under large lateral deformation.

As shown in Figure 4.19(c), the nonperformance contour for IO performance level is affected mainly by α instead of λ . When $0.9 < \alpha < 1.0$ and $0.55 < \lambda < 0.85$, the nonperformance contours can be approximated into lines with about 20-degree slope with respect to the horizontal axis. The slope increases with the value of λ . In two areas, one $0.9 < \alpha < 1.0$ and $0.85 < \lambda < 1.0$, the other with $0.4 < \alpha < 0.6$ and $0.7 < \lambda < 0.87$, the nonperformance contours can be approximated as lines oriented about 30 degrees relative to the horizontal axis. In these two areas,

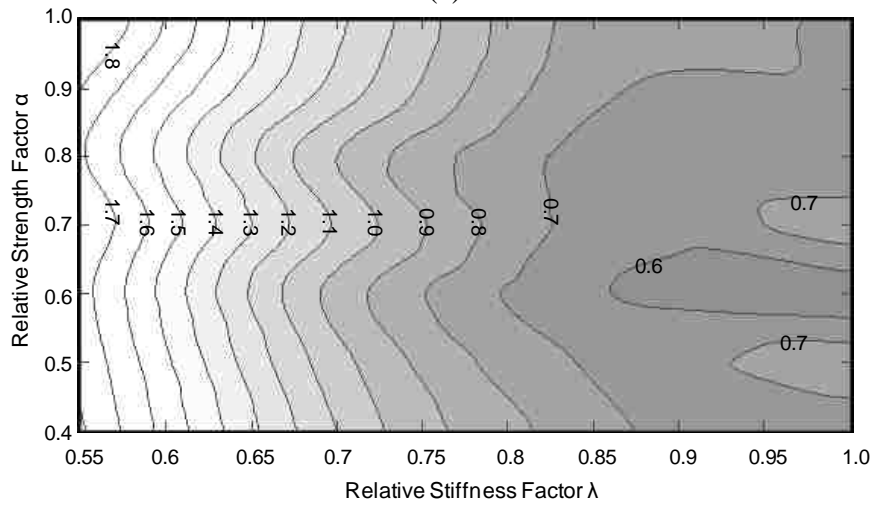
if the value of λ is fixed, the nonperformance probability increases with the reduction of α . The other contours in Figure 4.19(c) can be taken as horizontal lines, indicating that the probability nonperformance evaluated based only on plastic hinge is governed by α .

In Figure 4.19(b), if $\lambda < 0.8$ and $\alpha > 0.5$, the nonperformance contours for LS can be approximated into lines oriented about 40 degrees relative to the horizontal axis. Two bumps exist on these contours when the values of α are about equal to 0.6 and 0.8. If the value of λ is fixed, the nonperformance probability is reduced with the increase of α . If $\lambda < 0.55$ and $0.4 < \alpha < 0.5$, the tendency of the contours are similar to those for $\lambda < 0.8$ and $\alpha > 0.5$, but the slope is decreased from 40 degrees to 30 degrees. For the aforementioned two cases, both λ and α affect the nonperformance contours. This is because the number of plastic hinges and magnitude of plastic hinge rotation for LS is between those for CP and IO; accordingly, both inter-story drift and relative strength factor α affect the nonperformance contours. If $0.7 < \lambda < 0.83$ and $0.4 < \alpha < 0.5$, the contours are almost vertical. In this area, the nonperformance probability is affected mainly by λ rather than α . If $\lambda > 0.8$, a clear tendency cannot be identified due to the very low nonperformance probability.

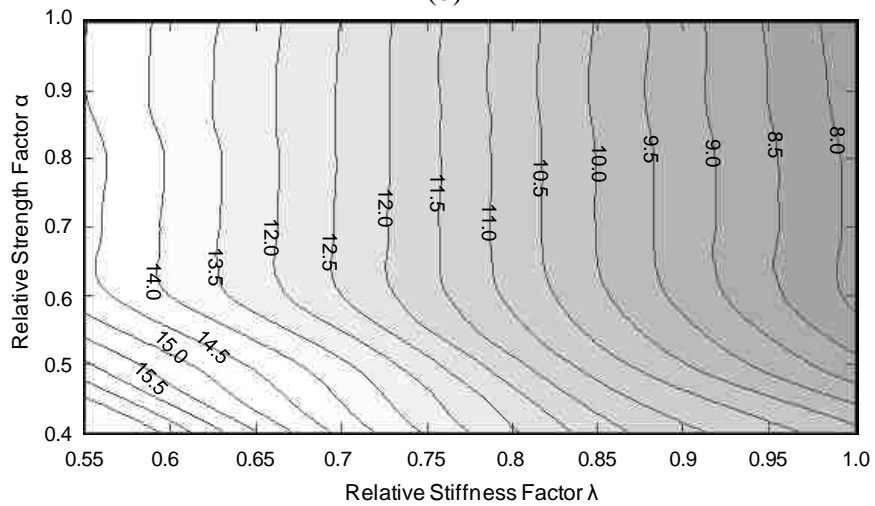
Figure 4.20 shows the probability contours of nonperformance due to either plastic hinge rotation or inter-story drift. The contours depends on the nonperformance probability due to plastic hinge rotation or inter-story drift, whichever controls. As shown in Figure 4.20(a), the nonperformance contours for CP are very similar to those shown in Figure 4.19(a) for CP. This is because the nonperformance probability due to inter-story drift is much lower than that due to



(a)



(b)



(c)

Figure 4.20 Probability contours of nonperformance due to either inter-story drift or plastic hinge rotation for different performance levels (a) collapse prevention; (b) life safety; and (c) immediate occupancy (unit: %)

plastic hinge rotation.

When α is more than 0.6, the nonperformance contours for LS shown in Figure 4.20(b) are similar to those due to inter-story drift alone (Figure 4.17(b)). This is because, when $\alpha > 0.6$, the nonperformance probability due to inter-story drift alone (Figure 4.17(b)) is at least 50% higher than that due to plastic hinge rotation only (Figure 4.19(b)). When $\alpha < 0.6$, the difference of nonperformance probability between the two types of contours becomes small, and the slope angle of the contours due to plastic hinge only is much smaller than that due to inter-story drift only. Therefore, when $\alpha < 0.6$, the contours due to either plastic hinge rotation or inter-story drift shown in Figure 4.20(b) are similar to those due to plastic hinge rotation only (Figure 4.19(b)).

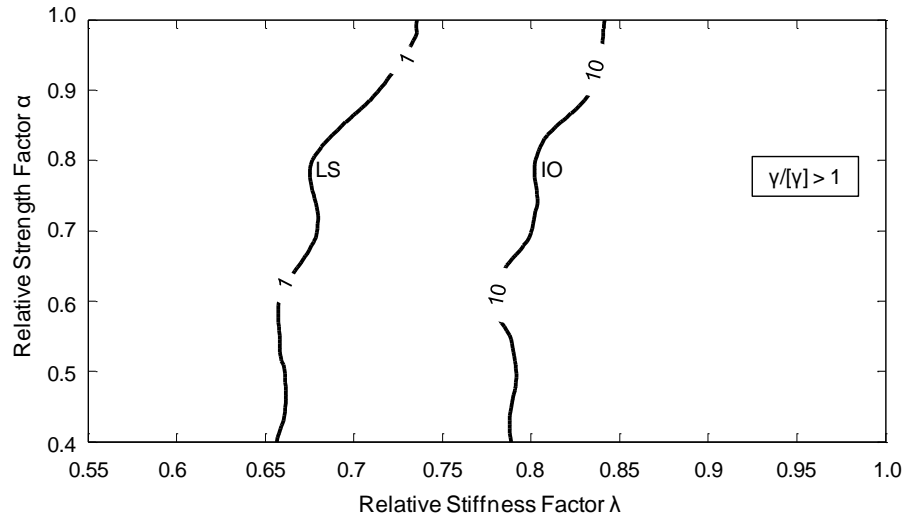
When the α is about equal to 0.6 and 0.8, two bumps exist in the contours shown in Figure 4.20(b). In this figure, the contours corresponding to nonperformance probability greater than 0.7 shown can be divided into four segments for $0.4 < \alpha < 0.6$, $0.6 < \alpha < 0.7$, $0.7 < \alpha < 0.8$, and $0.8 < \alpha < 1.0$. In the first and third segments, contours have 45- to 70-degree angles with respect to the horizontal axis. If the value of λ is fixed, the nonperformance probability is reduced with the increase of α . In the second and fourth segments, contours also have 45- to 70-degree angles with respect to the horizontal axis but are in the opposite direction. Thus, if the value of λ is fixed, the nonperformance probability increases with α . In all segments, the angle between the contours and the horizontal axis is reduced with the increase of λ .

The nonperformance contours due to either plastic hinge rotation or inter-story drift for IO are shown in Figure 4.20(c). When $\alpha > 0.6$, the contours are similar to those due to inter-story

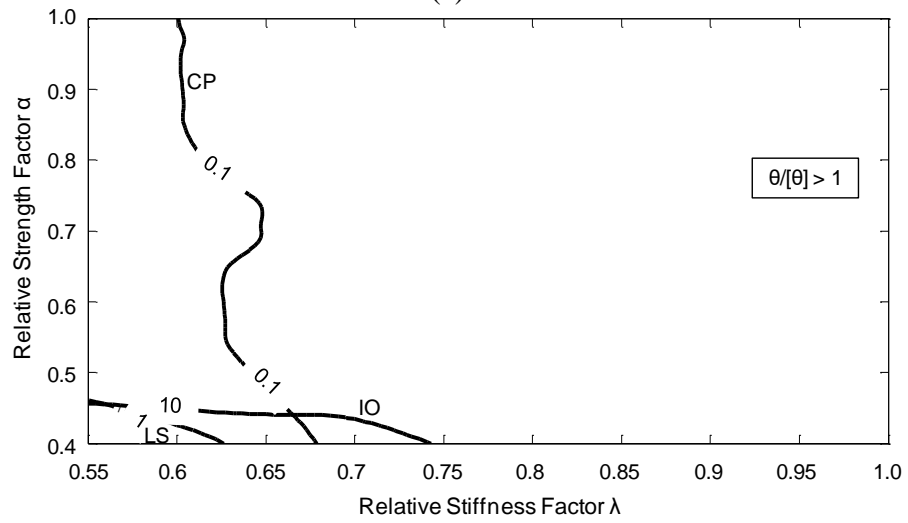
drift only because the nonperformance probability due to inter-story drift alone is much higher than that due to plastic hinge rotation alone. When $\alpha < 0.6$, the difference in nonperformance probability between the two types of contours shown in Figures 4.17(c) and 4.19(c) becomes less. The contours of nonperformance due to inter-story drift only and those due to plastic hinge rotation only for IO are affected respectively by λ and α . Thus, as shown in Figure 4.20(c), the contours of nonperformance based on both inter-story drift and plastic hinge rotation affected by both λ and α when $\alpha < 0.6$. In general, the contours in Figure 4.20(c) can be separately described by two segments based on the values of α : (1) $0.6 < \alpha < 1.0$ and (2) $0.4 < \alpha < 0.6$. In the first segment, the contours are almost vertical, implying that the nonperformance probability is primarily affected by λ rather than α . In the second segment, the contours can be approximated into lines with a 40-degree slope with respect to the horizontal axis. If the value of λ is fixed, the nonperformance probability increases with the reduction of α . This tendency reflects that, with the same nonperformance probability, a structure can be designed based on higher λ but lower α , or higher α but lower λ .

As shown in Table 4.4, the nonperformance probability limits suggested for CP, LS and IO performance levels are 0.1%, 1%, 10%, respectively. Figures 4.21 summarizes the nonperformance contours corresponding to these limits. If a structure is designed based on the values of λ and α at the point located on the right side of a contour, the nonperformance probability is lower than the nonperformance probability limits represented by this contour.

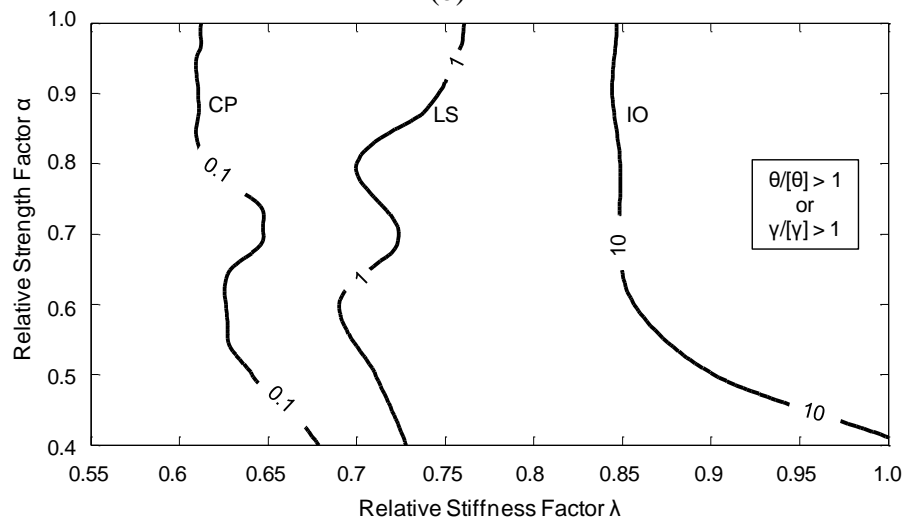
Figure 4.21(a) shows the nonperformance probability limits based on inter-story drift



(a)



(b)



(c)

Figure 4.21 Nonperformance contours due to (a) inter-story drift; (b) plastic hinge rotation; and (c) either plastic hinge rotation or inter-story drift (unit: %)

only. The nonperformance probability for structures within the range of λ and α is always lower than the limit for CP; thus, only the nonperformance contours corresponding to the limit of LS and IO are drawn. The nonperformance probability limit for IO performance level is on the right side. Therefore, it controls the feasible region of λ and α . If a structure is designed based on λ larger than 0.84 and α larger than 0.4, then the nonperformance probability due to inter-story drift satisfies all the nonperformance probability limits for three performance levels. Because the contour for IO has about 80-degree angle measured from the horizontal axis, if the structure is designed based on a low value of α such as 0.4, the feasible λ can be reduced to 0.78.

Figure 4.21(b) shows the nonperformance probability limits based on plastic hinge rotation only. If a structure is designed with $\lambda > 0.74$ and $\alpha > 0.4$, the nonperformance probability limit for IO performance level controls the feasible region of λ and α , and the nonperformance probability is lower than the limits for all three performance levels. If a structure is designed with $\alpha > 0.45$, the nonperformance probability limit for CP performance level controls the feasible region of λ and α . In this condition, the feasible λ can be reduced to 0.65 while the structure can still satisfy the nonperformance probability limit for all three performance levels.

As shown in Figure 4.21(c), the nonperformance probability limit for IO performance level controls the feasible region of λ and α . If a structure is designed with $\lambda > 0.85$ and $\alpha > 0.6$, then the nonperformance probability based on both plastic hinge rotation and inter-story drift is always lower than the limits for all three performance levels. The contour for IO performance level has a 40-degree angle with respect to the horizontal axis. Therefore, if a structure is

designed with $0.4 < \alpha < 0.6$ and this structure is expected to satisfy the nonperformance probability limits for all performance levels, the value of λ shall be increased from 0.85 to 1.0.

CHAPTER 5

SUMMARY AND CONCLUSIONS

5.1 Summary

The overall goal of this study is to develop an optimal performance-based seismic design (PBSD) method for multi-story RC moment frames. This method is expected to have low computational cost, and can be practically implemented by the U.S. design practice. To achieve this goal, four tasks are completed: (1) developing a simplified optimal PBSD procedure that incorporates the latest criteria of structural performance of RC frame buildings and can be practically implemented by design engineers; (2) applying the proposed optimal PBSD method to a prototype structure to investigate the efficiency of this method on cost saving; (3) examining whether the optimal design derived from Task 2 can satisfy the requirements of the selected performance levels under multiple hazard levels; and (4) performing structural reliability analyses on the optimal structure, original structure, and other structures with different flexural strength and stiffness to investigate how these factors affect the nonperformance probability of RC moment frames.

For the first task, an optimal PBSD method based on capacity spectrum method is developed for multi-story RC moment frames. This method minimizes the total construction cost, and ensure that the optimized frame satisfies the deformation constraints for multiple selected performance levels under different hazard levels. The proposed method simplifies the numerous

optimal variables into only two overall system variables normalized based on the original design: a relative stiffness factor and a relative strength factor. A two-step optimal procedure is adopted in this method. The feasible region boundary in the domain composed by the relative strength factor and the relative stiffness factor is determined. The feasible region boundary is transformed from the relative strength and stiffness factor domain to the material consumption domain. Then the optimal design in the domain composed by the consumption of concrete and reinforcement is determined.

To obtain the feasible region boundary in the first step, a convenient mathematical iteration method based on the results of a single pushover analysis is proposed to search the minimum relative stiffness for a given relative strength factor level. The feasible region boundary is composed by the minimum relative stiffness factors for different levels of relative strength factors. To obtain the optimal design in the second step, nonlinear programming method is used to search the optimal solution of the problem with a linear objective function and a convex feasible region.

For the second task, the proposed optimal PBSM method is applied to a six-story four-bay RC prototype structure. The structure is first designed based on the conventional force-based seismic design method as an initial design. The proposed optimal PBSM method is applied to obtain the feasible region boundary in the relative strength and stiffness factor domain, and the optimal design in the material consumption domain. The construction cost of the optimal design is derived and compared with that of the original design.

For the third task, the nonlinear responses of the optimal and original structures are determined from nonlinear dynamic analyses. The average structural responses under ten scaled earthquake records are evaluated. These ten records are scaled according to the design spectra of three selected hazard levels. The nonlinear responses of the optimal and original structures for these three hazard levels are examined by the preselected performance limits.

For the fourth task, structural reliability analyses are performed on the original and optimal structures by considering seven types of uncertainties in external loads, strength and stiffness used to define the structural model, and performance-based limits. Latin Hypercube sampling method is used to select the discrete values of the random variables, and combines these discrete model parameters to create 8000 structure model samples for both the optimal and the original structures. For each sample, nonlinear dynamic analysis is performed to obtain the normalized nonlinear structural deformations defined by inter-story drift and plastic hinge rotation. The normalized nonlinear structural deformation reflects whether the sample satisfies a target performance level. The normalized nonlinear structural deformations of 8000 samples are used to establish fragility curves and calculate the nonperformance probabilities of the optimal and original structures. Such a reliability analysis method is extended to on other 26 structures with various relative strength and stiffness factors different from the optimal and original structures. The nonperformance probabilities of the total 28 structures are used to establish the nonperformance contours to investigate how the relative strength and stiffness factors affect the nonperformance probability.

5.2 Conclusions

The following conclusion can be reached based on the optimal result of the prototype structure used in this study by applying the proposed optimal PBSM method:

(1) An optimal performance-based seismic design method for multi-story RC moment frames is proposed in this study based on the capacity spectrum method. The proposed method requires comparatively low computational cost.

(2) Compared with the conventional strength-based design, the proposed optimal PBSM method can lead to a 30% reduction in the needed flexural strength for the beams and the columns, a 26% reduction in this cross-sectional area, and about 20% reduction in the overall cost.

(3) If both inter-story drift and plastic hinge rotation are used to evaluate the structural nonlinear response, the optimal result for the prototype building is controlled by inter-story drift limit for the Life Safety performance level under rare earthquakes. If only plastic hinge rotation is used to measure structural performance, the construction cost can be further reduced, and the optimal design would be controlled by the limit for the Life Safety performance level under rare earthquakes. The limits of inter-story drift and plastic hinge rotation for Collapse Prevention performance level do not control the optimal result.

(4) Nonlinear dynamic analyses indicate that, in general, the optimal result derived from the proposed optimal PBSM method can satisfy the deformation limits of multiple performance levels under different hazard levels. The plastic hinge rotation demand are farther less than the

limits for all three performance levels.

(5) Structural reliability analyses indicate that, in general, the structural probability of nonperformance evaluated using inter-story drift is sensitive the relative stiffness factor rather than the relative strength factor. The probability of nonperformance due to plastic hinge rotation for Immediate Occupancy performance level is sensitive to relative strength factor instead of relative stiffness factor. The probability of nonperformance due to plastic hinge rotation for Life Safety performance level is affected by both relative strength factor and stiffness.

(6) When both plastic hinge rotation and inter-story drift are used to limit the response of structure, the probability for Collapse Prevention performance level is affected mainly by plastic hinge rotation. The probability of nonperformance for Life Safety and Immediate Occupancy performance levels is affected by both plastic hinge rotation and inter-story drift. The effect caused by inter-story drift is higher than plastic hinge rotation.

(7) To design a structure satisfying the probability limit of nonperformance due to inter-story drift, the relative stiffness factor λ shall be larger than 0.84 and the relative strength factor α shall be larger than 0.4. To design a structure satisfying the probability limit of nonperformance due to plastic hinge rotation, λ can be larger than 0.75 and the α can be larger than 0.4; otherwise, λ can be larger than 0.65 and the α can be larger than 0.45. To design a structure satisfying the probability limit of nonperformance due to either plastic hinge rotation or inter-story drift, λ shall be larger than 0.85 and the α shall be larger than 0.6.

5.3 Suggestions

The followings are future research suggestions:

(1) The proposed optimal PBSO method can be extended by using more optimal variables. This can be achieved by assigning different relative stiffness and strength factors for each story to optimize the stiffness and strength of the elements. A better optimal design can be obtained based in this way, which however requires additional optimal algorithm and computational cost.

(2) The proposed method can be applied to RC moment frames with different geometries considering the effect of higher vibration modes to further support the conclusions derived from the prototype structure in this study.

(3) To obtain an realistic flexural response of elements, fiber elements can be used to establish the structural model instead of using the plastic concentrated elements in this study. However, this will cause a large additional computational cost in structural analyses.

(4) The required minimum sampling number shall be determined in order to identify a clear tendency of contours, when the nonperformance probability is less than 0.1%.

REFERENCES

- Abrahamson, N. A., Silva, W. J., and Kamai, R. (2014). Summary of the ASK14 ground motion relation for active crustal regions. *Earthquake Spectra*, 30(3), 1025-1055.
- ACI (American Concrete Institute). (2014). *Building Code Requirements for Structural Concrete and Commentary. (ACI 318-14)*. American Concrete Institute, Farmington Hills, MI, 2014.
- Antoniou, S. and Pinho, R. (2004). Development and verification of a displacement-based adaptive pushover procedure. *Journal of Earthquake Engineering*, 8(5), 643-661.
- ASCE (American Society of Civil Engineers). (2010). *Minimum Design Loads for Buildings and Other Structures. (ASCE/SEI 7-10)*, American Society of Civil Engineers, Reston, VA, 2010.
- ASCE (American Society of Civil Engineers). (2007). *Seismic Rehabilitation of Existing Buildings. (ASCE/SEI 41-06)*, American Society of Civil Engineers, Reston, VA, 2007.
- ASCE (American Society of Civil Engineers). (2014). *Seismic Rehabilitation of Existing Buildings. (ASCE/SEI 41-13)*, American Society of Civil Engineers, Reston, VA, 2014.
- ATC (Applied Technology Council). (1996). *Seismic Evaluation and Retrofit of Concrete Buildings. (ATC-40)*, Applied Technology Council, California Seismic Safety Commission: Redwood City, CA, 1996.
- Ayyub, B. M. and McCuen, R. H. (2016). *Probability, statistics, and reliability for engineers and scientists*. CRC press, 2016.
- Baker, J. W. (2015). Efficient analytical fragility function fitting using dynamic structural analysis. *Earthquake Spectra*, 31(1), 579-599.
- Bertero, R. D. and Bertero, V. V. (2002). Performance-based seismic engineering: the need for a reliable conceptual comprehensive approach. *Earthquake Engineering and Structural Dynamics*, 31(3), 627-652.
- Boore, D. M., Stewart, J. P., Seyhan, E., and Atkinson, G. M. (2014). NGA-West2 equations for

- predicting PGA, PGV, and 5% damped PSA for shallow crustal earthquakes. *Earthquake Spectra*, 30(3), 1057-1085.
- Bracci, J. M., Kunnath, S. K., and Reinhorn, A. M. (1997). Seismic performance and retrofit evaluation of reinforced concrete structures. *Journal of Structural Engineering*, 123(1), 3-10.
- Bulleit, W. M. (2008). Uncertainty in structural engineering. *Practice Periodical on Structural Design and Construction*, 13(1), 24-30.
- Campbell, K. W. and Bozorgnia, Y. (2014). NGA-West2 ground motion model for the average horizontal components of PGA, PGV, and 5% damped linear acceleration response spectra. *Earthquake Spectra*, 30(3), 1087-1115.
- Chan, C. M. and Zou, X. K. (2004). Elastic and inelastic drift performance optimization for reinforced concrete buildings under earthquake loads. *Earthquake Engineering and Structural Dynamics*, 33(8), 929-950.
- Chiou, B. S. J. and Youngs, R. R. (2014). Update of the Chiou and Youngs NGA model for the average horizontal component of peak ground motion and response spectra. *Earthquake Spectra*, 30(3), 1117-1153.
- Chopra, A. K. (2017). Dynamics of structures. theory and applications to. *Earthquake Engineering*, 2017.
- Chopra, A. K. and Goel, R. K. (1999). Capacity-demand-diagram methods based on inelastic design spectrum. *Earthquake Spectra*, 15(4), 637-656.
- Cowper G. R. (1996) The shear coefficient in Timoshenko's beam theory. *Journal of Applied Mechanics*, 33(2), 335-340.
- Deierlein, G. G., Reinhorn, A. M., and Willford, M. R. (2010). Nonlinear structural analysis for seismic design. *NEHRP Seismic Design Technical Brief*, 4, 1-36.
- Ellingwood, B. (1980). Development of a probability based load criterion for American National Standard A58: Building code requirements for minimum design loads in buildings and other structures (Vol. 13). US Department of Commerce, National Bureau of Standards,

1980.

Ellingwood, B. R. (2003). Toward load and resistance factor design for fiber-reinforced polymer composite structures. *Journal of Structural Engineering*, 129(4), 449-458.

Elwood, K. J. and Eberhard, M. O. (2009). Effective stiffness of reinforced concrete columns. *ACI Structural Journal*, 106(4), 1-5.

Elwood, K. J., Matamoros, A. B., Wallace, J. W., Lehman, D. E., Heintz, J. A., Mitchell, A. D., and Moehle, J. P. (2007). Update to ASCE/SEI 41 concrete provisions. *Earthquake Spectra*, 23(3), 493-523.

Fajfar, P. (1999). Capacity spectrum method based on inelastic demand spectra. *Earthquake Engineering and Structural Dynamics*, 28(9), 979-993.

Fajfar, P. (2000). A nonlinear analysis method for performance-based seismic design. *Earthquake Spectra*, 16(3), 573-592.

Fajfar, P. and Gaspersic, P. (1996). The N2 method for the seismic damage analysis of RC buildings. *Earthquake Engineering and Structural Dynamics*, 25(1), 31-46.

Fajfar, P. (2002). Structural analysis in earthquake engineering—a breakthrough of simplified non-linear methods. *12th European Conference on Earthquake Engineering*, 2002.

Fajfar, P. and Fischinger, M. (1988). N2-A method for non-linear seismic analysis of regular buildings. *Proceedings of the Ninth World Conference in Earthquake Engineering*. 5, 111-116.

FEMA (Federal Emergency Management Agency). (1997). *NEHRP guidelines for the seismic rehabilitation of buildings*. (FEMA 273), Federal Emergency Management Agency, Washington, D.C, 1997.

FEMA (Federal Emergency Management Agency). (1997). *NEHRP commentary on the guidelines for the seismic rehabilitation of buildings*. (FEMA 274), Federal Emergency Management Agency, Washington, D.C, 1997

FEMA (Federal Emergency Management Agency). (2000). *Prestandard and commentary for the seismic rehabilitation of buildings*. (FEMA 356), Federal Emergency Management

Agency Washington, D.C, 2000.

Fragiadakis, M., and Papadrakakis, M. (2008). Performance-based optimum seismic design of reinforced concrete structures. *Earthquake Engineering & Structural Dynamics*, 37(6), 825-844.

Freeman, S. A. (1998). Development and use of capacity spectrum method. *The 6th US National Conference on Earthquake Engineering/EERI*, Seattle, Washington, 1998.

Ganzerli, S., Pantelides, C. P., and Reaveley, L. D. (2000). Performance-based design using structural optimization. *Earthquake Engineering and Structural Dynamics*, 29(11), 1677-1690.

Gaxiola-Camacho, J. R., Azizsoltani, H., Villegas-Mercado, F. J., and Haldar, A. (2017). A novel reliability technique for implementation of Performance-Based Seismic Design of structures. *Engineering Structures*, 142, 137-147.

Ghobarah, A. (2001). Performance-based design in earthquake engineering: state of development. *Engineering Structures*, 23(8), 878-884.

Gholizadeh, S. (2015). Performance-based optimum seismic design of steel structures by a modified firefly algorithm and a new neural network. *Advances in Engineering Software*, 81, 50-65.

Gholizadeh, S. and Moghadas, R. K. (2014). Performance-based optimum design of steel frames by an improved quantum particle swarm optimization. *Advances in Structural Engineering*, 17(2), 143-156.

Goel, S. C. and Chao, S. H. (2008). Performance-based plastic design: earthquake-resistant steel structures. *International Code Council*, 2008.

Goel, S. C., Liao, W. C., and Reza Bayat, M. (2010). Performance-based plastic design (PBPD) method for earthquake-resistant structures: an overview. *The Structural Design of Tall and Special Buildings*, 19(1-2), 115-137.

Gong, Y. (2003). Performance-based design of building frameworks under seismic loading. PhD thesis, University of Waterloo, Waterloo, Canada, 2003.

- Gong, Y., Xu, L., and Grierson, D. E. (2005). Performance-based sensitivity analysis of steel moment frameworks under seismic loading. *International Journal of Numerical Methods in Engineering*, 63(9), 1229-1249.
- Grierson, D. E., Gong, Y., and Xu, L. (2006). Optimal performance-based seismic design using modal pushover analysis. *Journal of Earthquake Engineering*, 10(1), 73-96.
- Gupta, B. and Kunnath, S. K. (2000). Adaptive spectra-based pushover procedure for seismic evaluation of structures. *Earthquake Spectra*, 16(2), 367-392.
- Hajirasouliha, I., Asadi, P., and Pilakoutas, K. (2012). An efficient Performance-based seismic design method for reinforced concrete frames, *Earthquake Engineering and Structural Dynamics*, 41(4), 663-679.
- Hettmansperger, T. P. and McKean, J. W. (1978). Statistical inference based on ranks. *Psychometrika*, 43(1), 69-79.
- Huang, M. F., Li, Q., Chan, C. M., Lou, W. J., Kwok, K. C., and Li, G. (2015). Performance-based design optimization of tall concrete framed structures subject to wind excitations. *Journal of Wind Engineering and Industrial Aerodynamics*, 139, 70-81.
- Huyse, L., Chen, R., and Stamatakos, J. A. (2010). Application of generalized Pareto distribution to constrain uncertainty in peak ground accelerations. *Bulletin of the Seismological Society of America*, 100(1), 87-101.
- Ibarra, L. F., Medina, R. A., and Krawinkler, H. (2005). Hysteretic models that incorporate strength and stiffness deterioration. *Earthquake Engineering and Structural Dynamics*, 34(12), 1489-1511.
- Ibarra, L. F. and Krawinkler, H. (2005). Global collapse of frame structures under seismic excitations. Berkeley, CA: Pacific Earthquake Engineering Research Center, 2005.
- Idriss, I. M. (2014). An NGA-West 2 empirical model for estimating the horizontal spectral values generated by shallow crustal earthquakes. *Earthquake Spectra*, 30(3), 1155-1177.
- Iervolino, I. and Cornell, C. A. (2008). Probability of occurrence of velocity pulses in near-source ground motions. *Bulletin of the Seismological Society of America*, 98(5),

2262-2277.

- Iman, R. L. and Conover, W. J. (1980). Small sample sensitivity analysis techniques for computer models, with an application to risk assessment. *Communications in Statistics-theory and Methods*, 9(17), 1749-1842.
- Kalkan, E., and Kunnath, S. K. (2007). Assessment of current nonlinear static procedures for seismic evaluation of buildings. *Engineering Structures*, 29(3), 305-316.
- Kaveh, A., Azar, B. F., and Hadidi, A. (2010). Performance-based seismic design of steel frames using ant colony optimization. *Journal of Constructional Steel Research*, 66(4), 566-574.
- Kaveh, A., Laknejadi, K., and Alinejad, B. (2012). Performance-based multi-objective optimization of large steel structures. *Acta Mechanica*, 223(2), 355-369.
- Kaveh, A. and Nasrollahi, A. (2014). Performance-based seismic design of steel frames utilizing charged system search optimization. *Applied Soft Computing*, 22, 213-221.
- Khatibinia, M., Fadaee, M. J., Salajegheh, J., and Salajegheh, E. (2013). Seismic reliability assessment of RC structures including soil–structure interaction using wavelet weighted least squares support vector machine. *Reliability Engineering and System Safety*, 110, 22-33.
- Kogut, G. F. and Chou, K. C. (2004). Partial resistance factor design on steel–concrete beam-columns. *Engineering Structures*, 26(7), 857-866.
- Krawinkler, H. (1992). Seismic design based on ductility and cumulative damage demand and capacities. *Nonlinear Seismic Analysis and Design of Reinforced Concrete Buildings*, 23-39.
- Krawinkler, H. (1999). Challenges and progress in performance-based earthquake engineering. *International Seminar on Seismic Engineering for Tomorrow–In Honor of Professor Hiroshi Akiyama*, 26.
- Krawinkler, H., and Seneviratna, G. D. P. K. (1998). Pros and cons of a pushover analysis of seismic performance evaluation. *Engineering structures*, 20(4-6), 452-464.
- Kircher, C. A., Reitherman, R. K., Whitman, R. V., and Arnold, C. (1997). Estimation of

- earthquake losses to buildings. *Earthquake Spectra*, 13(4), 703-720.
- Kreslin, M. and Fajfar, P. (2012). The extended N2 method considering higher mode effects in both plan and elevation. *Bulletin of Earthquake Engineering*, 10(2), 695-715.
- Lee, J. O., Yang, Y. S., and Ruy, W. S. (2002). A comparative study on reliability-index and target-performance-based probabilistic structural design optimization. *Computers and Structures*, 80(3-4), 257-269.
- Li, G., Lu, H., and Liu, X. (2010). A hybrid genetic algorithm and optimality criteria method for optimum design of RC tall buildings under multi-load cases. *The Structural Design of Tall and Special Buildings*, 19(6), 656-678.
- Li, G. and Hu, H. (2014). Risk design optimization using many-objective evolutionary algorithm with application to performance-based wind engineering of tall buildings. *Structural Safety*, 48, 1-14.
- Liang, Q. Q., Uy, B., and Steven, G. P. (2002). Performance-based optimization for strut-tie modeling of structural concrete. *Journal of Structural Engineering*, 128(6), 815-823.
- Lignos, D. G. and Krawinkler, H. (2012). Development and utilization of structural component databases for performance-based earthquake engineering. *Journal of Structural Engineering*, 139(8), 1382-1394.
- Lignos, D. G. and Krawinkler, H. (2010). Deterioration modeling of steel components in support of collapse prediction of steel moment frames under earthquake loading. *Journal of Structural Engineering*, 137(11), 1291-1302.
- Lignos, D. (2008). Sidesway collapse of deteriorating structural systems under seismic excitations. Stanford university, 2008.
- Liu, M., Burns, S. A., and Wen, Y. K. (2005). Multiobjective optimization for performance-based seismic design of steel moment frame structures. *Earthquake Engineering and Structural Dynamics*, 34(3), 289-306.
- Liu, B. Q., Liu, M., and Li, Y. B. (2004). Research and development of performance-based seismic design theory. *The 13th World Conference on Earthquake Engineering*,

Vancouver (BC), Canada, 2004.

McCormac, J. C. and Brown, R. H. (2015). Design of reinforced concrete. John Wiley and Sons, 2015.

Mechakhchekh, A. and Ghosn, M. (2007). Reliability-based procedure for developing load and resistance factor seismic bridge design specifications. *Transportation Research Record*, 2028(1), 173-179.

Moehle, J. (1992). Displacement-based design of RC structures subjected to earthquakes. *Earthquake Spectra*, 8(3), 403-428.

Moehle, J. P. (1996) Displacement-based seismic design criteria. *11th World Conference on Earthquake Engineering*, Acapulco, Mexico, 1996

Moharrami, H. and Grierson, D. E. (1993). Computer-automated design of reinforced concrete frameworks. *Journal of Structural Engineering*, 119(7), 2036-2058.

Miranda, E. and Bertero, V. V. (1994). Evaluation of strength reduction factors for earthquake-resistant design. *Earthquake Spectra*, 10(2), 357-379.

Möller, O., Foschi, R. O., Ascheri, J. P., Rubinstein, M., & Grossman, S. (2015). Optimization for performance-based design under seismic demands, including social costs. *Earthquake Engineering and Engineering Vibration*, 14(2), 315-328.

Möller, O., Foschi, R. O., and Quiroz, L. M. (2009). Structural optimization for performance-based design in earthquake engineering: applications of neural networks. *Structural Safety*, 31(6), 490-499.

Murakami, M. and Penzien, J. (1975). Nonlinear response spectra for probabilistic seismic design and damage assessment of reinforced concrete structures. *Earthquake Engineering Research Center*, University of California, 1975.

Nassar, A. A., Oстераas, J. D., and Krawinkler, H. (1992). Seismic design based on strength and ductility demands. *10th World Conference on Earthquake Engineering*, 10, 5861-5866.

Newmark, N. M. and Hall, W. J. (1982). Earthquake spectra and design. *Earthquake Engineering Research Institute*, Berkeley, CA, 1982

- Newmark, N. M., Hall, W. J. (1969). Seismic design criteria for nuclear reactor facilities. *World Conference of Earthquake Engineering*, B-4. 37-50.
- Park, Y. and Ang, A. (1985). Mechanistic seismic damage model for reinforced concrete. *Journal of Structural Engineering*, 111(4), 722–739.
- Park, H. G., Eom, T., and Lee, H. (2007). Factored modal combination for evaluation of earthquake load profiles. *Journal of Structural Engineering*, 133(7), 956-968.
- Paulay, T. and Priestley, M. J. N. (1992). Seismic design of reinforced concrete and masonry buildings, *Wiley-Interscience*, New York, 1992.
- Priestley, M. J. N., Calvi, G. M., and Kowalsky, M. J. (2007). Direct displacement-based seismic design. *2005 New Zealand Society for Earthquake Engineering Conference*, 33-43.
- Priestley, M. J. N. (2000). Performance based seismic design. *Bulletin of the New Zealand Society for Earthquake Engineering*, 33(3), 325-346.
- Priestley, M. J. N., Kowalsky, M. J., Ranzo, G., and Benzoni, G. (1996). Preliminary development of direct displacement-based design for multi-degree of freedom systems, *65th Annual SEAOC Convention*, 47-66.
- Priestley, M. J. N. and Park, R. (1987). Strength and ductility of concrete bridge columns under seismic loading. *Structural Journal*, 84(1), 61-76.
- Powell, G. H. (2008). Displacement-based seismic design of structures. *Earthquake spectra*, 24(2), 555-557.
- Plevris, V. ed. (2012). Structural seismic design optimization and earthquake engineering: formulations and applications: formulations and applications. *IGI Global*, 2012.
- Rainer, J. H. and Karacabeyli, E. (2000). Performance of wood-frame construction in earthquakes. *The 12th World Conference on Earthquake Engineering*, Auckland, New Zealand (30), 1-8.
- Rashedi, E., Nezamabadi-Pour, H., and Saryazdi, S. (2009). GSA: a gravitational search algorithm. *Information sciences*, 179(13), 2232-2248.

- Reinhorn, A. M. (1997). Inelastic analysis techniques in seismic evaluations. Seismic design methodologies for the next generation of performance based seismic engineering of codes, 277-287.
- Rwamamara, R., Simonsson, P., and Ojanen, J. (2010). Advantages of industrialized methods used in small bridge construction. *Annual Conference of the International Group for Lean Construction*, 569-579.
- Sasani, M. (1998). A two-level-performance-based design of reinforced concrete structural walls. *6th US National Conference on Earthquake Engineering*, EERI: Oakland, CA, 1998.
- Schmit, L. A. and Farshi, B. (1974). Some approximation concepts for structural synthesis. *American Institute of Aeronautics and Astronautics Journal*, 12(5), 692-699.
- SEAOC (Structural Engineers Association of California). (1995). *Performance Based Seismic Engineering of Buildings*. Sacramento, CA.
- SEAOC (Structural Engineers Association of California) Seismology Committee. (2008). A brief guide to seismic design factors. *Structure Magazine*, 30-32
- Shooman, M. L. (1968). Reliability physics models. *IEEE Transactions on Reliability*, 17(1), 14-20.
- Soegiarso, R. and Adeli, H. (1997). Optimum load and resistance factor design of steel space-frame structures. *Journal of Structural Engineering*, 123(2), 184-192.
- Soong, T. T. and Grigoriu, M. (1993). Random vibration of mechanical and structural systems. *NASA STI/Recon Technical Report*, A 93.
- Subramanian, N. (2010). Limiting reinforcement ratios for RC flexural members. *Indian Concrete Journal*, 84(9), 71.
- Sung, Y. C., Liao, W. I., and Yen, W. P. (2009). Performance-based concept on seismic evaluation of existing bridges. *Earthquake Engineering and Engineering Vibration*, 8(1), 127-135.
- Talatahari, S. (2013). Optimum performance-based seismic design of frames using metaheuristic optimization algorithms. *Metaheuristic applications in structures and infrastructures*. Elsevier, 419-37.

- Talatahari, S., Hosseini, A., and Mirghaderi, S. R. (2014). Optimum performance-based seismic design using a hybrid optimization algorithm. *Mathematical Problems in Engineering*, 2014.
- Veletsos, A. S. and Newmark, N. M. (1960) Effect of inelastic behavior on the response of simple systems to earthquake motions, *The 2nd World Conference on Earthquake Engineering*, 2, 895–912.
- Veletsos, A. S. and Newmark, N. M. (1964) Design procedures for shock isolation systems of underground protective structures, 3, *Response Spectra of Single-Degree-of-Freedom Elastic and Inelastic Systems*, Newmark Hansen and Associates Urbana.
- Vidic, T., Fajfar, P., and Fischinger, M. (1994). Consistent inelastic design spectra: strength and displacement. *Earthquake Engineering and Structural Dynamics*, 23(5), 507-521.
- Welch, D. P., Sullivan, T. J., and Calvi, G. M. (2014). Developing direct displacement-based procedures for simplified loss assessment in performance-based earthquake engineering. *Journal of Earthquake Engineering*, 18(2), 290-322.
- Xu, L., Gong, Y., and Grierson, D. E. (2006). Seismic design optimization of steel building frameworks. *Journal of Structural Engineering*, 132(2), 277-286.
- Yang, I. H. (2006). Uncertainty Analysis of Concrete Structures Using Modified Latin Hypercube Sampling Method. *International Journal of Concrete Structures and Materials*, 18(2E), 89-95.
- Yazdani, H., Khatibinia, M., Gharehbaghi, S., and Hatami, K. (2016). Probabilistic performance-based optimum seismic design of RC structures considering soil–structure interaction effects. *ASCE-ASME Journal of Risk and Uncertainty in Engineering Systems, Part A: Civil Engineering*, 3(2), G4016004.
- Zameeruddin, M. and Sangle, K. K. (2016). Review on Recent developments in the performance-based seismic design of reinforced concrete structures. *Structures*, 6, 119-133.
- Zou, X. K. and Chan, C. M. (2005 a). An optimal resizing technique for seismic drift design of concrete buildings subjected to response spectrum and time history loadings. *Computers*

and Structures, 83(19-20), 1689-1704.

Zou, X. K. and Chan, C. M. (2005 b). Optimal seismic performance-based design of reinforced concrete buildings using nonlinear pushover analysis. *Engineering Structures*. 27(8), 1289-1302.

Zou, X. K., Chan, C. M., and Li, G. (2007). Multi-objective optimization for performance-based design of reinforced concrete frames. *Journal of structural engineering*, 133(10), 1462-1474.

CURRICULUM VITAE

Graduate College
University of Nevada, Las Vegas

Chunyu Zhang

syzhangchunyu@sina.com

Education:

Bachelor of Science in Civil Engineering, Shenyang Jianzhu University, 2009
Master of Science in Civil Engineering, Shenyang Jianzhu University, 2012

Employment:

Coordinator of the evaluation and demonstration division Ministry of Construction of China	March 2012 - April 2013 Beijing, China
Online instructor Northeastern University, China	March 2012 - March 2010 Shenyang, China

Thesis Title:

Study of the seismic performance of high-strength concrete filled square steel tube column with inner CFRP circular tube frame structures (2012)

Dissertation Title:

Performance-based Economical seismic design of multistory reinforced concrete frame buildings and reliability assessment

Dissertation Examination Committee:

Chairperson, Dr. Ying Tian
Committee Member, Dr. Nader Ghafoori
Committee Member, Dr. Mohamed Kaseko
Committee Member, Dr. Samaan Ladkany
Graduate Faculty Representative, Dr. Mohamed Trabia

Publication:

Zhang, C., and Tian, Y. "Performance-based Optimal Seismic Design of Reinforced Concrete Frame Buildings," Engineering Structures, under review.

Wang, L., Tian, Y., Luo, W., Li, G., Zhang, S. and Zhang, C. “Experimental Study of Seismic Performance of Axially Restrained Reinforced Concrete Frame Beams,” Journal of Structural Engineering, accepted.

Li, G., Liu, D., Yang, Z., and Zhang, C. (2017). “Flexural Behavior of High Strength Concrete-filled High Strength Square Steel Tube,” Journal of Constructional Steel Research, 128, 732-744.

Li, G., Qiu, Z., and Zhang, C. (2016). “Dynamic Time-history Analysis of High-strength Concrete-filled Square Steel Tube Column with Inner CFRP Circular Tube Frame Structure,” Journal of Shenyang Jianzhu University (Natural Science), in Chinese, 32(2), 216-224.